

# Aerodynamic Performance Measurements in a Counter-Rotating Aspirated Compressor

by

**Jean-François Onnée**

Ingénieur des Arts et Manufactures (2003)

Ecole Centrale Paris (Châtenay-Malabry, France)

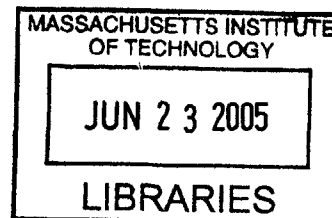
Submitted to the Department of Aeronautics and Astronautics  
in Partial Fulfillment of the Requirements for the Degree of

Master of Science in Aeronautics and Astronautics

at the

Massachusetts Institute of Technology

June 2005



© 2005 Massachusetts Institute of Technology  
All rights reserved

Author.....  
Department of Aeronautics and Astronautics  
May 20, 2005

Certified by.....  
Professor Alan H. Epstein  
R.C. Maclaurin Professor  
Department of Aeronautics and Astronautics  
Thesis Supervisor

Accepted by.....  
Professor Jaime Peraire  
Department of Aeronautics and Astronautics  
Chairman, Department Committee on Graduate Students

**AERO**



# **Aerodynamic Performance Measurements in a Counter-Rotating Aspirated Compressor**

by

Jean-François Onnée

Submitted to the Department of Aeronautics and Astronautics  
on May 20, 2005, in partial fulfillment of the  
requirements for the Degree of  
Master of Science in Aeronautics and Astronautics

## **Abstract**

This thesis is an experimental investigation of the aerodynamic performances of a counter-rotating aspirated compressor. This compressor is implemented in a blow-down facility, which gives rigorous simulation of the characteristic aerodynamic parameters in which a compressor operates in steady state conditions. To measure the efficiency of this unique machine, the total temperature as well as the total and the static pressures at the inlet and the outlet of the compressor are measured.

Due to the short test time ( $\sim 100$  ms) and unsteady nature of the blow-down environment, performance measurements in a short-duration test facility place especially demanding requirements on the accuracy and the response of the temperature and pressure sensors. For the total temperature probes, 0.0005-inch-diameter type-K thermocouple gage wires were assembled in specially designed casings allowing to perform measurements at determined span and circumferential locations. As for pressure probes, ultraminiature piezo-resistive transducers were used. The uncertainties related to their performances is estimated.

These results are then processed to obtain an estimation of the uncertainties in the efficiency measurement. The error related to the time-resolution as well as the discrete spatial sampling pattern are also assessed. The blow-down test facility provides a quasi-isothermal environment. The non-adiabatic effects lead to a biased efficiency measurement. A corresponding correction to estimate the adiabatic efficiency of the compressor is detailed. Finally, results from the first compressor test runs are provided.

Thesis Supervisor: Alan H. Epstein

Title: R.C. Maclaurin Professor of Aeronautics and Astronautics

Director of the Gas Turbine Laboratory



## **Acknowledgments**

I would like to thank Professor Alan H. Epstein and Dr. Gerald R. Guenette for having given me the opportunity to work on this innovative project. I am very grateful for their guidance, support and kindness during the course of this experimental work.

I would like to thank all the members of the blow-down counter-rotating aspirated compressor team, namely Professor Jack L. Kerrebrock, Dr. Ali Merchant, Dr. Fritz Neumayer and my fellow research student David V. Parker, for their teachings, support and precious help.

Many thanks to Jack Costa, Viktor Dubrowski and James Letendre for their help, patience and skills in turning my drawings into actual probes. I am also grateful to the entire GTL staff for their kindness.

I cannot express enough gratitude to my parents and my sister, whose love and support gave me the opportunity to earn this degree. I would like to address a special thought to my regretted grand-mother Mamama, for her love and supporting prayers throughout my studies.

Finally, I would like to thank all my friends, overseas, for their support, and here in the United States, for making these two years in New England a great experience.

This work was supported by the Defense Advanced Research Projects Agency, Dr. S. Walker, Manager.



# Contents

1. Introduction.....	19
1.1. Motivation.....	19
1.2. Objective and Approach .....	21
1.3. Thesis Outline .....	23
2. Experimental Facility.....	25
2.1. The Counter-Rotating Aspirated Compressor .....	25
2.2. The MIT Blow-Down Counter-Rotating Compressor Facility.....	28
2.3. Operation of the MIT Blow-Down Counter-Rotating Compressor .....	31
2.4. Instrumentation and Data Acquisition .....	32
2.4.1. Instrumentation used on the Facility.....	32
2.4.2. Data Acquisition Devices .....	35
3. Total Temperature Measurement.....	37
3.1. Introduction.....	37
3.2. Requirements for Total Temperature Probe in a Blow-Down Facility.....	38
3.3. Basic Theory of Thermocouple Technology .....	39
3.4. Total Temperature Probe Design.....	42
3.4.1. Probe Head Design and Model .....	42
3.4.2. Upstream and Downstream Total Temperature Single Probes.....	47
3.4.3. Upstream and Downstream Total Temperature Rakes .....	48
3.4.4. Mechanical Integrity within the Flow Conditions .....	50
3.4.5. Signal Conditioning .....	55
3.5. Static Calibration of Total Temperature Probes .....	56
3.5.1. Calibration Equipment.....	56
3.5.2. Calibration of Thermocouples .....	57
3.6. Uncertainty Estimation of Total Temperature Measurement .....	60
3.6.1. Recovery Error and Response Time .....	60
3.6.2. Conduction Error .....	62
3.6.3. Radiation Error.....	64

3.6.4.	Overall Uncertainty of Total Temperature Measurement.....	65
4.	Total Pressure Measurement.....	67
4.1.	Introduction.....	67
4.2.	Requirements for Total Pressure Probe in a Blow-Down Facility .....	68
4.3.	Total Pressure Design .....	69
4.3.1.	Isolated Pressure Measurement probes .....	69
4.3.2.	Total Pressure Rakes.....	69
4.3.3.	Signal Conditioning .....	70
4.4.	Probe Calibration .....	71
4.5.	Uncertainty Estimation of Pressure Measurement.....	71
5.	Aerodynamic Performance Measurement.....	77
5.1.	Introduction.....	77
5.2.	Uncertainty of Adiabatic Efficiency Measurement .....	79
5.2.1.	Uncertainty due to Instrumentation Imperfections .....	79
5.2.2.	Uncertainty Due to Discrete Spatial Sampling .....	81
5.2.3.	Uncertainty Due To Time Sampling.....	84
5.3.	Non-Adiabatic Effects in a Blow-Down Test Environment.....	84
5.3.1.	Difference Between Blow-Down Efficiency and Adiabatic Efficiency ...	85
5.3.2.	Correction to provide to Measured Efficiency.....	87
6.	Experimental Results .....	91
6.1.	Introduction.....	91
6.2.	Test Data .....	91
6.2.1.	Preliminary Tests .....	91
6.2.2.	Matched Corrected Speed Run Results.....	93
6.2.3.	Preliminary Compressor Map .....	106
7.	Conclusion .....	107
7.1.	Summary .....	107
7.2.	Future Work .....	109
8.	Appendix A: Detailed Calculation of the Correction Between Indicated and Adiabatic Efficiencies in a Blow-Down Test Facility.....	111

9.	Appendix B: Detailed calculation of the Total Temperature Probe Errors. ....	135
10.	Appendix C: Total Temperature Probes Drawings.....	145
11.	Appendix D: Total Pressure Probes Drawings .....	153
12.	Appendix E: Detailed Type-K Thermocouple Manufacturing Description .....	157



## List of Figures

Figure 1.1 - Effect of suction on boundary layer growth.....	20
Figure 2.1 – Inlet Guide Vane Mounted on Forward Section.....	25
Figure 2.2 – Rotor 1.....	26
Figure 2.3 – Rotor 2.....	27
Figure 2.4 - Bleed Flow Passage in a Rotor 2 Blade.....	27
Figure 2.5 – The MIT Blow-Down Compressor Facility.....	29
Figure 2.6 – Forward Test Section.....	30
Figure 2.7 – Aft Test Section.....	31
Figure 2.8 – Instrumentation Positions on Test Stand.....	34
Figure 3.1 – Thermocouple Circuit with External Reference Junction.....	41
Figure 3.2 – Ice Point Reference Chambers.....	41
Figure 3.3 – Thermocouple Head Design.....	43
Figure 3.4 – Infinite Cylinder with Initial Uniform Temperature Subjected to Sudden Convection Conditions.....	44
Figure 3.5 – Compressional Heating in the Blow-Down Seen by the Upstream Probes..	47
Figure 3.6 – Downstream Temperature Probe Mounted on Brass Plug.....	48
Figure 3.7 – Fully assembled upstream total temperature rake.....	50
Figure 3.8 – Schematic of Free Jet Resistance Test.....	51
Figure 3.9 – Picture of 0.0005-inch Thermocouple Gage.....	52
Figure 3.10 – Gage Wire Shapes Tested in the Free Jet Stand.....	52
Figure 3.11 – Wire response-time in (s) versus the Percentage of Load Reduction for ¼” heads by Decreasing the Vent Hole Size.....	54
Figure 3.12 – Evolution of the Recovery Error versus the Percentage of Load Reduction for ¼” heads, by Decreasing the Vent Hole Size.....	54
Figure 3.13 – Evolution in Conduction Error versus the Percentage of Load reduction by Decreasing the Inlet Area of a ¼” head.....	55
Figure 3.14 – Schematic of One-Dimensional Conduction-Convection Model for Thermocouple Wire.....	64

Figure 3.15 – Conduction Error Percentage, Predicted by a Steady State One-Dimensional Conduction-Convection Model.....	64
Figure 4.1 – Fully-Assembled Upstream Total Pressure Rake.....	70
Figure 5.1 – Inlet and Outlet Relative Entropy Variations.....	83
Figure 5.2 – Enthalpy – Entropy Diagram for the Compression Processes in Compressors.....	85
Figure 5.3 – Difference Between Adiabatic and Indicated Efficiency Over the Test Time.....	89
Figure 6.1 – Corrected Speeds During Test Time Normalized by Full Design Speed – Run 003.....	93
Figure 6.2 – Upstream Total Temperatures of Run 010.....	96
Figure 6.3 – Downstream Total Temperatures of Run 010.....	96
Figure 6.4 – Upstream and Downstream Radial Total Temperature Distribution at 250 ms, 300 ms and 350 ms for Run 010.....	97
Figure 6.5 – Area-Averaged Pressure History in the Supply Tank, the Valve, Upstream and Downstream of the Compressor, in the Bleed Flow and in the Dump Tank for Run 010.....	97
Figure 6.6 – Upstream Total Pressure at Three Midspan Locations for Run 010.....	98
Figure 6.7 – Upstream Static Pressure Distribution for Run 010.....	98
Figure 6.8 – Upstream Pitot Total and Static Pressures for Run 010.....	99
Figure 6.9 – Downstream Pitot Total and Static Pressures for Run 010.....	99
Figure 6.10 – Upstream Total Pressure Rake Measurements for Run 010.....	100
Figure 6.11 – Downstream Total Pressure Rake Measurements for Run 010.....	100
Figure 6.12 - Upstream and Downstream Radial Total Pressure Distribution at 250 ms, 300 ms and 350 ms for Run 010.....	101
Figure 6.13 – Pressure Ratio, Temperature Ratio and Efficiency Radial Distributions at 250 ms, 300 ms and 350 ms for Run 010.....	101

Figure 6.14 – High Speed Static Pressures Behind Rotor 1 (Blue) and Rotor 2 (Green) for Run 010.....	102
Figure 6.15 - High Speed Static Pressures Behind Rotor 1 (Blue) and Rotor 2 (Green) for Run 010 between 250 ms and 255 ms.....	102
Figure 6.16 – Upstream and Downstream Mach Numbers for Run 010.....	103
Figure 6.17 – Rotor 1 and 2 Normalized Corrected Speeds for Run 010.....	103
Figure 6.18 – Compressor Conditions During Test Time for Run 010.....	104
Figure 6.19 – Compressor Performance During Test Time for Run 010.....	104
Figure 6.20 – Preliminary Counter-Rotating Aspirated Compressor Map for Corrected Speeds Between 88% and 102%.....	106
Figure A.1. - Temperature Profile vs. $\eta$ Inside Rotor 1 at Various Time Points.....	117
Figure A.2. - Temperature Profile vs. $\eta$ Inside Rotor 2 at Various Time Points.....	118
Figure A.3. - Temperature Evolution at the Surface of the Leading Edge of Rotor 1 over 1s.....	118
Figure A.4. - Temperature Evolution at the Surface of the Leading Edge of Rotor 2 over 1s.....	119
Figure A.5. – Biot Number at Leading Edge (a) and Trailing Edge (b) of Rotor 1 over 1s.....	120
Figure A.6. - Biot Number at Leading Edge (a) and Trailing Edge (b) of Rotor 2 over 1s.....	121
Figure A.7. – Temperature Evolution at the Surface of the Leading Edge of Rotor 1 Over 1s.....	123
Figure A.8. - Temperature Evolution at the Surface of the Trailing Edge of Rotor 1 Over 1s.....	124
Figure A.9. - Temperature Evolution at the Surface of the Leading Edge of Rotor 2 Over 1s.....	124
Figure A.10. - Temperature Evolution at the Surface of the Trailing Edge of Rotor 2 Over 1s.....	125
Figure A.11. - Temperature Evolution at the Surface of the IGV Over 1s.....	125

Figure A.12. – Temperature Evolution of Rotor 2 Hub vs. Depth for Different Time Points (a) and vs. Time at the Surface (b).....	126
Figure A.13. - Temperature Evolution of Rotor 1 Hub vs. Depth for Different Time Points (a) and vs. Time at the Surface (b).....	127
Figure A.14. - Temperature Evolution of the Leading Edge Parts of Rotor 1 Blades vs. Depth for Different Time Points (a) and vs. Time at the Surface (b).....	128
Figure A.15. - Temperature Evolution of the Trailing Edge Parts of Rotor 1 Blades vs. Depth for Different Time Points (a) and vs. Time at the Surface (b).....	129
Figure A.16. - Temperature Evolution of the Leading Edge Parts of Rotor 2 Blades vs. Depth for Different Time Points (a) and vs. Time at the Surface (b).....	130
Figure A.17. - Temperature Evolution of the Trailing Edge Parts of Rotor 2 Blades vs. Depth for Different Time Points (a) and vs. Time at the Surface (b).....	131
Figure A.18. - Difference Between Adiabatic and Indicated Efficiency Over the Test Time.....	134
Figure B.1. – Radiation Error Evolution for the Upstream Probes, Over 1s.....	142
Figure B.2. - Radiation Error Evolution for the Downstream Probes, Over 1s.....	143
Figure C.1. – Upstream Rake Total Temperature Measurement Head.....	147
Figure C.2. – Downstream Rake Total Temperature Measurement Head.....	148
Figure C.3. – Upstream Total Temperature Measurement Probe.....	149
Figure C.4. - Downstream Total Temperature Measurement Probe.....	150
Figure C.5. – Upstream Total Temperature Measurement Rake Assembly.....	151
Figure C.6. – Downstream Total Temperature Measurement Rake Assembly (5 Head Model).....	152
Figure D.1. – Upstream Total Pressure Measurement Rake Assembly.....	155
Figure D.2. – Downstream Total Pressure Measurement Rake Assembly.....	156
Figure E.1. – Close-Up View of the Thermocouple Gage Wire Epoxied to the Ceramic Stem.....	160
Figure E.2. – View of the Thermocouple Extension Cables Laced Together in the Rake Airfoil Cavity.....	163

## List of Tables

Table 2.1 – Individual performances of each rotor predicted by CFD calculation.....	28
Table 2.2 – Overall compressor performances and back pressure setting predicted by CFD calculation.....	28
Table 3.1 – Specifications for the Rosemount Standard Platinum Resistance thermometer model 162N.....	57
Table 3.2 – Summary of Probes Geometries, Inner Mach Numbers, Recovery Errors and Time Responses.....	62
Table 3.3 – Detailed Summary of Thermocouple Probes’ Errors.....	66
Table 4.1 – Pressure Sensor Name Nomenclature.....	70
Table 4.2 – Upstream Total Pressure Uncertainty.....	74
Table 4.3 – Downstream Total Pressure Uncertainty.....	74
Table 4.4 – Total Upstream Static Pressure Error.....	74
Table 4.5 – Upstream Transducer Uncertainty.....	75
Table 4.6 – Downstream Transducer Uncertainty.....	76
Table 5.1 – Radial Sampling Uncertainty.....	82
Table 5.2. – Absolute and Relative Uncertainties in Total Temperature and Pressure Measurements for Runs 005 to 014.....	90
Table 5.3. – Scaling Coefficients, Scaled Uncertainties in Temperature, Pressure and Specific Heat Ratio and Efficiency Uncertainty for Runs 005 to 014.....	90
Table 6.1. - Compressor Initial Operating Conditions, Performances and State at 250 ms for Runs 005 to 014.....	105
Table B.1. – Casing Mach Number, Wire and Bead Response Times for the Upstream Probes at $t = 250$ ms and $t = 500$ ms.....	139
Table B.2. - Casing Mach Number, Wire and Bead Response Times for the Downstream Probes at $t = 250$ ms and $t = 500$ ms.....	140



## Nomenclature

$a$	Sound velocity, m/s
$A_c$	Thermocouple wire cross-sectional surface area
$Bi$	Biot number
$C_p$	Specific heat at constant pressure
$E_{rec}$	Recovery Error
$F_0$	Fourier number
$h$	Heat transfer coefficient, W/m <sup>2</sup> K – Enthalpy, J/kg
$h_{01}$	Inlet total enthalpy, J/kg
$h_{02,ad}$	Outlet total enthalpy for an adiabatic compression, J/kg
$h_{02,ind}$	Indicated outlet total enthalpy, J/kg
$h_{02,is}$	Outlet total enthalpy for an isentropic compression
$k$	Thermal conductivity, W/mK
$L$	Thermocouple wire length exposed to the flow, m
$m$	Characteristic spatial frequency of the heat equation of one-dimensional steady state conduction-convection transfer, 1/m <sup>2</sup>
$M$	Mach number
$\dot{m}$	Mass-flow rate, kg/s
$p$	Static pressure, Pa
$P$	Thermocouple perimeter, m
$P_s$	Static pressure, Pa
$P_t$	Total pressure, Pa
$P_{01}$	Inlet total pressure, Pa
$P_{02}$	Outlet total pressure, Pa
$r$	Thermocouple radius variable, m – Recovery factor
$r_0$	Thermocouple nominal radius, m
$r^*$	Thermocouple non-dimensional radius
$t^*$	Dimensionless time
$T$	Thermocouple temperature pattern, K

$T_i$	Thermocouple initial temperature, K
$T_s$	Static temperature, K
$T_t$	Total temperature, K
$T_{t,ind}$	Indicated total temperature, K
$T_{t,j}$	Junction total temperature, K
$T_{surr}$	Thermocouple casing temperature, K
$T_{wall}$	Wall temperature, K
$T_{01}$	Inlet total temperature, K
$T_{02,ad}$	Outlet total temperature for an adiabatic compression, K
$T_{02,ind}$	Indicated outlet total temperature, K
$T_{02,is}$	Outlet total temperature of an isentropic compression, K
$T_\infty$	Free flow temperature, K
$V$	Flow velocity, m/s
$W_a$	Actual work provided to the compression, W
$W_{ideal}$	Ideal compressor work, W
$x$	Thermocouple gage length variable, m

### Greek Symbols

$\gamma$	Specific heat ratio
$\varepsilon$	Emissance
$\eta_c$	Compressor efficiency
$\eta_{ind}$	Indicated efficiency obtained from direct measurements
$\theta$	Difference between thermocouple and gas temperatures, K
$\nu^*$	Dimensionless temperature
$\pi_c$	Compressor pressure ratio
$\rho$	Flow density, kg/m <sup>3</sup>
$\sigma$	Stefan-Boltzmann constant, W/m <sup>2</sup> K <sup>4</sup>
$\tau$	Temperature ratio

# 1. Introduction

## *1.1. Motivation*

Over the past 40 years, the aerodynamic performances of conventional compressors have increased enormously, thanks to the development of several enhancing design methodologies. But beyond those methods, the idea of developing compressors capable of achieving higher pressure ratios thanks to higher rotating velocities continued to make its way. The idea of a counter-rotating compressor is a case in point in that matter. Replacing the traditional stator by a rotor rotating in the opposite direction of the preceding rotor is a technique that would allow higher relative velocities and hence higher pressure ratio. But this technique alone is not efficient as high turning flows result in separation of the flow from the blades' surface on the second rotor. It is in this context that the concept of aspiration comes to play a role.

For the past 10 years, the prospects for aspirated compressors have become a center of focus for research laboratories. Studies have been able to prove the benefits of this technique. It allows one to reduce the amount of low energy fluid around the blades, which is tantamount to decreasing in the boundary layer thickness, as shown in Figure 1.1. The work available at a given tip speed can hence be increased, which expands the design space for compressor stages. The related benefits is either a higher pressure ratio

per stage, or a lower blade speed for a given pressure ratio, or a compromise between the two. More information can be found in [1]. This breakthrough technique has enabled to create blades capable of remaining efficient when submitted to high turning flows, perfectly suitable for a counter-rotating assembly. The envisioned benefits of this breakthrough technique include high pressure ratios per stage and shorter and lighter machines. The synergy with counter-rotating turbines can be underlined in this context.

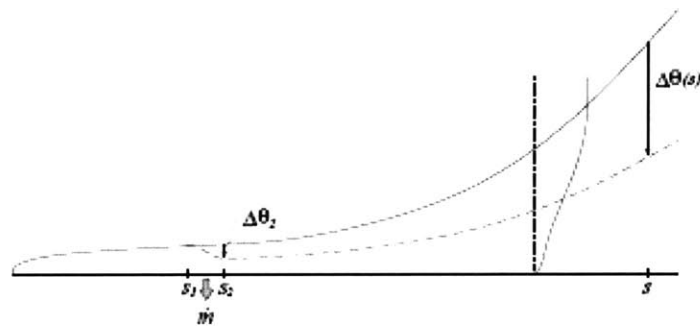


Figure 1.1 - Effect of suction on boundary layer growth

Since the early 1970's, MIT has performed and developed many short-duration blow-down tests on turbines and compressors. The technology is based on transient testing techniques that are able to provide highly accurate data at a relatively low cost. Using proper scaling of the facility, it is possible to reproduce and measure the flow's non-dimensional parameters that characterize the compressor in a steady operating mode. The actual testing time of the compressor is hence quite short, on the order of 400-500ms. This allows the total energy consumption to be kept at a low level. Meanwhile, the building and maintenance costs of the short-duration rig are greatly reduced in comparison to a traditional test stand.

These are the justifications that fostered the conception, design and operation of a counter-rotating aspirated compressor in a blow-down testing facility at the Gas Turbine Laboratory. This thesis deals with the aerodynamic performance measurements of this compressor. We can already state here that high frequency response instrumentation is a

key requirement for this testing configuration. A detailed description of the design and the characteristics of these instruments will be provided in the next chapters. The associated error analysis will be provided as well. Testing in transient conditions implies a certain number of consequences in the interpretation of the measured efficiency. The difference between steady state test measured efficiencies and transient test measured efficiencies will be addressed.

## ***1.2. Objective and Approach***

The objective of the experiment is to determine the efficiency of a one-stage counter-rotating aspirated compressor. From thermodynamic considerations, for a given total pressure ratio  $\pi_c$  the efficiency of a compressor is defined as:

$$\eta_c = \frac{W_{ideal}}{W_a} \quad (1.1)$$

where  $W_{ideal}$  is the ideal work of compression for that given  $\pi_c$  in isentropic conditions and  $W_a$  is the actual work of compression applied to achieve the same total pressure ratio.

Assuming the gas is ideal and the mass-flow as well as the specific heat ratio are constant through the compressor, the ideal work of compression can be calculated as:

$$W_{ideal} = \dot{m} C_p T_{01} \left( \left( \frac{P_{02}}{P_{01}} \right)^{\frac{\gamma-1}{\gamma}} - 1 \right) \quad (1.2)$$

where  $\dot{m}$  is the mass flow rate,  $C_p$  is the constant pressure heat coefficient,  $T_{01}$  and  $P_{01}$  are the total temperature and total pressure of gas at the inlet of the compressor,  $P_{02}$  is the total pressure of gas at the exit,  $\gamma$  is the specific heat ratio.

Defining the actual way for a compressor is a more intricate problem. In steady state, a compressor runs under adiabatic conditions and its work can be written as:

$$W_a = \dot{m} C_p (T_{02,ad} - T_{01}) \quad (1.3)$$

where  $T_{02,ad}$  is the total temperature of gas at the exit of a compressor in an adiabatic process. This expression is valid under the same conditions stated for equation (1.2).

Following those definitions, the latter process-defined actual work (1.3) leads to the most commonly used definition of adiabatic compressor efficiency. It can be written as:

$$\eta_{ad} = \frac{\pi_c^{\frac{\gamma-1}{\gamma}} - 1}{\tau - 1} \quad (1.4)$$

where:

$$\pi_c = \frac{P_{02}}{P_{01}} \quad (1.5)$$

$$\tau = \frac{T_{02}}{T_{01}} \quad (1.6)$$

Equation number (1.4) tells us that in order to make an efficiency measurement, it is sufficient to know the aerodynamic parameters at the inlet and the outlet of a compressor and to know the thermodynamic properties of the gas. So measuring the inlet and outlet total temperatures and total pressures would give the answer for the adiabatic efficiency of a compressor.

It is however very important to recall here that a blow-down facility does not provide the testing conditions for the previous efficiency calculation to be led in a straightforward manner. A blow-down compressor works in non-adiabatic conditions and in unsteady or quasi-steady conditions both in terms of aerodynamic parameters of the flow and in terms of thermodynamic properties of the gas. The efficiency was thus computed by calculating the isentropic enthalpy rise and the actual enthalpy rise of the gas mixture, based on the measured data:

$$\eta_{ind} = \frac{h_{02,is} - h_{01}}{h_{02,ind} - h_{01}} \quad (1.7)$$

The common approach to describing compressor performance is to quote their adiabatic efficiency. As explained earlier, a blow-down test facility cannot directly yield this information. It is then also mandatory to try and assess the amount of difference

between the indicated efficiency, and the efficiency the compressor would have had for the same operating point, had it been tested in adiabatic and steady state conditions. This subject will be analyzed in chapter 5 and 6.

### ***1.3. Thesis Outline***

The remainder of the thesis is organized into the following chapters.

Chapter 2 describes the experimental facility. A description of the Counter-Rotating Aspirated Compressor is given along with a brief explanation of the blow-down compressor test rig operations. The accuracy requirements for temperature measurement along with the temperature sensors development, design and calibration processes and the assessment of their performances are covered in chapter 3. Chapter 4 focuses on the pressure measurements. The total pressure probe design and calibration are shown along with the uncertainty associated to their data measurements. The following chapter deals with efficiency computation and more precisely with the evaluation of the difference of efficiency measurements between a short-duration test and a steady state test. Experimental results are provided in chapter 6 and they are followed by a final summary and conclusion in chapter 7. Further detailed information related to the error analysis of the temperature probes and efficiency measurements are given in appendix, along with detailed instructions and drawings of the manufacturing process of those probes.



## **2. Experimental Facility**

This chapter provides a description of the Counter-Rotating Aspirated Compressor and the experimental facility used to measure its aerodynamic performances. The configuration and operation during a typical run are described, along with the instrumentation probes and the data acquisition systems.

### ***2.1. The Counter-Rotating Aspirated Compressor***

The counter-rotating aspirated compressor consists of 3 rotating parts, namely an IGV, rotor 1 and rotor 2.

The IGV is made of 35 blades, bound together by a one-piece annular shroud.

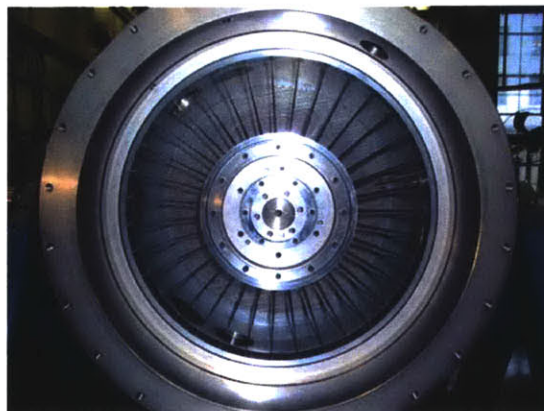


Figure 2.1 – Inlet Guide Vane Mounted on Forward Section.

Rotor 1 consists of 20 un-shrouded blades.

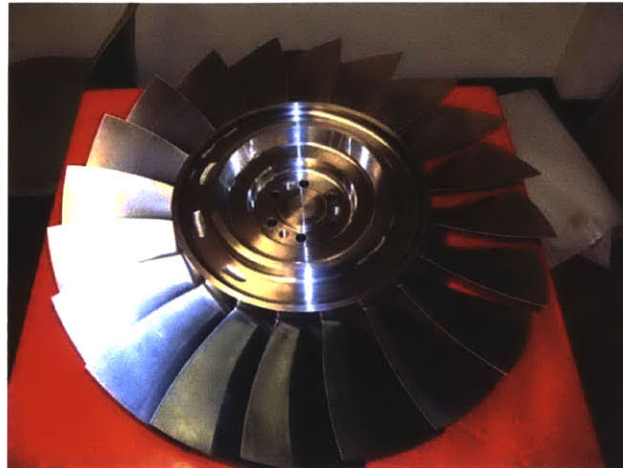


Figure 2.2 – Rotor 1.

Rotor 2 is the aspirated feature of this compressor. It is indeed counter-rotating with respect to rotor one. It is confronted by a high turning flow and must hence accommodate the aspiration system that will remove the bulk of the low energy part of the flow on the suction surface, by aspirating the boundary layer. Rotor 2 consists of 29 blades designed with aspiration slots on their suction side and a channel to drive the flow out of the core flow, towards the bleed flow (Figure 2.3 and Figure 2.4). In the blow-down facility, the rotating parts are placed in vacuum. The flow is then rapidly released in the rig. Suction relies on the pressure difference between the incoming flow and the rest of the facility sitting in vacuum.



Figure 2.3 – Rotor 2.



Figure 2.4 - Bleed Flow Passage in a Rotor 2 Blade.

Table 2.1 and Table 2.2 summarize the predicted performance of each rotor as well as the entire compressor at for different operating points. These results are based on CFD calculations performed by Ali Merchant at MIT and engineers at APNASA, assuming the throttle opening length ensure the appropriate back pressure. The goal of this experiment is to try to verify experimentally these predictions.

Speeds	Rotor 1			Rotor 2		
	PR 1	TR 1	Eff 1 (%)	PR 2	TR 2	Eff 2 (%)
100-100	1.91	1.23	89	1.60	1.16	89
95-95	1.78	1.21	87	1.44	1.12	89
90-90	1.68	1.18	85	1.37	1.13	74
85-85	1.60	1.17	84	1.36	1.12	76
80-80	1.50	1.15	81	1.29	1.10	78

Table 2.1 – Individual performances of each rotor predicted by CFD calculation.

Speeds	Both			Throttle Length (in)
	PR	TR	Eff (%)	
100-100	3.06	1.43	87	3.53
95-95	2.57	1.36	85	3.50
90-90	2.30	1.33	82	3.50
85-85	2.17	1.31	81	3.60
80-80	1.93	1.26	80	3.75

Table 2.2 – Overall compressor performances and back pressure setting predicted by CFD calculation.

## ***2.2. The MIT Blow-Down Counter-Rotating Compressor Facility***

The tests to investigate the aerodynamic performance of the counter-rotating aspirated compressor were performed on a blow-down compressor test rig. The non-dimensional equations of continuity, motion and energy show that it is the ratio of forces, fluxes and states that determine the flow field. Hence, only the non-dimensional parameters characterizing the steady state running conditions need to be reproduced to simulate the engine operation. Those parameters are the corrected mass flow, the corrected speed, the ratio of specific heat, the Mach number at the inlet and the outlet of the compressor, and, to a lesser extent, the Reynolds number. The blow-down test rig has been designed and dimensioned so as to maintain these non-dimensional parameters approximately constant over the test period, matching the values these parameters would have in steady state. This section only purports to give a brief description of the blow-down compressor facility. Details of the rig design and operations can be found in [2].

Several design requirements and constraints applied to the design of the testing facility. One of them is the urban location of MIT, which required keeping all operating stresses within safe limits. This aspect accounted partly for the type of gas used in the

tunnel. A mixture of Argon and CO<sub>2</sub> was chosen. The mixture ratio is set by the desired specific heat ratio  $\gamma$ . This choice presented several advantages over a classic air mix. The Argon-CO<sub>2</sub> mixture has a larger density, which allows the compressor rotors' physical speeds to be lower for a given corrected speed than if the test gas had been air. The facility can hence be operated at a lower level of stress in the blades, the disks, the blisks and the flywheel and other rotating parts.

Figure 2.5. shows the blow-down compressor facility. It breaks down into five major components: the supply tank, the fast-acting valve, the forward test section, the aft test section and the dump tank.

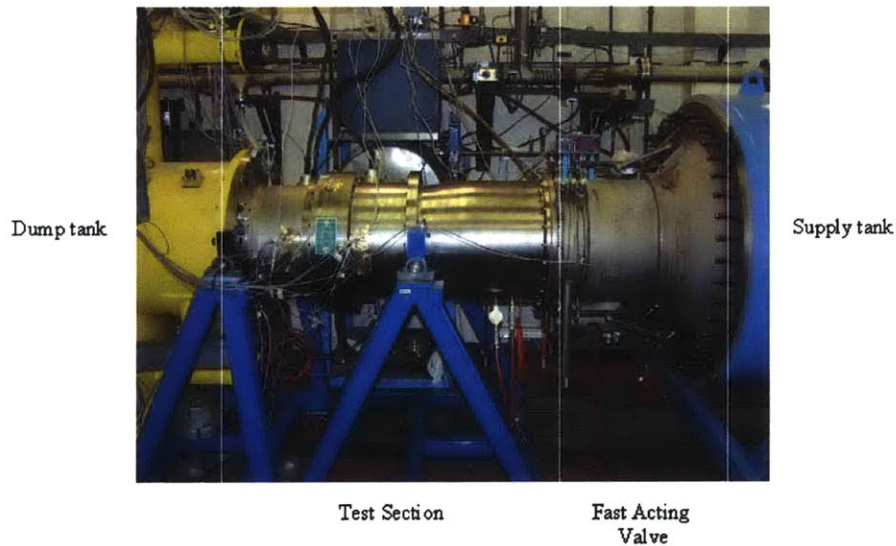


Figure 2.5 – The MIT Blow-Down Compressor Facility.

The supply tank has a volume of 157 ft<sup>3</sup> and can safely hold pressures up to 100 psia. It sits on wheels.

The fast acting valve separates the supply tank filled with gas, from the test sections and the dump tank sitting in vacuum. It was designed to open in less than 50 ms and provide a smooth expansion path for the gas exiting the tank. It is followed by a screen designed to set the appropriate pressure and mass-flow, as well as uniform inlet conditions in the inlet plane of the compressor.

The forward test section houses the IGV and the first rotor, as well as its drive motor and flywheel. It also houses a pressure screen aimed at imposing the correct pressure and mass flow upstream of the rotors. The motor and the flywheel are mounted on the same shaft as rotor 1, which imposed tight requirements in the design of those parts and their fitting in the inner diameter of the flow-path section. The flywheel is aimed at providing the rotor with the necessary inertia during its coasting phase to match the required corrected speed. Figure 2.6 shows a cross-sectional view of the forward test section.

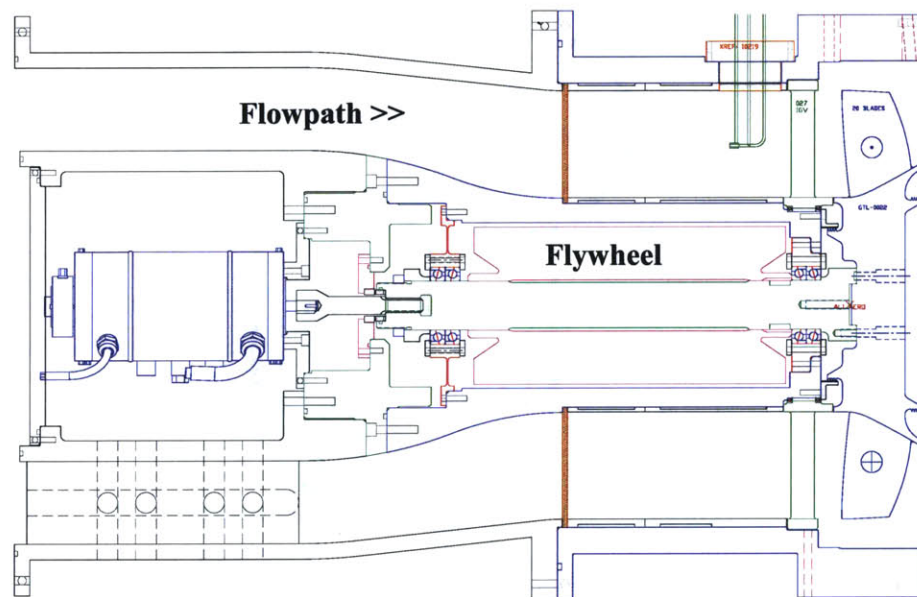


Figure 2.6 – Forward Test Section.

The aft test section houses the counter-rotating aspirated rotor with its rotating system and the throttle. Here again, the rotating system is mounted inside the inner diameter of the flow-path, which splits into two parts, the main path and a bleed flow passage. The flow path ends in the throttle, which sets the corrected flow. Figure 2.7 shows a cross-sectional view of the aft test section

Finally the dump tank is a 570 ft<sup>3</sup> tank bolted to the ground.

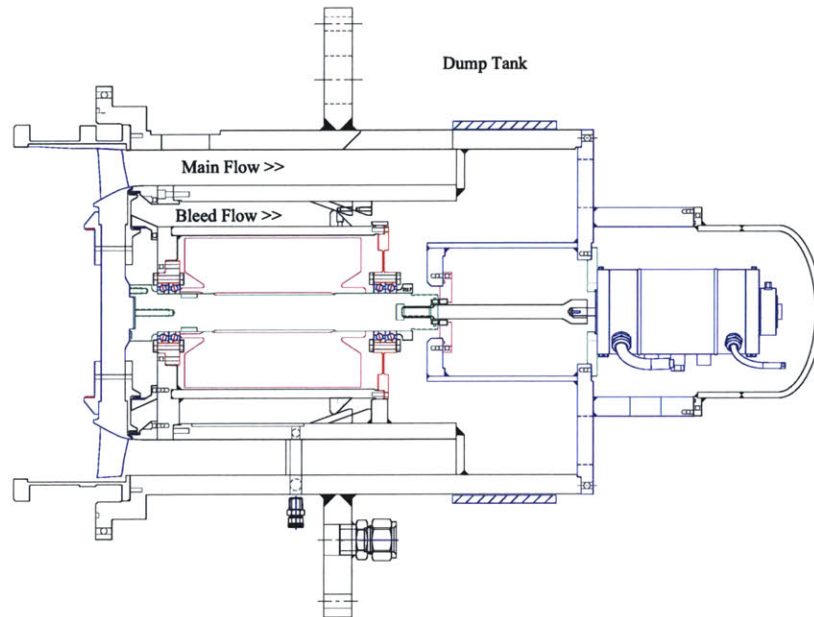


Figure 2.7 – Aft Test Section.

In the forward test section, as well as in the aft one, there are seven instrumentation window ports for access to the flow field. Each set consists of 2 sets of three windows equally spaced 120degrees apart. These two sets of three windows are rotated 20 degrees away from one another. The last windows are located on the bottom of the test cross-section. These windows are used to hold the total and static pressure probes as well as the total temperatures probes. Additional pressure sensors are placed further upstream and further downstream of the rotors.

### ***2.3. Operation of the MIT Blow-Down Counter-Rotating Compressor***

A brief description of the operation of the blow-down compressor is given in this paragraph. First, the tunnel is evacuated by an external vacuum system. Pressure probes then undergo a first calibration procedure. Once this calibration is done, the fast acting valve is closed. CO<sub>2</sub> is then loaded in the supply tank. Argon is later added to get the appropriate mole fractions and pressure. The pressure transducers are calibrated a second time. The two rotors are then spun up to the desired speeds. The A/D system is armed. The two rotors are then set to coast and the firing circuitry is triggered immediately after.

The fast-acting valve opens and releases the gas mixture in the tunnel. At the same time, the A/D system starts acquiring data. Both rotors are decelerated under the gas friction. After a transient mode of 200 milliseconds, the non-dimensional parameters characterizing the flow are maintained in a quasi-steady state for 300 milliseconds. The throttle un-chokes 700 milliseconds after the firing circuitry has been triggered, which marks the end of the test. The data acquisition system keeps on recording data for 1,300 milliseconds more. The rotors are finally braked and the pressure transducers are calibrated for a third and last time. The entire tunnel is eventually vented to atmosphere.

## ***2.4. Instrumentation and Data Acquisition***

### **2.4.1. Instrumentation used on the Facility**

The MIT blow-down compressor is instrumented with many advanced flow sensors.

The supply tank is fitted with a total pressure transducer and a Sensotec 150psig gage. A pressure transducer records the total pressure between the valve and the screen.

Upstream from the IGV, 5 of the 7 pressure plugs are fitted with instrumentation. The A, B and C windows, which are 120 degrees apart, are each fitted with a static and a total pressure probe as well as Pitot probes. Each probe is hooked to piezoresistive differential Kulite transducer. These window plugs all carry a total temperature probe. These probe heads shelter 0.0005-inch-diameter type-K thermocouples, which have sufficient response time to be able to record the compressional heating of the start-up transient of the blow-down tests. A detailed description of the design, the calibration and the uncertainties linked to the probes is given in chapters 3 and 4. An 8-probe total pressure probe rake is mounted one the windows, while an 11-probe total temperature probe rake is mounted at the same axial location but 120 degrees apart from the pressure rake. All these probes are oriented in a straight direction to face the incoming flow.

Downstream of the compressor, there is only one plug used to carry the single pressure and total temperature probes. The reduction in flow passage lead to the design of two rakes for both the temperature and the pressure measurements instead of one

upstream. The temperature rakes have 5 and 6 heads while the pressure rakes carry 5 impact heads each. For each type of measurement, the two rakes are located within the same angular sector. These rakes as well as the other total measurement probes can be rotated to account for the swirl coming out of the second rotor.

In order to detect any stall on the rotors, a high-speed static pressure probes have been set up behind each rotor.

A three-way wedge probe is mounted in the bleed flow passage, while a static sensor records the pressure in the dump tank, along with a Sensotec 050 device.

Figure 2.8 gives detailed view of the instrumentation display on the rig.

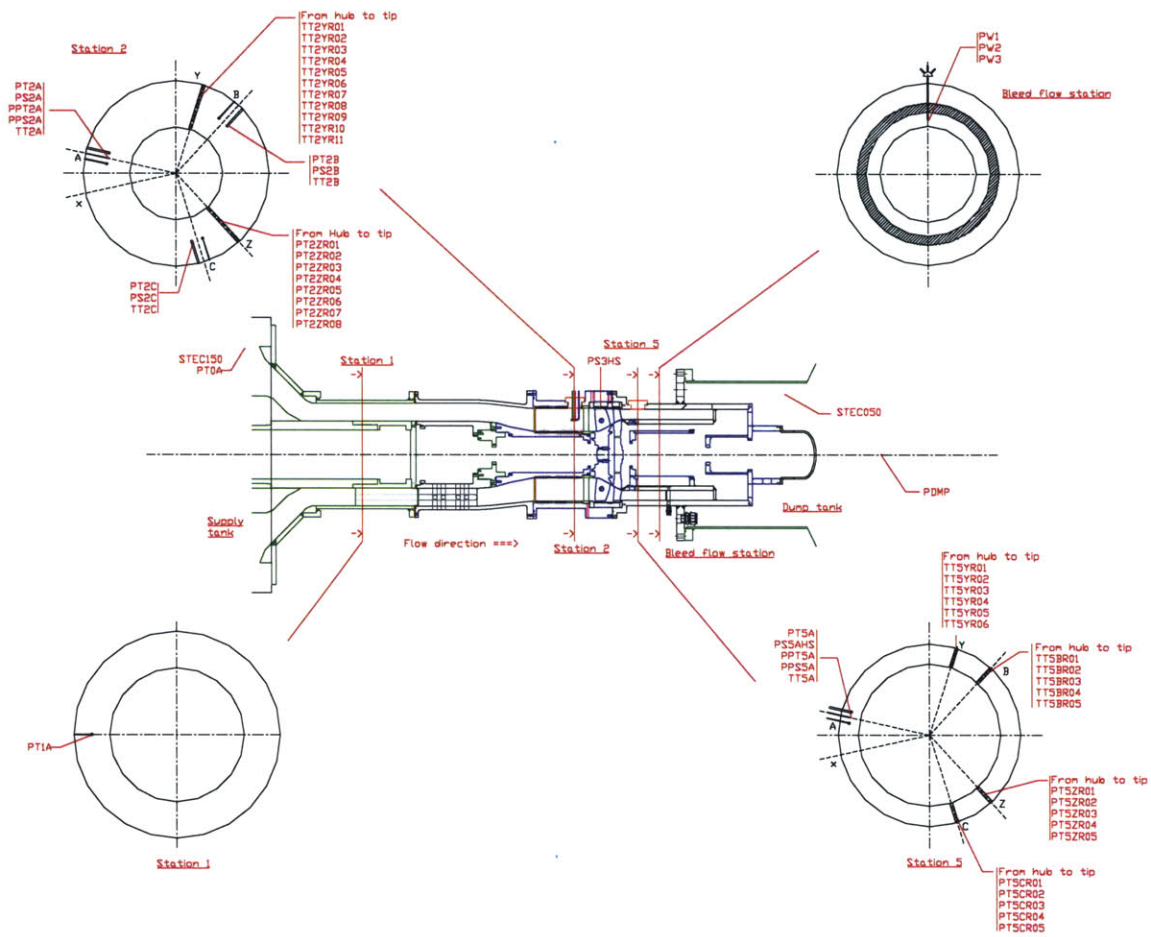


Figure 2.8 – Instrumentation Positions on Test Stand.

### **2.4.2. Data Acquisition Devices**

Though a blow-down test lasts only 1 second, an impressive amount of test data is sampled and taken into computer memories. For sampling purpose, a central data acquisition system is employed on the test facility. This system is fitted with two types of A/D cards:

1. Two National Instruments PCI-6031E 64-analog-channel 16-bit-analog cards were used for the thermocouple and the pressure sensors. The sampling frequency of these systems was set to 1,000 Hz over 2 seconds.[18]

2. A National Instruments PCI-6143 8-analog-channel 16-bit A/D card with a 100 kHz sampling frequency per channel. This card is used to record high speed data from static pressure located behind each rotor. [19]

A National Instruments PCI-6602 8-channel 32-bit counter card with an 80 MHz maximum sampling rate was installed on the data acquisition computer to record the speeds of the two rotors. [20]

These cards were mounted on a Dell x86 computer, equipped with a 260 MHz processor and offering 332 kB of RAM.

High sampling Data acquisition is a delicate process that can cause buffer saturation. In order to avoid any risk of losing control on the rotors which could result in serious accidents, the motor drive monitoring system was installed on a completely independent computer. This computer was a Dell x86 with a 65 MHz processor and 60 kB RAM. An RS-422 interface card was mounted on this computer to communicate with the Yaskawa GPD 515/G5 controlling the operating mode and settings of the drive motors.



## **3. Total Temperature Measurement**

### ***3.1. Introduction***

The purpose of this experiment is to determine the aerodynamic performances of the counter-rotating aspirated compressor. This approach requires the determination of the total temperature and the total pressures of the compressor. The transient testing conditions impose these instrument pieces to have an extremely short time-response so to be able to capture and record the entire data during the one second test time. The total temperature measurements rely on type-K thermocouples. The design and the manufacturing of those elements are based on the probe concept developed for the MIT Blow-down Turbine and described in [3].

This chapter first lists the requirements for the design of the total temperature measurement probes in a blow-down facility. A brief description of the basic theory of thermocouple technology is detailed, followed by a thorough description of the thermal model used to design the different probes. The manufacturing and robustness test processes are then detailed, followed by a description of the static calibration experiments. Finally, uncertainties involved in the probe data measurements are addressed.

### ***3.2. Requirements for Total Temperature Probe in a Blow-Down Facility***

In a traditional steady state test, the inlet and outlet total temperatures remain constant over the testing time, which is very long compared to the frequency response of the probes. But in the case of a blow-down test rig, the experiment aims at analyzing the behavior of the rotating assembly during a very short transient state, where the non-dimensional parameters characterizing the flow conditions are maintained constant. In that purpose, the type and requirements imposed on the instrumentation characteristics differs widely from a conventional testing environment. There is a strong requirement for very fast response total temperature probes. In the present case, the fast-acting valve opens within 50 ms, a compressional heating occurs for the next 200 ms before the set of data starts recording useful values where the quasi-steady test conditions are simulated. So the total temperature probes are supposed to reach to the gas temperature before the quasi-steady period starts and they are required to be fast responsive so that it can record the real-time changes in flow temperature.

As will be discussed in chapter 5, the uncertainty of temperature measurement plays a key role in the estimation of the efficiency measurement uncertainty. The influence coefficient due to the temperature measurement error weighs approximately three times more than that due to pressure measurement error. The goal of this work is to measure total temperature with less than 0.180 K upstream and 0.352 K downstream.

It is also very important that the design of the probes allows recording the total temperature of the flow. The design of the casing, the rakes and the plugs should allow the orientation of the heads to ensure that they face the flow and record the total parameters. This is less of an issue for the upstream probes, as the flow is filtered by a pressure screen which is here to guarantee the uniformity of the incoming flow. The downstream conditions are however different, as the counter-rotating nature of the compressor is bound to trigger vortices and swirls in the facility.

### ***3.3. Basic Theory of Thermocouple Technology***

The theory behind thermocouple technology was discovered and developed by Thomas Johann Seebeck in 1821. He carried an experiment joining two wires of dissimilar metals (a copper wire and a bismuth wire) and noticed that the temperature difference between the two junctions led to the generation of an electromotive force in the closed loop, resulting in a continuous electric current. This experiment was then verified with a set of dissimilar metals that form the thermoelectric series. Research showed that a bijective relation exists between the voltage inside the closed circuit made of any pair of thermoelectric metals and the temperature gradient between the two junctions binding them. The detailed theory of thermocouple can be found in [4]. Here, we present three fundamental laws of thermoelectric circuits:

1. A thermoelectric current cannot be sustained in a circuit of a single homogeneous material, however varying in cross section, by application of heat alone. This law implies that two different metals are required at least to form a thermocouple circuit.
2. The algebraic sum of the thermo-electromotive forces in a circuit composed of any number of dissimilar materials is zero if all the circuit is at a uniform temperature. A direct consequence to this law is that a third homogeneous material can be added inside the loop without modifying the net electromotive force as long as its extremities are maintained at the same temperature.
3. If two dissimilar homogeneous metals produce a thermal electromotive force of  $E_1$ , when the junctions are at  $T_1$  and  $T_2$ , and a thermal e.m.f. of  $E_2$ , when the junctions are at  $T_2$  and  $T_3$ , the e.m.f. generated when the junctions are at  $T_1$  and  $T_3$  will be  $E_1+E_2$ .

Two consequences can be induced from this last law. First, a thermocouple can be calibrated for a particular reference temperature and used with any other temperature reference provided an adequate correction is applied. Second, extension wires can be added to the thermocouple circuit without affecting the net e.m.f., provided they are of

similar nature, i.e. bear the same thermoelectric characteristics as the wires forming the thermocouples.

Standard thermocouple tables are provided for 0°C reference temperatures, that is when the reference junction is maintained at 0°C. In the case an external reference junction cannot be used, a proper use of the last two laws along with the standard thermocouple tables for the adequate thermoelectric metal pair, allows to compute the absolute temperature of the measuring junction. The details are given in [3]. It is very important to notice that, during a measurement or a set of measurements, the temperature of the reference junction must be maintained as constant as possible. When an external 0°C reference junction is used, the voltage reading can directly be input in the standard thermocouple tables to determine the corresponding temperature of the measuring junction. For this experiment, five Ice Point Reference Junction Omega TRCIII capable of accommodating six thermocouple reference points each, are used (Figure 3.2). These devices are designed, calibrated and certified to maintain 0°C at an accuracy of  $\pm 0.1^\circ\text{C}$  and a stability of  $\pm 0.04^\circ\text{C}$  for constant ambient [15].

When a filter or an amplifier are used to enhance the signal output, it is necessary to proceed to the calibration of the thermocouple probe and the corresponding reference cell, so as to account for the imperfections in the signal treatment and also the imperfections and impurities associated with the thermocouple manufacturing.

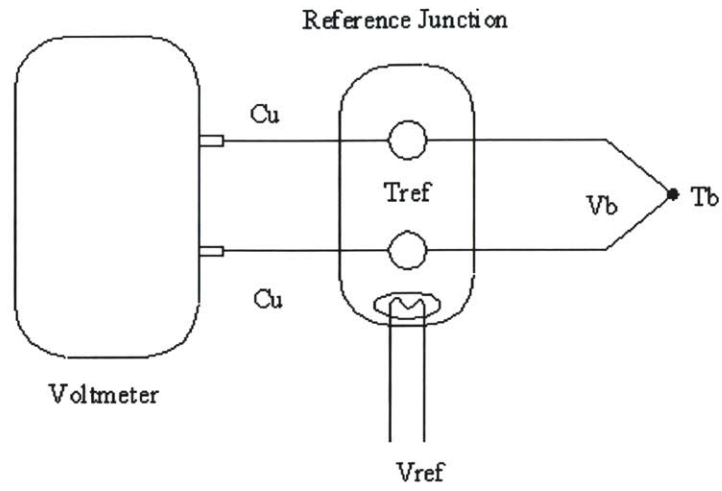


Figure 3.1 – Thermocouple Circuit with External Reference Junction.



Figure 3.2 – Ice Point Reference Chambers.

### ***3.4. Total Temperature Probe Design***

#### **3.4.1. Probe Head Design and Model**

The probe head design and model are directly inspired from the endeavors and researches done over fast response thermocouple probes on the MIT blow-down turbine project. As is detailed in [3], thermocouple probes are subject to a number of error sources. These sources stem from the heat conduction from the wire and the supporting ceramic stems, the radiation of the casing, the recovery aspects and the calibration procedures. The response time is also an aspect which shall not be neglected in a short duration testing facility.

As was the case on the blow-down turbine project, type-K thermocouple gages were chosen for this project, because of their enduring stability and linearity. In order to reduce the response time of each probe, 0.0005 inch diameter thermocouple wires were chosen. This type of wire happens to be the smallest thermocouple wire size available on the market. As shown on Figure 3.3, the thermocouple bead is located in the middle of the probe. The wire is held straight between two ceramic stems to which it is epoxied. This assembly is inserted into a protecting casing regulating the flow speed around the gage. The sensor wires are soldered to thicker thermocouple extension wires at the other end of the insert. This design encompasses several advantages. First and foremost, exposing a significant length of the thermocouple gage allows significant reduction in the conduction error. The thermocouple wires are subjected to the same flow and temperature conditions as the junction, which reduces the temperature gradient on either side of the bead. A more detailed calculation of that phenomenon will be given in section 3.6.2. A second aspect is related to the structural resistance of the probe to the jet flow. As has been observed on previous MIT blow-down experiments as well as on the mechanical integrity probe tests conducted for this project (see section 3.4.4.), hanging the thermocouple gage in a straight and softly stretched manner between the two stems prevents the wires from being damaged by the turbulence enticed by the flow inside the casing. These flow disturbances can lead to the gage rupture near the bead, where the

strongest stress conditions are applied. Finally, the casing ensures not only a protection of the thermocouple gage from hazardous manipulations, but thanks to a vent hole system, it allows to significantly reduce the speed of the flow around the gage.

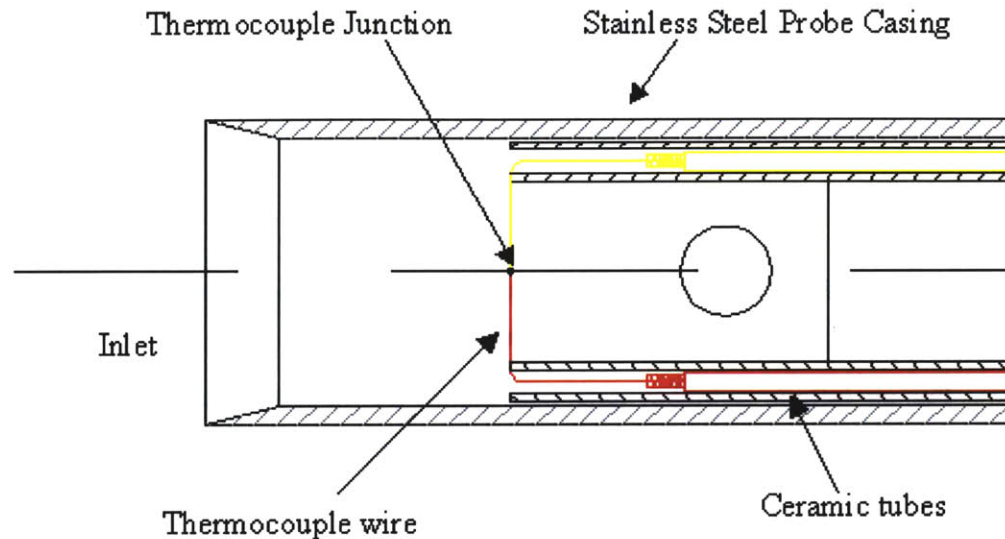


Figure 3.3 – Thermocouple Head Design.

In the case of a short duration blow-down test, determining the time response of the probe is equivalent to determining how quickly the center of the thermocouple gage wire reaches the temperature imposed by the test gas surrounding it. Practically, we try to determine the time required for that centerline point temperature to be within 1% of the flow temperature.

As a secondary consequence of the choices made to reduce the conduction error of the probe, the length of the gage exposed to the flow is much larger than the wire diameter. This geometrical consideration validates the infinite cylinder heat transfer theory as an appropriate model to compute the cross-sectional transient conduction inside the gage wires. References for that model can be found in [7].

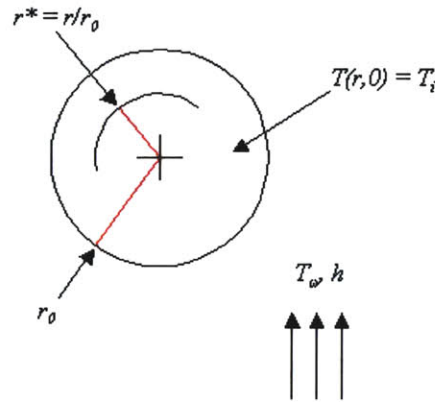


Figure 3.4 – Infinite Cylinder with Initial Uniform Temperature Subjected to Sudden Convection Conditions.

For an infinite cylinder, only one spatial coordinate is needed to describe the internal temperature distribution. The heat equation is reduced to:

$$\frac{\partial^2 T}{\partial r^2} = \frac{1}{\alpha} \cdot \frac{\partial T}{\partial t} \quad (3.1)$$

In order to solve this equation, it is necessary to specify one initial and two boundary conditions. The initial condition is:

$$T(r,0) = T_i \quad (3.2)$$

and the boundary conditions are:

$$\left. \frac{\partial T}{\partial r} \right|_{r=0} = 0 \quad (3.3)$$

and

$$-k \left. \frac{\partial T}{\partial r} \right|_{r=r_0} = h[T(r_0, t) - T_\infty] \quad (3.4)$$

where  $h$  is the convection heat transfer coefficient and  $k$  is the thermal conductivity of the thermocouple wire.

Equation (3.2) supposes that the temperature distribution inside the wire is uniform. Equation (3.3) defines the radial symmetry of the problem and equation (3.4) describes the convective heat exchange at the surface of the gage wire for any  $t > 0$ .

A practical way of solving this problem is to define the equation involving the non-dimensional forms of the dependent variables. These dimensionless variables are:

$$\nu^* \equiv \frac{T - T_\infty}{T_i - T_\infty} \quad (3.5)$$

The dimensionless form of the spatial coordinate is:

$$r^* \equiv \frac{r}{r_0} \quad (3.6)$$

As for the time variable, it is replaced by the Fourier number:

$$t^* \equiv \frac{\alpha \cdot t}{r_0^2} \equiv F_0 \quad (3.7)$$

The problem hence becomes:

$$\frac{\partial^2 \nu^*}{\partial r^{*2}} = \frac{\partial \nu^*}{\partial F_0} \quad (3.8)$$

with the initial condition:

$$\nu^*(r^*, 0) = 1 \quad (3.9)$$

and the boundary conditions:

$$\left. \frac{\partial \nu^*}{\partial r^*} \right|_{r^*=0} = 0 \quad (3.10)$$

$$\left. \frac{\partial \nu^*}{\partial r^*} \right|_{r^*=1} = 1 = -Bi \cdot \nu^*(1, t^*) \quad (3.11)$$

where  $Bi$  is the Biot number, defined as:

$$Bi \equiv \frac{h \cdot r_0}{k} \quad (3.12)$$

The exact solution to this dimensionless problem is a linear superposition of particular solution involving Bessel functions of the first kind:

$$\nu^*(r^*, t^*) = \sum_{n=1}^{\infty} C_n \exp(-\zeta_n^2 \cdot F_0) \cdot J_0(\zeta_n \cdot r^*) \quad (3.13)$$

where

$$C_n = \frac{2}{\zeta_n} \cdot \frac{J_1(\zeta_n)}{J_0^2(\zeta_n) + J_1^2(\zeta_n)} \quad (3.14)$$

and the discrete values of  $\zeta_n$  are the positive roots of the transcendental equation:

$$\zeta_n \cdot \frac{J_1(\zeta_n)}{J_0(\zeta_n)} = B_i \quad (3.15)$$

$J_0$  and  $J_1$  are Bessel functions of the 0<sup>th</sup> and 1<sup>st</sup> order of the first kind.

The Biot number is determined by the geometry and the nature of the wire, as well as by the convection heat transfer coefficient, which is determined by a first order modeling of the flow temperature, that will be detailed in the error modeling section in section 3.6. Theory lets us know that for values of the Biot number below 0.01, the first term of the response series needs to be retained for a 2% accuracy. Solving equations (3.14) and (3.15) gives the values of  $C_1$  and  $\zeta_1$  which can then be substituted in equation (3.13) to find the corresponding Fourier number. The corresponding time can then be deduced from this result. Accordingly, the calculations, which are detailed in Appendix B, give the following results: it takes 30 ms for the center line of the infinite-long type K thermocouple wire to be within 1% of the boundary flow temperature, at the upstream locations, and 19 ms at the downstream locations. A similar calculation has been done for the bead, which has the shape of a sphere with four times the radius of the wire. It takes 57 ms for the center of the junction bead to reach 99% of the external temperature for the upstream probes and 36 ms for the downstream located probes. This model allows the theoretical validation of the choice of 0.0005-inch thermocouple gages to satisfy the design requirement for very fast response probes.

As in all blow-down facilities, a phenomenon known as compressional heating can be observed at the early stage of the startup transient. The high pressure in the supply tank coupled with the initial vacuum in the test section has the effect of compressing the gas and, therefore, heating it, as explained in [5]. This phenomenon is very short in time and its duration is directly linked to the speed with which the valve opens. So far, only

fast response probes have been able to detect it. Hence, the capacity of a probe to record this phenomenon, which translates into a temperature spike, as shown in Figure 3.5, is an experimental criterion for a probe response qualification.

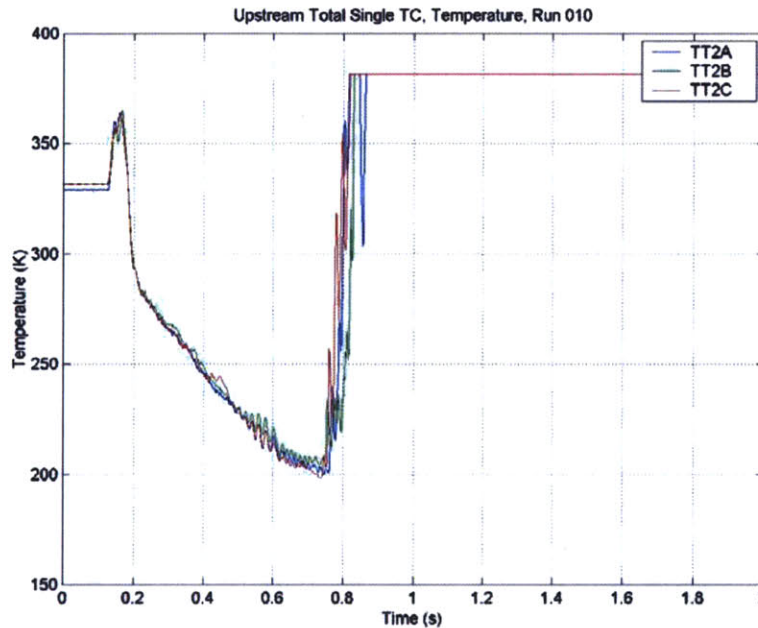


Figure 3.5 – Compressional Heating in the Blow-Down Seen by the Upstream Probes.

### 3.4.2. Upstream and Downstream Total Temperature Single Probes

As is explained in section 3.6.2, an efficient way to reduce the conduction error for a given probe is to expose significant length of wire to the flow, on either side of the junction bead. But this length should also allow the gage wire to sustain the dynamic pressure of the blow-down flow. In these circumstances, it was decided to manufacture ¼-inch single thermocouple heads.

For these heads, the gage is inserted in a ¼-inch OD casing with a 0.016-inch thick wall. These casings are each vented with two holes diametrically opposed, whose dimensions have been determined by the surrounding flow conditions and the recovery error, as explained in section 3.6.1. The gage wire is hung between two half-inch-long ceramic stems epoxied on a stainless steel spacer whose diameter matches the inner diameter of the casing. The epoxy used can endure temperatures up to 500 F. The gage

wire ends are soldered to 0.010-inch diameter thermocouple extension wires, inside the ceramic tubes. These extension parts run through a 3/16-inch stem tube, filled with epoxy to seal the probe. These single probes are mounted via Swagelock fitting on brass plugs located at the inlet and outlet stations of the compressor. These extension wires connect to thicker thermocouple extension wires to the external ice point reference chambers where they mate with temperature reference junctions maintained at 0°C. The signal is caught there and led to special conditioning instruments that will be described in section 3.4.5.

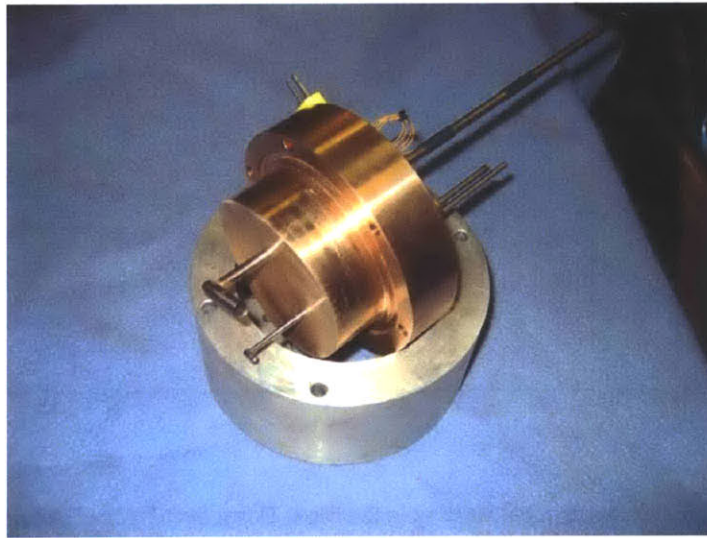


Figure 3.6 – Downstream Temperature Probe Mounted on Brass Plug.

### **3.4.3. Upstream and Downstream Total Temperature Rakes**

In order to determine the radial distribution of the temperature at the inlet and the outlet of the compressor, total temperature rakes have been designed. They consist of specially designed airfoils fitted with thermocouple heads on their leading edges. One rake is located upstream of the compressor, it supports 11 heads, spaced in such a manner that they will record temperature figures for similar annular areas. The reduction in the flow duct radius led to the design of two downstream rakes, one with 5 probes and the other with 6 probes. The arrangement of these heads is again organized in a way that all probes will cover identical annular flow areas. However, we should underscore the

exception of the tip probes on the 6-head rake, that had to be shifted towards the mid-radius of the duct, due to their casing diameter.

These airfoils have been designed so as to disturb as little as possible the flow pattern. On the one hand, this implies that the airfoils should have the smallest thickness possible. But on the other hand, the thermocouple probe performances are still subjected to conduction error, which require, to be overcome, a larger head diameter. In these circumstances, a consensual approach was found with 3/16-inch head probes. These heads have the same length and share the same layout as their single counterparts, only with a smaller inner casing diameter and a different vent hole size. Each airfoil actually consists of a main body encompassing the leading and trailing edges, with a cavity in the middle, and a cover side sliding in the airfoil span direction. It has a circular base through which it is screwed to an aluminum canister. For manufacturing reasons, each canister consists of two mating parts. The extension wires are laced together at the back of the probe heads and run down the canister to a sealed multi-pin connector where these wires are soldered to thicker thermocouple extension wires crimped to thermocouple grade sockets. The sealing of the connector is ensured by an O-ring placed between the connector part and the aft canister, and by epoxy potting, poured between the sockets. Each of these assemblies fit on machined brass plugs, which mount on the test rig. The downstream rakes have the ability to be rotated with respect to the brass plug, in order for the probes to face the flow and record the total parameters. These orientations are dependent on the speed regime the compressor is tested at. Cables have been made to be mate with the multi-pin connector and connect the thermocouple heads to their external reference junctions, as in the case of the single probe heads. From there on, the information is led to special signal conditioning devices before being recorded by the A/D devices.



Figure 3.7 – Fully assembled upstream total temperature rake.

Each probe is given an instrument name, according to a certain logic pattern. These names all start by the letters ‘TCK’, which stand for type-K thermocouples. The following letter can either be an ‘R’, for the heads mounted on rakes, or an ‘S’, for the single probes. These letters are followed by a ‘U’, for the upstream probes or a ‘D’ the downstream probes. Finally, a three-digit number is added. This information is stored in an electronic instrument database, where each probe is recorded, with the references and names of all the cables and the devices that are active in their functioning. This is not only important for archiving purposes, but also and above all, for calibration purposes, as will be explained in section 3.5.

#### **3.4.4. Mechanical Integrity within the Flow Conditions**

After having determined a design capable of satisfying the requirements for the blow-down testing thermal conditions, it was necessary to set up a test that would validate this design in terms of structural integrity of the probes when they are submitted to the dynamic pressure of the flow. In this purpose, a free-jet stand was used. This facility consists of a plenum tube with a circular opening at one end and a connection to a pressurized air system at the other. The gas expands isentropically through the open exit of the plenum. The total pressure of the gas is hence conserved. Inside the plenum, the speed of the gas is close to zero. It is hence possible to monitor the dynamic pressure

coming out of the plenum tube by setting its inner pressure to a certain value through a feeding valve.

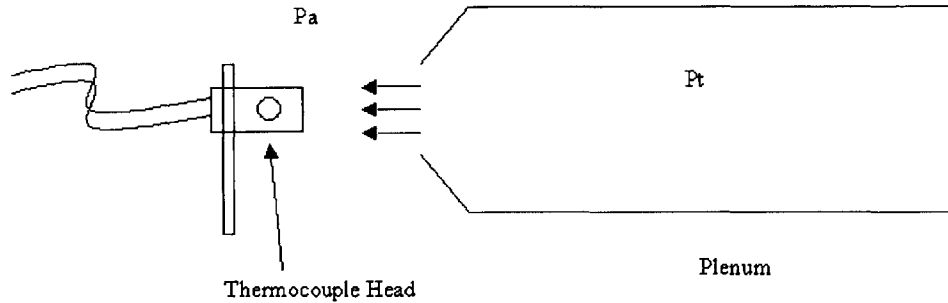


Figure 3.8 – Schematic of Free Jet Resistance Test.

To gather the best efficiency out of this validation test, the simulation aimed at reproducing the strongest dynamic pressure the probes were likely to encounter in the compressor. These conditions occur for the design speed test, at the downstream locations, at the starting of the transient blow-down. The dynamic pressure reaches almost 6 psi in such conditions. The pressure inside the plenum had to be brought to 20.7 psi to reproduce these conditions, and to achieve a safety factor of one. The probes were then exposed to this dynamic pressure in different ways. The first way tried to systematically search for the pressure leading to the gage break. A given probe would be submitted to any total pressure values between the ambient pressure and the limit value of 22 psi, in steps of 0.5 psi. Several tests showed that the downstream probes were unable to sustain the level of dynamic pressure required. Many broke just around 21 psi, which was perfectly suitable for the upstream probes, which would only be submitted to total pressures of 18 psi at most. Digital camera pictures showed that the breaking points were systematically located at the nearest proximity of the bead junction. The manufacturing process requires the two thermoelectric metal wires to be at a 60° angle from one another, at the location where the bead is machined. Our probe manufacturing process required stretching this gage, creating elbows in the immediate vicinity of the bead. Kinking the gage wire in this location turned out to render it more fragile.

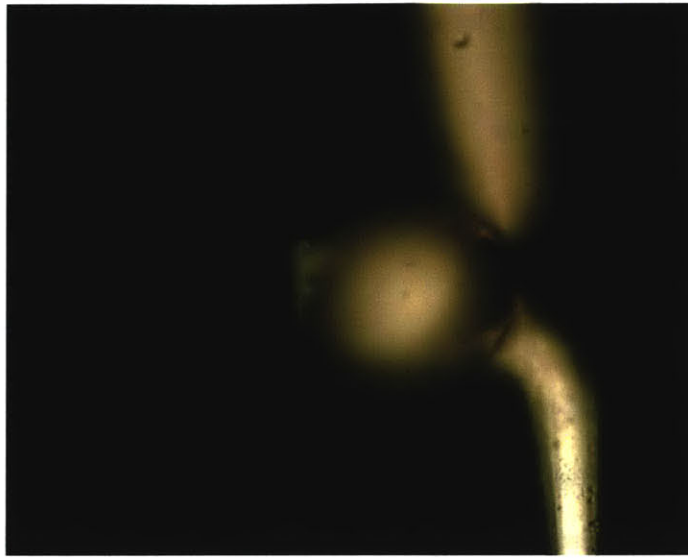


Figure 3.9 – Picture of 0.0005-inch Thermocouple Gage.

Consequently, several solutions were examined. The first one consisted in trying to manufacture the heads without stretching the gage wire between the two ceramic stems, so as to release the level of stress in this wire and avoid the kinks creating fragile areas on either side of the bead junction. Several gage wire shapes and assembling processes were made, but they all turned out to be either too hard to realize, or totally inefficient to improve the probe design in terms of structural integrity to the tests. Releasing the stress led to the gage wires to be more confronted to the drawbacks of the turbulent flow inside the head casing.

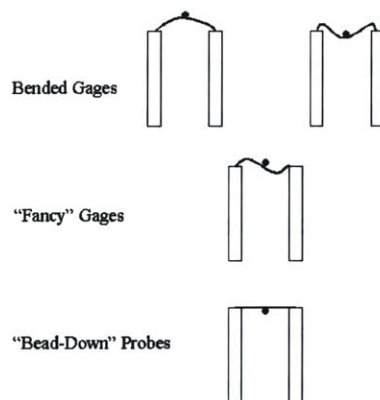


Figure 3.10 – Gage Wire Shapes Tested in the Free Jet Stand

Another option consisted of changing the vent hole sizes on the head casings. As will be explained in section 3.6.1., the vent hole size sets the recovery error of the thermocouple probe, by regulating the flow of air inside the casing. Decreasing the vent hole size would result in a smaller flow speed and hence a smaller dynamic pressure on the gage wire. But reducing the Mach number inside the head had other consequences as well. Although it allows reduced recovery error, it increases the response time of the gage, by reducing the convection heat transfer coefficient around the wire. Another option was to reduce the casing diameter, to reduce the length of wire exposed to the flow. This reduction would entail an increase in conduction error of the probe. In order to achieve the best decision, a comparative study was conducted to assess the modifications any given load reduction on the wire would have on the recovery and the conduction error as well as the response time of the probe, which are all affected by the different options detailed above. These modifications are summarized in Figure 3.11, Figure 3.12 and Figure 3.13.

This study showed that the best consensus, entailing the lesser losses in design requirements as well as manufacturing procedures, would consist in reducing the vent hole size of the downstream probes to achieve a 30% reduction in load on the gage wire. This solution imposed an increase of 3 ms in response time, which corresponds to a 10% increase, but granted a 35% decrease in recovery error. The exponential changes in conduction error with the reduction in load showed the higher impact on the quality of the measurements a reduction in casing diameter would have had.

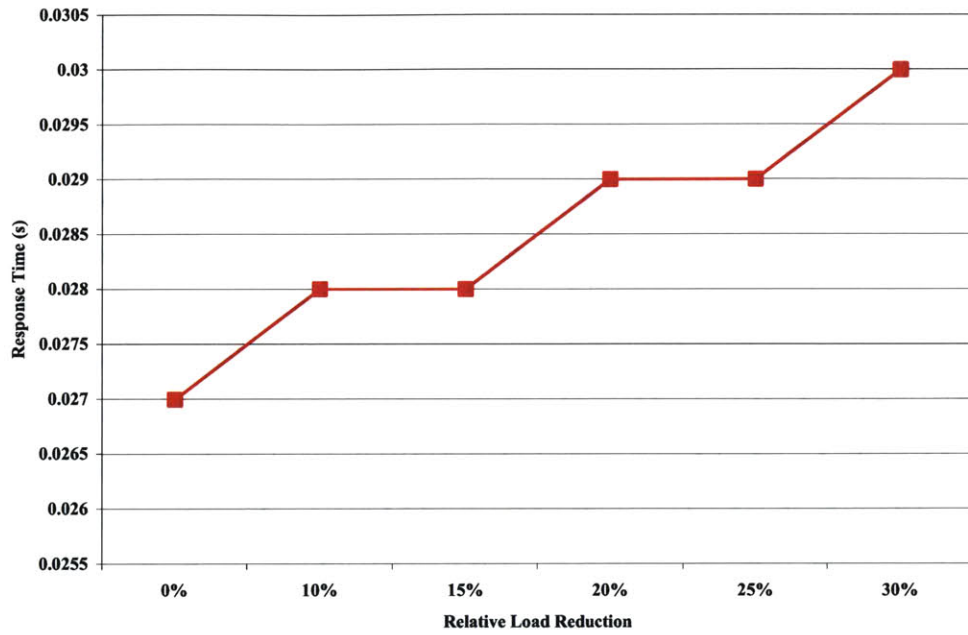


Figure 3.11 – Wire response-time in (s) versus the Percentage of Load Reduction for 1/4” heads by Decreasing the Vent Hole Size.

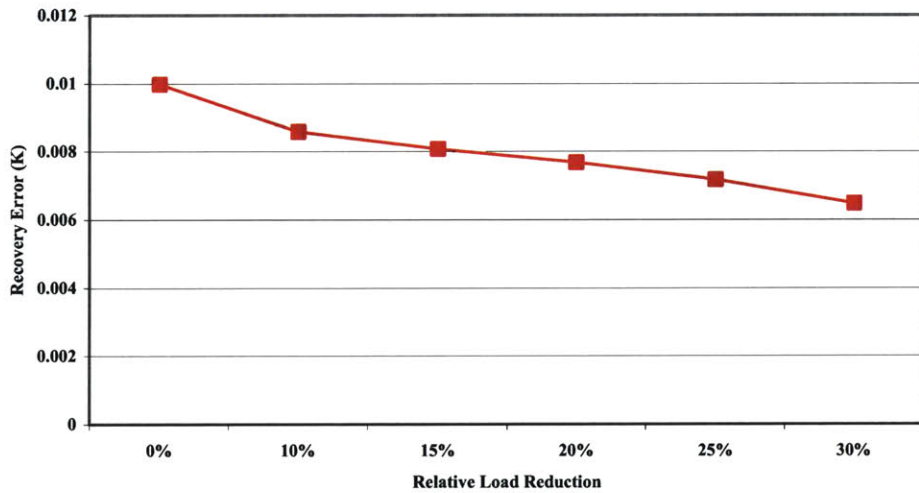


Figure 3.12 – Evolution of the Recovery Error versus the Percentage of Load Reduction for 1/4” heads, by Decreasing the Vent Hole Size.

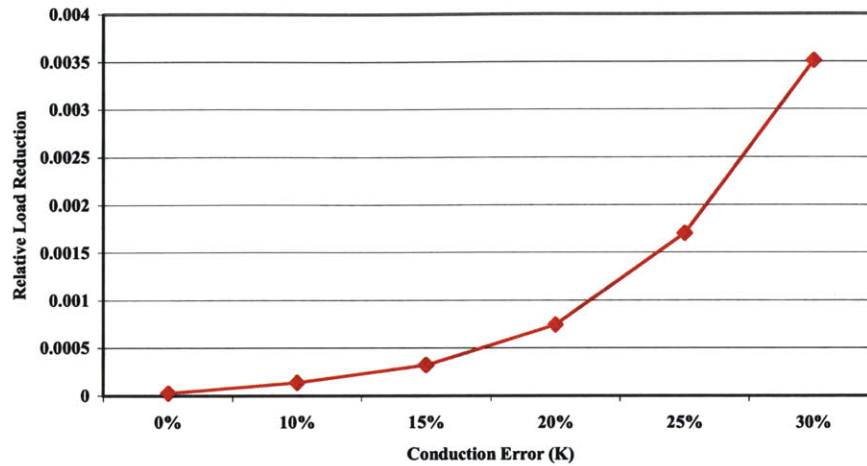


Figure 3.13 – Evolution in Conduction Error versus the Percentage of Load reduction by Decreasing the Inlet Area of a 1/4” head.

Following the same protocol, the new probes were tested to find the pressure causing the gage wire to break. They proved to be much more resistant and broke under a total pressure of 26 psi, which corresponds to a safety factor of 2 in terms of dynamic pressure.

To finally validate the assembly process, it was decided to submit all the different probes to a test simulating the pressure pulse they would see in the test rig. This protocol consisted in reproducing the pressure pulse consecutive to the firing of the fast acting valve. Each head would be placed in the flow path but would remain protected from it by a bar of angled iron. The pressure in the plenum would be brought to 22 psi, and the angle iron would be removed quickly. The air flow in the plenum would be shut right after.

### 3.4.5. Signal Conditioning

Output signals from the total temperature probes are filtered and amplified by 2B31L analog device signal conditioners. After amplification, the signals are fed into multiplexer A/D systems, which are described in section 2.4.2. This type of signal conditioner module has small offset drift with temperature and time ( $0.6 \mu\text{V}/^\circ\text{C}$  and  $3 \mu\text{V}/\text{month}$  from

specifications) and low gain non-linearity (0.025% max from specifications). Experiments indicate offset variation of less than 0.0006 mV (corresponding to 0.001 K at gain 1000) during a typical day. The conditioner module provides an adjustable-gain amplifier, a three-pole low pass filter and also an adjustable transducer excitation. All thermocouple signals are low-pass filtered at 500 Hz.

### ***3.5.Static Calibration of Total Temperature Probes***

As has been explained in section 3.3, using signal enhancing and conditioning devices on thermocouple probes require the probes to be calibrated, as each device introduces some error and drift from the standard thermocouple tables. In this chapter, the calibration equipment used is described, as well as the calibration procedures of the thermocouple probes.

#### **3.5.1. Calibration Equipment**

The calibration of the thermocouple probes aims at determining and creating a file associating each voltage output of the instrumentation to the corresponding temperature of the probe. For that purpose, the probes are placed in a medium that is thermally conductive and electrically non-conductive, so as to render the calibration independent of the medium the probe is in. The thermocouple probes of the counter-rotating aspirated compressors are submitted to temperatures that range from  $-60^{\circ}\text{C}$  to  $170^{\circ}\text{C}$ . This range cannot be covered by a single calibration fluid. It was hence necessary to acquire two different calibration baths. For the lower part of the temperature range, a calibration bath of the type 7381 from Hart Scientific was used. This device offers an 18-inch deep cavity and is fitted with a cooling system that allows it to reach temperatures ranging from  $-80^{\circ}\text{C}$  to  $110^{\circ}\text{C}$  [8]. The fluid used in that bath is Hart Scientific HFE 7500, which can be used between  $-75^{\circ}\text{C}$  and  $100^{\circ}\text{C}$ . This fluid was chosen for its reasonable price and its probe cleaning simplicity. The upper temperature calibration was handled by a Hart Scientific 6330 calibration bath. This device covers temperatures from  $35^{\circ}\text{C}$  to  $300^{\circ}\text{C}$ . The cavity is 9.25 inches deep. The fluid used was Silicon oil 200.20 that can cover temperatures from  $10^{\circ}\text{C}$  to  $230^{\circ}\text{C}$ . Each bath is fitted with an automatic stirring system

that guarantee a flow temperature uniformity of less than 0.02°C at 200°C for the 6330 model and 0.007°C at 0°C for the 7381 model. Each bath can be monitored either manually or automatically via an RS-232 connection.

To optimize the quality of the calibration files, the calibration bath's temperature is recorded in two ways. The first way is a built-in system that is used to monitor the bath. The second one relies on a NIST-traceable Rosemount Standard Platinum Resistance Thermometer model 162N. The specifications are given in Table 3.1. This device is used to establish the calibration file. The resistance of the Rosemount thermometer is measured by a Fluke 8520A digital multimeter. This multimeter can be operated remotely via an integral IEEE-488 interface, allowing triggering from the data acquisition computer.

<b>Temperature range</b>	-200°C to 400°C
<b>Stability</b>	0.10°C/year
<b>Self-Heating</b>	28 mW/°C
<b>Time Constant</b>	1.0 sec
<b>Max. Calibration Uncertainty (below 200°C)</b>	0.025°C

Table 3.1 – Specifications for the Rosemount Standard Platinum Resistance thermometer model 162N.

A Labview data acquisition program, named TCCalMain, is run on a DELL x86 computer. This program reads and records the voltage output of each thermocouple amplifier through the A/D and the resistance of the Rosemount thermometer through the Fluke digital multimeter. The program displays the temperature reading of the calibration bath. A setting file where the starting temperature set-point, the number of set-points, the temperature increment, the sampling rate, the sampling count as well as the bath conditions to start recording a set-point, must be specified to operate the baths through the Labview program. The end product is a text file gathering the calibration conditions, the probe name, as well as the set-point recordings.

### **3.5.2. Calibration of Thermocouples**

To perform a calibration, the thermocouple probes are mounted on a metallic plate. In the case of the single probes, the plate is fitted with 6 Swagelock fittings. The length of stem is set to ensure the heads remain in the calibration fluid over the entire

calibration process and despite the fluid's changes in volume. An extra hole was drilled to accommodate the Rosemount thermometer as close to the heads as possible. The plate is used as a lid for the bath, so as to reduce convection from its surface and to protect the fluid from dust or other particles. As for the rakes, the metallic plate is fitted with a 3.2" inch hole to support a Teflon jig onto which the rake mounts. The rakes' canisters are designed with a flange to ease the assembly of the rake onto the brass piece. This flange is a convenient way of holding the rake in the bath. But the forward canisters are not long enough to guarantee that the probes are immersed in the fluid at all times. In the meantime, the flange was too large to be inserted in the bath. It was hence necessary to unscrew the two parts of the rakes' canisters and to design a jig that would allow to hold the front part in the fluid while keeping the aft part of the canister outside the cavity.

Once mounted, the probes are then hooked to their assigned extensions wires to their cold junction thermometers. The signal is then carried to the A/D device through the amplifier cards. For the accuracy and quality of the calibration, it is mandatory to hold the external reference junction cells to the stable temperature of 0°C. This requires the cells to be switched on at least 24 hours prior to the calibration. It is also mandatory to name, identify and record thoroughly each wire and device linking each probe to the data acquisition system, as the calibration and the signal is strongly dependent on the physical properties of these accessories. To ensure a proper use of the probes, the thermocouple have to be linked to the same wires, cold cells and amplifying cards as they were during their calibration to validate the information they provide. This information is stored in a LabView database named "InstrumentDataBase".

The calibration setting file is used to set up each calibration. For this experiment, each probe is calibrated from -60°C to 60°C on the cold bath and from 50°C to 170°C on the hot bath, by increments of 10°C. This gives two overlapping points for each probe, which allows a partial check for the validity of a calibration measurement. The bath temperature setting is monitored from the computer. The computer records the bath temperature every five seconds and computes the associated average value over the last 3 minutes, along with the corresponding standard deviation. These parameters play a key role in determining the right moment for the computer to make a calibration

measurement. It appears mandatory to guarantee the stability and the homogeneity of the fluid temperature to make an accurate and sensible recording. The average of the last 3-minute bath temperature recordings must be within 1 K from the set-point value while the standard deviation must be less than 0.1 K. When these criteria are met, the computer records 500 samples of data from the Rosemount thermometer and from the A/D device at the rate of 50 Hz. The corresponding averages are stored in a separate text file for each probe.

As mentioned earlier, the two calibration baths are operated with different fluids. To transfer the probes from one bath to the other, the thermocouples are cleaned with ethanol, which very efficiently dissolves the fluids and evaporates. This procedure prevents any mixing of the two fluids and contributes to the quality of the calibrations.

The calibrations are used to determine probe drifts with time. Several calibrations are hence necessary to determine this aspect and to obtain the proper calibration files. A Matlab program was written to check the validity and the quality of the calibration of the thermocouple probes. For each thermocouple probe, this program treats their calibration file in a chronological order. It first performs a 9<sup>th</sup>-order polynomial regression on the data of all but the latest calibration file. It then computes and plots the difference in temperature between the data points of the last calibration file and the temperature the polynomial fit gives for the same voltage output, for each of the previous calibration files. Another comparison is done between those calibration curves and a 9<sup>th</sup>-order polynomial fit for the last file. An average error is also plotted. The choice for a 9<sup>th</sup>-order polynomial regression is based on the fact that the ideal law linking the voltage output of a type-K thermocouple and its corresponding temperature is a 9<sup>th</sup>-order polynomial. This choice was hence made in a conservative perspective.

This program has been able to show that the thermocouple probes age at the higher range of temperatures. Calibration after calibration, the difference plotted by the Matlab program was brought down to a level less than 0.1 K. This latter value was chosen to determine whether the thermocouple probes were still subjected to drifts or whether they could be used with the corresponding calibration file. Closer attention was also paid to the overlapping temperature range between the two baths. Here again, a

difference of less than 0.1 K was set as an acceptance criterion. Once a calibration file is judged acceptable, it is stored as a Matlab file that is automatically used in the data processing.

To further check the drifts in calibration, the single probes were recalibrated after the first three runs. Again, difference of less than 0.1 K was recorded between this calibration and the last one used for the first tests, which showed the absence of drift for these probes.

### ***3.6. Uncertainty Estimation of Total Temperature Measurement***

The property of thermocouple material slightly varies due to imprecision in fabrication. This error can be reduced through proper calibration of each individual thermocouple. The related uncertainty is then totally dependent on the calibration method and the quality of the calibration equipment. But there are three other factors or sources of uncertainty in the temperature measurement of fluid flow. These sources are the recovery error, the conduction error and the radiation error. In this following chapter, we will discuss those three sources and quantitatively evaluate them.

#### **3.6.1. Recovery Error and Response Time**

Total temperature can be measured only when the fluid flow is brought to rest isentropically. Unfortunately, temperature probes cannot satisfy this requirement. How close the measured temperature is to the true total temperature can be evaluated by the recovery factor  $r$ .

$$r \equiv \frac{T_{t,ind} - T_s}{T_t - T_s} \quad (3.16)$$

where  $T_{t,ind}$  is the measured total temperature,  $T_t$  is the true total temperature, and  $T_s$  is the static temperature. If for a certain probe,  $r$  is equal to 1, then this probe stagnates the fluid flow isentropically without any loss.

A reasonable assumption for the evaluation of recovery loss is that all the measurement error is caused by recovery effect. In [5], the recovery error is estimated as:

$$E_{rec} = \frac{(1-r) \cdot \frac{\gamma-1}{2} \cdot M^2}{1 + \frac{\gamma-1}{2} M^2} T_t \quad (3.17)$$

where  $M$  is the Mach number, and  $T_t$  can be calculated with the known parameters of the compressor.

[6] shows that the recovery factor is highly dependent on the geometry of the probe as well as the operating conditions and the material constituting the thermocouple gage. Consequently, it can only be determined experimentally and no a priori law encompassing those parameters has been established yet. Hence, the best estimation available is still the ideal concept linked to the Prandtl number of the fluid flow. In these circumstances, the recovery factor is set by the flow and is an external factor in the computation of the recovery error. The Mach number is the only parameter that can be set by the design of the probes to determine the recovery error. This Mach number is determined by the ratio of the casing inlet surface area to the vent hole surface area. For a subsonic flow, a reduction in Mach number entails a reduction in the recovery error, all other parameters being equal. The goal is to reduce the recovery error as much as possible, but a reduction in the Mach number around the thermocouple junction implies an increase in the time response of the probe, as has been explained earlier. The recovery error helps determine a Mach number that leads to the computation of the probe time response. For the upstream probes, the best compromise was found for a recovery error of 0.025 K, which lead to a time response of 30 ms. The associated vent hole have a diameter of 0.096 inches for the single probes and 0.076 inches for the rake probes. As

for the downstream probes, the recovery error was contained even more, at 0.0065 K, with a time response of 19 ms, and vent holes of 0.074 inches for the single probes and 0.060 inches on the rake probes.

Probes	Inlet diameter (in)	Vent hole diameter (in)	Mach number	Recovery Error (K)	Time response (s)
3/16 upstream	0.174	0.076	0.059	0.0250	0.030
1/4 upstream	0.219	0.096	0.059	0.0250	0.030
3/16 downstream	0.174	0.060	0.030	0.0065	0.019
1/4 downstream	0.219	0.074	0.030	0.0065	0.019

Table 3.2 – Summary of Probes Geometries, Inner Mach Numbers, Recovery Errors and Time Responses.

### 3.6.2. Conduction Error

As mentioned earlier, the conduction loss was the biggest error source that made the previously designed total temperature probes unsuitable to the blow-down type tests. In this design, the 0.0005-inch type-K thermocouple is stretched across the inner diameter of the stainless steel shield. The wire is supported by two ceramic tubes. While the flow comes into the probes, heat is convected from the test gas to the wires. It is also conducted from the wires to the supporting ceramic tubes. Previously, we have shown that the time response at upstream test condition amounts to 30 ms and 19 ms at downstream conditions. With such fast time response, we can assume a one-dimensional steady state conduction-convection model to calculate the conduction error.

The heat equation for one-dimensional steady state conduction-convection of a fin with uniform cross-sectional area can be written as:

$$\frac{d^2T}{dx^2} - \frac{hP}{kA_c}(T - T_\infty) = 0 \quad (3.18)$$

where  $T$  is the temperature of the fin,  $x$  is the coordinate along the fin,  $h$  is the convection heat transfer coefficient,  $k$  is the thermal conductivity of the thermocouple,  $P$  is the perimeter of the thermocouple,  $A_c$  is the constant cross-sectional area, and  $T_\infty$  is the gas temperature.

If we define the difference between the thermocouple temperature and the gas temperature as

$$\theta(x) \equiv T(x) - T_\infty \quad (3.19)$$

then, we can rewrite equation (3.18) as

$$\frac{d^2\theta}{dx^2} - m^2\theta = 0 \quad (3.20)$$

where

$$m^2 \equiv \frac{hP}{kA_c} \quad (3.21)$$

Equation (3.20) is a linear, homogeneous, second-order differential equation with constant coefficients. Its general solution is of the form

$$\theta(x) = C_1 e^{mx} + C_2 e^{-mx} \quad (3.22)$$

To evaluate the constants  $C_1$  and  $C_2$ , it is necessary to specify boundary conditions. In our case, the two boundary conditions are the same. Figure 3.14 shows the schematic of the one-dimensional convection-conduction model of the thermocouple. The temperature difference between the gas and wall at the two ends of the thermocouple is the same as

$$\theta(0) = \theta(L) = T_{wall} - T_{\infty} \equiv \theta_{wall} \quad (3.23)$$

The solution to equation (3.20) is

$$\theta(x) = \theta_{wall} \frac{\sinh(mx) + \sinh(m(L-x))}{\sinh(mL)} \quad (3.24)$$

The flow parameters different and the gas properties change through the compressor. This results in different conduction losses. Figure 3.15 shows the difference between the gas temperature and the thermocouple wire temperature divided by the difference between the wall temperature and the gas temperature, which is the relative measurement error, for the upstream  $\frac{1}{4}$ -inch temperature probes. Qualitatively, the errors are small. For the upstream conditions, the rake probes show a conduction error of 0.073 K, while the single probes one of 0.005 K. For the downstream conditions, the rake probes show a conduction error of 0.014 K and the singles 0.0005 K. Such low values are due to the small size of the thermocouple wires and the great length exposed to the gas. The fact that the conduction loss does not penetrate from the inner wall of the probe shield to the middle of the thermocouple wire resulted from these two positive factors.

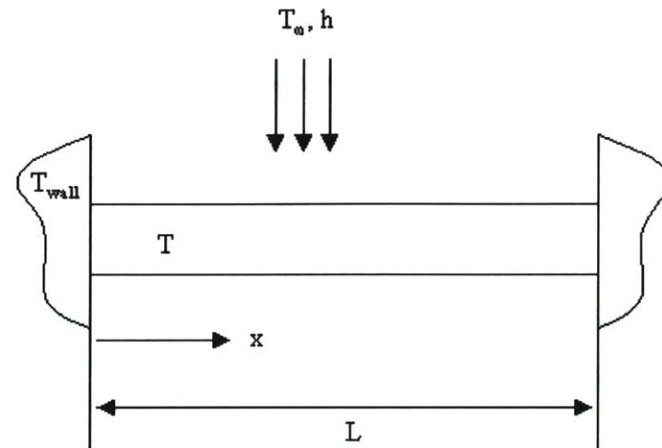


Figure 3.14 – Schematic of One-Dimensional Conduction-Convection Model for Thermocouple Wire.

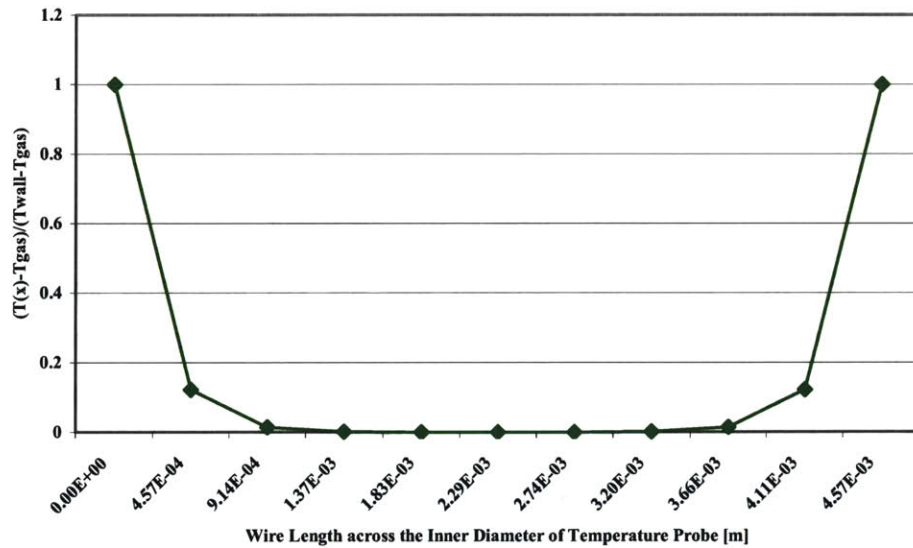


Figure 3.15 – Conduction Error Percentage, Predicted by a Steady State One-Dimensional Conduction-Convection Model.

### 3.6.3. Radiation Error

Radiation of the thermocouple wires is also an important error source in temperature measurement. As in [5], the radiation error is evaluated at steady state

conditions, and the assumption is that all the heat convected from the gas to the thermocouple is radiated to the surrounding body, i.e. the probe stainless steel shield. The error can be expressed as

$$E_{rad} = \frac{\sigma \varepsilon (T_{t,j}^4 - T_{surr}^4)}{h} \quad (3.25)$$

where  $\sigma$  is the Stefan-Boltzman constant and  $\varepsilon$  is the emissivity of the junction. A value of 0.4 is used for chromel-alumel material [9].  $h$  is the convection heat transfer coefficient.  $T_{t,j}$  is the temperature of the thermocouple junction.  $T_{surr}$  is the temperature of the surrounding shield. Since the upstream and downstream total temperature probes are sitting in the test section of the tunnel, their temperature is room temperature prior to the test. The probes are essentially a part of the tunnel, thus they are a comparatively large heat sink. A heat transfer calculation performed on the blades show that the probe shield temperature will not change significantly during the test time. Therefore, the radiation shielding for the thermocouple sensors in short-duration experiment has little effectiveness. During a test upstream and downstream temperature sensors see different gas temperatures, and  $h$  is also different. The error due to radiation loss for upstream temperature probes is 0.112 K and that for the downstream probes is 0.299 K. The latter value is obtained for the highest temperature the probe sees. Detailed calculation is given in Appendix B.

#### 3.6.4. Overall Uncertainty of Total Temperature Measurement

The four major sources of uncertainty have been discussed in the previous paragraphs. The following table summarizes the quantitative estimates of those errors. These errors stem from independent sources. The total absolute error is hence computed as the square root of the sum of the squares of each source. The percent uncertainty is calculated with upstream and downstream flow conditions.

Sensor Name	Error (K)				
	Recovery	Conduction	Radiation	Calibration	Total
TCKSU001	0.025	0.005	0.112	0.048	0.124
TCKSU002	0.025	0.005	0.112	0.058	0.129
TCKSU007	0.025	0.005	0.112	0.055	0.127
TCKRU001	0.025	0.073	0.112	0.041	0.142
TCKRU002	0.025	0.073	0.112	0.038	0.141
TCKRU003	0.025	0.073	0.112	0.040	0.142
TCKRU004	0.025	0.073	0.112	0.039	0.141
TCKRU005	0.025	0.073	0.112	0.042	0.142
TCKRU006	0.025	0.073	0.112	0.040	0.142
TCKRU007	0.025	0.073	0.112	0.038	0.141
TCKRU008	0.025	0.073	0.112	0.039	0.141
TCKRU009	0.025	0.073	0.112	0.039	0.141
TCKRU010	0.025	0.073	0.112	0.043	0.143
TCKRU011	0.025	0.073	0.112	0.042	0.142
TCKSD001	0.0065	0.0005	0.299	0.071	0.307
TCKSD002	0.0065	0.0005	0.299	0.036	0.301
TCKSD003	0.0065	0.0005	0.299	0.065	0.306
TCKRD001	0.0065	0.014	0.299	0.033	0.301
TCKRD002	0.0065	0.014	0.299	0.028	0.301
TCKRD003	0.0065	0.014	0.299	0.034	0.301
TCKRD004	0.0065	0.014	0.299	0.034	0.301
TCKRD005	0.0065	0.014	0.299	0.037	0.302
TCKRD006	0.0065	0.014	0.299	0.060	0.305
TCKRD007	0.0065	0.014	0.299	0.326	0.443
TCKRD008	0.0065	0.014	0.299	0.054	0.304
TCKRD009	0.0065	0.014	0.299	0.047	0.303
TCKRD010	0.0065	0.014	0.299	0.062	0.306
TCKRD011	0.0065	0.014	0.299	0.097	0.315

Table 3.3 – Detailed Summary of Thermocouple Probes’ Errors.

## **4. Total Pressure Measurement**

### ***4.1. Introduction***

The measurement of the pressures at the inlet and the outlet of the compressor is required to the aerodynamic performance study. As mentioned in section 2.4.1, the blow-down compressor employs one 8-head impact total pressure probe rake upstream of the IGV and two 5-head impact total pressure probe rakes. In addition, upstream of the compressor are located three sets of pressure sensors encompassing each a Kiel head total pressure probe, a static pressure point and a Pitot probe. One comparable set is mounted downstream of the compressor, where the static sensor window is fitted with a high-speed pressure sensor. Along with the total temperature measurement, these probes allow the mass-flow and the Mach number at different locations in the flow to be estimated. Several other pressure sensors are mounted on the rig, namely a high-speed static tap between the two rotors, and a 3-way wedge probe in the bleed flow passage. Both the supply and the dump tanks have been fitted with a redundant static pressure measurement system.

In this chapter, the requirements for the total pressure measurement are outlined. The design of the total pressure probe rakes is described. The online calibration

procedure is detailed and lastly, an uncertainty estimation of the total pressure measurement is presented.

#### ***4.2. Requirements for Total Pressure Probe in a Blow-Down Facility***

The purpose of the total pressure probe is to record the stagnation pressure in the flow field. In this perspective, the probe should be designed to stop the flow isentropically and add dynamic pressure to static pressure. The probes must hence be adaptable to the flow direction so as to record the total parameters. The single total pressure measurement points are achieved using both Kiel-head and Pitot probes, which are fitted on brass plugs via Swagelock fittings, gripping their stems. This allows an easy rotation of the probes towards the flow direction. As for the radial total pressure distribution, it is measured through special airfoil-shaped rakes accommodating impact heads on their leading edges. This choice was made so as to minimize the blockage effect caused by the introduction of rakes in the flow. Impact heads present the advantage of being relatively small in comparison to other total pressure measurement devices. But the direct consequence of the small inlet section area of these impact heads is their relatively strong sensitivity to misalignment. Consequently, the rakes they are mounted on have to be easily adjustable.

The main type of pressure transducer used in the counter rotating aspirated compressor is a piezoresistive strain gage. A piezoresistive transducer is essentially a variable resistor that changes its resistance under different mechanical strains. This type of transducer is very sensitive to pressure change and has good response frequency, which is a prevailing critical factor in a blow-down facility. But in the case of ultraminiature gauges, this technology shows some instability caused by non-linearity and hysteresis effects. To overcome these particularities, these Kulite sensors are calibrated against two high precision Heise transducers prior to filling the supply tank, once the supply tank is filled and immediately after a test. A Heise DXD 150 psia is located in the supply tank and a HEISE model DXD 15 psia is recording the pressure in the dump tank. These two transducers are also piezoresistive strain gauges.

For further accuracy, two absolute strain gage transducers were mounted on the supply and the dumps tanks. The model implemented upstream from the compressor is a Sensotec SuperTJE – 150 psia and the one on the rear is a Sensotec TJE – 50 psia.

### ***4.3. Total Pressure Design***

#### **4.3.1. Isolated Pressure Measurement probes**

The isolated pressure probes encompass the Kiel heads, the Pitot probes as well as the flush mount static pressure tubes. The first two types are commercially available devices. Their geometry has been certified and calibrated by their manufacturer. More information can be found in [13] and [14].

The Kiel head total pressure probes are of type KCD and KCC. The inner side of the sensing head is shaped as a Venturi. Kiel heads show a noticeable insensitivity to flow angle, which ranges to  $\pm 54^\circ$  in yaw and  $\pm 49^\circ$  in pitch. Pitot probes show a lot more sensitivity in that respect. Yaw and pitch affect the reading the same way and result in relative static and total pressure measurement errors of 3% and 1% respectively for yaw/pitch angle of  $\pm 10^\circ$ .

#### **4.3.2. Total Pressure Rakes**

The stationary upstream low-frequency total pressure rake has eight impact heads. The eight heads are radially arranged on the leading edge of the supporting airfoil. Each head has sharp leading edge, which is effective in reducing the sensitivity to misalignment. A  $15^\circ$  bevel angle was chosen for these impact heads. This angle provides  $\pm 27.5\%$  insensitivity. [10]. They are connected to fine aluminum tubes and Tygon tubes which transfer the pressure outside of the rig and onto which pressure transducers are mounted. An efficient use of epoxy guarantees the integrity and the sealing of the rake. This device does not have the ability to rotate, as the flow is supposed to enter the compressor deprived of any swirl. The pressure sensors used are Kulite XCQ-062-15, which can sustain a pressure of 15 psig. Back reference pressure is provided to the transducers via Tygon tubing which is connected to an external vacuum pump. A Lemo

connector cable is mounted on the back of the transducer and carries the information to an amplifier box.

The two downstream rakes are identical to the upstream one, except that they only carry five impact heads each. The Kulite transducers are capable of sustaining higher pressures, namely 50 psig. These rakes have been designed to be rotated around the span direction, so as to face the swirl of the flow coming out of the compressor.

The naming convention used for these probes is summarized in the Table 4.1.

Sensor Name	Location
PT2ZRxx	Upstream of NGV
PT5CRxx	Downstream of rotor 2
PT5ZRxx	Downstream of rotor 2

Table 4.1 – Pressure Sensor Name Nomenclature.



Figure 4.1 – Fully-Assembled Upstream Total Pressure Rake.

### 4.3.3. Signal Conditioning

Output signals from the total pressure probes are filtered and amplified by AD521IC analog device signal conditioners. After amplification, the signals are also fed into multiplexer A/D systems, described in section 2.4.2. The conditioner module provides an adjustable-gain amplifier, a three-pole low pass filter and also an adjustable transducer excitation. All pressure transducer signals are low-pass filtered at 500 Hz.

#### ***4.4. Probe Calibration***

For most pressure transducers, the relation between pressure and voltage is linear. Therefore, we need to know the sensitivity and zero offset of each transducer. In order to minimize the offset drift of the pressure transducers due to time, run-time calibration method is applied in a blow-down test. Pre-fill calibration is done when the tunnel is in vacuum, post-fill calibration is done once the supply tank has been filled and the post-test calibration is done after the tunnel pressure has reached steady state conditions. The two differential pressure states are recorded by alternately switching the transducer reference pressure to atmosphere and vacuum. The three calibrations are compared to see how much the transducers drift.

To determine the scale and the zero of each transducer, a Matlab program called AutoCal was written. It first starts by determining the scales by associating the voltages recorded by each transducer to two differential pressures. The first one corresponds to the case when the back pressure system is in vacuum while the second one corresponds to the case when it is sitting at atmosphere. The associated pressures are then the difference between the pressure read by the Heise transducer sitting in the same condition as the transducer in the process of calibration and the back pressure.

Determining the voltage that corresponds to a pressure of zero is done based on data recorded right before the blow-down, as Kulite transducers show a tendency to drift. This zero is computed as the difference between the voltage read by each transducer and the pressure read by the Sensotec probe, in the corresponding condition, divided by the scale established earlier. We should point out that the Sensotec probes are calibrated against the Heise transducers during the pre-fill and the post-test calibrations.

#### ***4.5. Uncertainty Estimation of Pressure Measurement***

The total uncertainty in both upstream and downstream pressure measurements will be considered to consist of three parts: the probe error, the signal noise and the transducer error. Since these errors are not correlated, the root mean square will be taken.

The probe error results from the aerodynamic interference of the probe. This error is reduced by using an airfoil probe body shape. An error is introduced when the probe is misaligned with the flow direction. The impact head with 15° bevel angle provides ±27.5° insensitivity to the flow angle. Within this ±27.5°, the measurement error is less than 1% of the dynamic head. It is of interest to determine the probe error caused by misalignment upstream and downstream of the compressor stage. Following the approach taken in [11] gives:

$$\frac{1}{2} \rho V^2 = \frac{1}{2} \rho M^2 a^2 = \frac{\gamma}{2} M^2 p \quad (4.1)$$

The non-dimensional form of the dynamic pressure becomes:

$$\frac{\frac{1}{2} \rho V^2}{P_t} = \frac{\gamma M^2}{2(1 + \frac{\gamma-1}{2} M^2)^{\gamma/\gamma-1}} \quad (4.2)$$

The maximum non-dimensional error, then, should be 1% of the value given by equation (4.2). Using the recorded upstream and downstream time-averaged Mach numbers and average specific heat ratio, we have been able to compute the total probe error for each run. The results are summarized in Table 4.2 and Table 4.3.

For the static measurement points on the Pitot heads, the non-dimensional form of the dynamic pressure over the static pressure becomes:

$$\frac{\frac{1}{2} \rho V^2}{P_s} = \frac{\gamma M^2}{2} \quad (4.3)$$

The maximum non-dimensional error, then, should be 1% of the value given by equation (4.3). Using again the results of each test run, the static Pitot probe errors have been computed. They are summarized in Table 4.4.

The transducer error mainly comes from non-linear behavior of the transducer and the drift of zero-offset. Often times, these two error sources work together, and it is not easy to separate them. To measure the error on each probe, the following process is followed. The tunnel is first brought to vacuum. A calibration is performed. Air is then injected in the tunnel to a pressure of 2.65 psi. Once this pressure has settled, data are

sampled from all pressure measurement probes over 30 sec. More air is let inside the tunnel and these steps are repeated 6 times at the intermediate pressures of 6.05, 8.85, 12 psi and atmosphere pressure of 14.85 psi. After the final set of data is recorded, another calibration is performed. For each step, the probes measurements are computed using the 2 calibrations. The results are then compared to the Heise readings of the pressure in the tunnel. Hence, for each pressure level, an average relative error is calculated, along with a standard deviation. The final transducer error is taken as the mean value of the individual relative errors. As for the mean standard deviation, knowing the data have been recorded on a time scale that is much larger than the inverse of the sampling rate, it represents the noise associated to each pressure instrument signal. The results are gathered in Table 4.5 and Table 4.6. They correspond to calculation made with the last calibration file, which was performed under conditions closer to the blow-down test conditions. We were able to detect a difference of 0.05% with the results obtained with the first calibration.

Another important source of error is linked to the effects of temperature on the transducer sensitivity. This phenomenon was thoroughly studied in [5]. Transducer sensitivities can vary from 1% to 2.5% over the compensated temperature range, which corresponds to 25°C to 80°C. It is therefore important to determine the temperature that the transducer “sees” during a test. The pressure sensors are mounted outside of the tunnel, so that their operating temperature is that of the room. Each transducer is submitted to the gas that has traveled along the 3”-long stainless steel tubes, which are initially at room temperature. The tubing hence modifies the gas temperature. In addition, heat must diffuse through the gas present in the tubes once their initial filling is complete. The time required for this transfer is on the order of the diffusive time scale  $L^2/\alpha$ , where  $L$  is equal to 3” and  $\alpha$  is the gas diffusivity, equal to  $18.8 \times 10^{-6} \text{ m}^2/\text{s}$ . This yields a characteristic time of 5 minutes, which is very large compared to the test duration. Alternatively heat can be conducted along the tube length. In that case, the characteristic time-scale for this process is 27 minutes. All this shows that the transducer temperature remains unchanged during the blow-down test and that the effects of temperature on the transducer output are negligible in this application. More information can be found in [5].

Upstream Total Pressure Total Error						
Run ID	gamma	Mach #	Head Loss	Transducer	Noise	Total
005	1,429	0,441	0,17%	0,12%	0,18%	0,28%
006	1,430	0,439	0,17%	0,12%	0,18%	0,28%
007	1,430	0,429	0,16%	0,12%	0,18%	0,27%
008	1,431	0,451	0,18%	0,12%	0,18%	0,28%
009	1,432	0,519	0,24%	0,12%	0,18%	0,33%
010	1,431	0,521	0,24%	0,12%	0,18%	0,33%
011	1,431	0,485	0,21%	0,12%	0,18%	0,30%
013	1,433	0,570	0,30%	0,12%	0,18%	0,37%
014	1,434	0,593	0,32%	0,12%	0,18%	0,39%

Table 4.2 – Upstream Total Pressure Uncertainty.

Downstream Total Pressure Total Error						
Run ID	gamma	Mach #	Head Loss	Transducer	Noise	Total
005	1,399	0,535	0,26%	0,19%	0,27%	0,42%
006	1,397	0,492	0,21%	0,19%	0,27%	0,39%
007	1,394	0,425	0,15%	0,19%	0,27%	0,36%
008	1,391	0,424	0,15%	0,19%	0,27%	0,36%
009	1,385	0,432	0,16%	0,19%	0,27%	0,37%
010	1,385	0,436	0,16%	0,19%	0,27%	0,37%
011	1,384	0,433	0,16%	0,19%	0,27%	0,37%
013	1,385	0,456	0,18%	0,19%	0,27%	0,38%
014	1,387	0,478	0,20%	0,19%	0,27%	0,38%

Table 4.3 – Downstream Total Pressure Uncertainty.

Total Upstream Static Pressure Error						
Run ID	gamma	Mach #	Head Loss	Transducer	Noise	Total
005	1.429	0.441	0.14%	0.13%	0.21%	0.29%
006	1.430	0.439	0.14%	0.13%	0.21%	0.28%
007	1.430	0.429	0.13%	0.13%	0.21%	0.28%
008	1.431	0.451	0.15%	0.13%	0.21%	0.29%
009	1.432	0.519	0.19%	0.13%	0.21%	0.32%
010	1.431	0.521	0.19%	0.13%	0.21%	0.32%
011	1.431	0.485	0.17%	0.13%	0.21%	0.30%
013	1.433	0.570	0.23%	0.13%	0.21%	0.34%
014	1.434	0.593	0.25%	0.13%	0.21%	0.35%

Table 4.4 – Total Upstream Static Pressure Error.

<b>Upstream Transducer Uncertainties</b>		
<b>Name</b>	<b>Transducer</b>	<b>Noise</b>
<b>PT0A</b>	0,12%	0,77%
<b>PT1A</b>	0,10%	0,35%
<b>PDMP</b>	0,50%	0,10%
<b>PT2ZR01</b>	0,12%	0,14%
<b>PT2ZR02</b>	0,16%	0,17%
<b>PPT2C</b>	0,15%	0,20%
<b>PT2ZR04</b>	0,09%	0,17%
<b>PT2ZR05</b>	0,11%	0,15%
<b>PPS2C</b>	0,12%	0,24%
<b>PT2ZR07</b>	0,12%	0,24%
<b>PT2ZR08</b>	0,14%	0,15%
<b>PT2A</b>	0,27%	0,19%
<b>PS2A</b>	0,10%	0,30%
<b>PPT2A</b>	0,14%	0,33%
<b>PPS2A</b>	0,16%	0,28%
<b>PT2B</b>	0,12%	0,13%
<b>PS2B</b>	0,12%	0,33%
<b>PT2C</b>	0,10%	0,15%
<b>PS2C</b>	0,11%	0,11%
<b>PW1</b>	0,09%	0,14%
<b>PPT2B</b>	0,09%	0,15%
<b>PPS2B</b>	0,09%	0,16%
<b>Average</b>	<b>0,14%</b>	<b>0,22%</b>

Table 4.5 – Upstream Transducer Uncertainty.

<b>Downstream Transducer Uncertainties</b>		
<b>Name</b>	<b>Transducer</b>	<b>Noise</b>
<b>PT5A</b>	0,05%	0,91%
<b>PPT5A</b>	0,06%	0,16%
<b>PPS5A</b>	0,02%	0,16%
<b>PT5ZR01</b>	0,06%	0,20%
<b>PT5ZR02</b>	0,02%	0,31%
<b>PT5ZR03</b>	0,03%	0,23%
<b>PT5ZR04</b>	0,08%	0,32%
<b>PT5ZR05</b>	0,06%	0,37%
<b>PT5CR01</b>	0,16%	0,19%
<b>PT5CR02</b>	0,13%	0,18%
<b>PT5CR03</b>	1,11%	0,49%
<b>PT5CR04</b>	0,18%	0,14%
<b>PT5CR05</b>	0,10%	0,24%
<b>PS3HS</b>	0,13%	0,47%
<b>PS5AHS</b>	0,09%	0,14%
<b>Average</b>	<b>0,15%</b>	<b>0,30%</b>

Table 4.6 – Downstream Transducer Uncertainty.

## **5. Aerodynamic Performance Measurement**

### ***5.1. Introduction***

The two previous chapters discussed the uncertainties related to the instruments used in the tunnel. The purpose of the experiment is to determine the aerodynamic efficiency of the compressor. The most accurate way to compute the efficiency of the compressor is to resort to NIST tabulated values of the thermodynamic properties of the gas mixture used in the tunnel. The facility runs in non-adiabatic conditions, the specific heat ratio changes across the compressor and the mass-flow is not constant because of the aspiration process on rotor 2. Consequently, we cannot rely on the traditional equations to compute the efficiency. Here is how the process followed in this case unfolds:

- A gas table is created out of the NIST tables for the gas mixture used.
- The raw voltage data are converted to engineering units, using the AutoCal.m program for the pressure transducers and the individual Matlab calibration files for the thermocouples. This data is then processed through a first order low-pass filter with a lowpass frequency of 12 Hz, to eliminate the noise.
- The total upstream rake pressures and temperatures are area-averaged. The gas tables allow determination of the corresponding total upstream enthalpy.

- The static temperature is computed using the total temperature and pressure as well as the measured static pressure in the gas table on a constant entropy line.
- The inlet velocity of the fluid is then derived from the difference between the total and the static enthalpy of the incoming gas. The gas tables help determine the gas density and the sound velocity for these parameters. An inlet Mach number is derived accordingly.
- The downstream total pressure, along with the upstream total parameters help compute what the isentropic total downstream temperature would be. This allows to determine the downstream total isentropic enthalpy.
- The efficiency is then computed:

$$\eta = \frac{h_{0-Dn-Isen} - h_{0-Up}}{h_{0-Dn-ind} - h_{0-Up}}$$

where  $h_{0-Dn-Isen}$  is the downstream total isentropic enthalpy of the gas,  $h_{0-Up}$  is the upstream total enthalpy and  $h_{0-Dn-ind}$  is the indicated downstream total enthalpy. Further information can be obtained in [2].

We now want to estimate the uncertainty in the measurement of the efficiency. Two ways are possible to reach this goal. The first way consists in perturbing the inputs to the efficiency calculation program described previously by the amount of error computed for each type of instruments. These perturbations can be added or subtracted to the recorded signals. Several combinations are hence possible. The uncertainty will then be given by the difference between the efficiency computed without any perturbations and the one computed with perturbations yielding the largest difference. A second way to calculate the impact instrument errors have on the efficiency uncertainty is to reinforce the assumptions about the thermodynamic process the gas is undergoing in the tunnel so as to be able to derive an analytical equation of the uncertainty. In this respect, we have to assume that the compressor is working adiabatically, that the gas mixture is ideal, that the mass-flow through the compressor is constant (no aspiration) and that the specific heat ratio remains unchanged in the compression. Under these circumstances, we can derive a first order approximation of the uncertainty associated to the efficiency calculation.

Recording data in discrete and limited locations in the tunnel triggers further uncertainty. We will address this question, along with the issues set by the time sampling of the parameters.

Finally in this chapter, we will explain the difference between the measured efficiency and the adiabatic efficiency and assess the amplitude of correction needed to be provided to obtain an equivalent adiabatic efficiency from our measurements.

## ***5.2. Uncertainty of Adiabatic Efficiency Measurement***

### **5.2.1. Uncertainty due to Instrumentation Imperfections**

The first method was applied for the results of run 010. The maximum difference between a perturbed signal efficiency calculation and the direct calculation amounts to 0.131 points of efficiency.

The analytical method requires starting from the definition of the adiabatic efficiency for a compressor operated with an ideal gas, for a constant mass flow and specific heat ratio. It is given by

$$\eta = \frac{\pi^{\frac{\gamma-1}{\tau}} - 1}{\tau - 1} \quad (5.1)$$

The efficiency  $\eta$  is a function of the pressure ratio  $\pi$ , the temperature ratio  $\tau$  and the specific heat ratio  $\gamma$ . Knowing that these parameters are independent from one another, the absolute error in efficiency as a function of the absolute uncertainty in pressure ratio, temperature ratio and specific heat ratio is given by the following equation [12]:

$$U_{\eta}^2 = \left(\frac{\partial \eta}{\partial \pi}\right)^2 U_{\pi}^2 + \left(\frac{\partial \eta}{\partial \tau}\right)^2 U_{\tau}^2 + \left(\frac{\partial \eta}{\partial \gamma}\right)^2 U_{\gamma}^2 \quad (5.2)$$

where  $U_X$  is the absolute uncertainty in  $X$ .

A more useful expression is that using the relative uncertainties in the pressure, temperature and specific heat ratios:

$$U_{\eta}^2 = \left( \pi \frac{\partial \eta}{\partial \pi} \right)^2 \left( \frac{U_{\pi}}{\pi} \right)^2 + \left( \tau \frac{\partial \eta}{\partial \tau} \right)^2 \left( \frac{U_{\tau}}{\tau} \right)^2 + \left( \gamma \frac{\partial \eta}{\partial \gamma} \right)^2 \left( \frac{U_{\gamma}}{\gamma} \right)^2 \quad (5.3)$$

From the definition of the pressure ratio and the temperature ratio, we can derive expressions of uncertainties of these parameters as a function of the relative uncertainties in upstream and downstream temperatures and pressures:

$$\left( \frac{U_{\pi}}{\pi} \right)^2 = \left( \frac{U_{Pup}}{Pup} \right)^2 + \left( \frac{U_{Pdn}}{Pdn} \right)^2 \quad (5.4)$$

$$\left( \frac{U_{\tau}}{\tau} \right)^2 = \left( \frac{U_{Tup}}{Tup} \right)^2 + \left( \frac{U_{Tdn}}{Tdn} \right)^2 \quad (5.5)$$

The uncertainty equation (5.2) shows that each error is multiplied by a coefficient obtained from the differentiation, which defines the impact a variation in one parameter will have over the sought uncertainty. From equations (5.4) and (5.5), we can see that the upstream and downstream parameters are multiplied by the same magnification factors. These are:

$$\frac{\partial \eta}{\partial \pi} = \frac{\gamma - 1}{\gamma(\tau - 1)} \cdot \pi^{\frac{-1}{\gamma}} \quad (5.6)$$

$$\frac{\partial \eta}{\partial \tau} = \frac{1 - \pi^{\frac{\gamma-1}{\gamma}}}{(\tau - 1)^2} \quad (5.7)$$

$$\frac{\partial \eta}{\partial \gamma} = \frac{\pi^{\frac{\gamma-1}{\gamma}} \ln(\pi)}{\gamma^2(\tau - 1)} \quad (5.8)$$

Using the results from each of the runs, we are able to compute the first order uncertainty for each efficiency measurement. The results are presented in Table 5.2 and Table 5.3. We can notice that the magnification coefficient for the temperature is three times larger than that of the pressure and that the influence of the specific heat ratio is not to be minimized. The relative uncertainty of the specific heat ratio is approximated to the first order by the error in gas mixture computed for each run.

Using these equations and the results from the error analysis from the previous chapters, we can compute a first order approximation of the adiabatic efficiency

uncertainty. The error is systematically smaller than one point of efficiency for each of the runs performed.

The first method yields much better results than the analytical method. For run 010, the second method gives an uncertainty of 0.660 points of efficiency compared to 0.131 points for the empirical method, which corresponds to an approximate ratio of 5.

### **5.2.2. Uncertainty Due to Discrete Spatial Sampling**

For practical reasons, the MIT Blow-Down compressor facility allows only a discrete spatial data sampling. As was explained in section 2.4.1, single instrumentation probes are scattered circumferentially in three equally spaced sectors. Similarly, the pressure and temperature rakes only allow a discrete sampling of the radial distribution of the aerodynamic parameters of the flow. Assessing the amount of uncertainty linked to these aspects appears as an issue of interest.

In terms of radial distribution, the dimensions of the pressure impact heads and total temperature heads did not allow to adequately sample data in the end wall boundary layer. To assess a level of uncertainty in that respect, calculations were made using the 100% - 100% CFD simulation results. The radial area averaged values of the compressor's pressure and temperature ratios and efficiency were computed in two different ways based on the same set of CFD calculations. The first way consisted in using the complete spanwise set of data. The second consisted in only using the values corresponding to the same span locations as the actual probes on the rakes. These values were scaled by the adequate surface area associated with their location. The results of these calculations are presented in Table 5.1. Under sampling of the end wall conditions seems to have a significant impact on the efficiency calculation.

	<b>Complete sampling</b>	<b>Actual Sampling</b>	<b>Uncertainty</b>
<b>Pressure Ratio</b>	2.97	3.00	0.96
<b>Temperature Ratio</b>	1.43	1.42	0.25
<b>Efficiency</b>	86.07%	87.55%	1.73

Table 5.1 – Radial Sampling Uncertainty.

Circumferentially, the total and static pressure measurements have recorded a pressure distortion in the inlet plane of the compressor. A thorough examination of the pressure screen has proved that the screen hole pattern is not uniform, which would tend to explain this phenomenon. More explanations are given in [2]. Assuming the total pressure in front of the screen is uniform, these hole measurements permit a determination of a total pressure value in each 20° section of the inlet area. Run measurements showed that distortions were only limited to pressure and did not involve temperature. An uncertainty is directly related to this pressure distribution. To assess the impact on the overall compressor measurements, the concept of parallel compressors is used. Each section sees the same compressor, with the same characteristic. Similarly, each outlet section is associated to the inlet section with the same azimuthal position. But its corresponding corrected mass-flow differs from the average corrected mass-flow computed from the actual runs by a factor equal to the ratio of the average inlet total pressure to the total pressure in the section. Using the compressor map established from the full speed runs 010, 011, 013 and 014, we are able to establish a pressure and a temperature ratio for each section and to compute the corresponding outlet values. These calculations permit one see the circumferential entropy structure of the flow, both upstream and downstream of the compressor. The relative entropy variation is plotted in Figure 5.1.

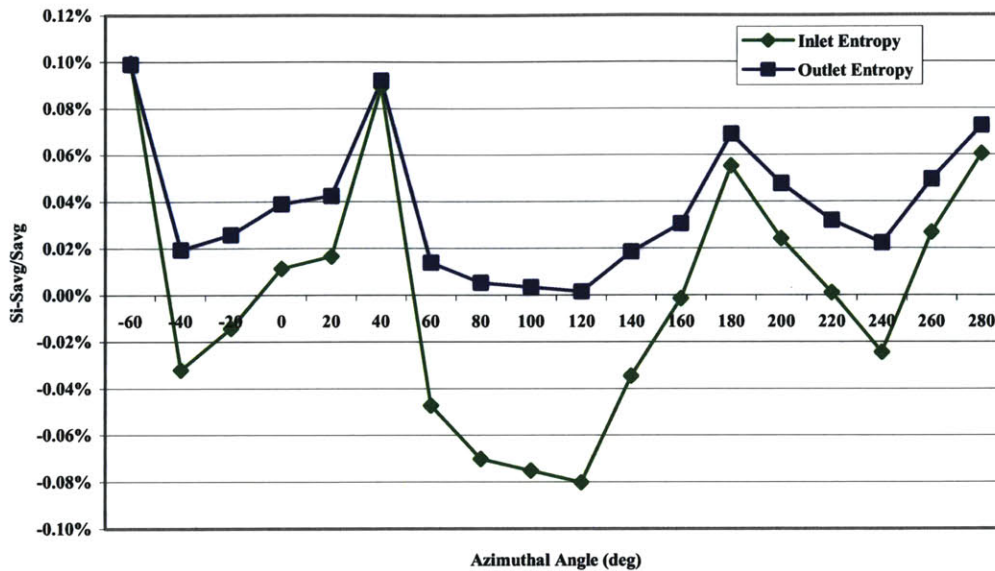


Figure 5.1 – Inlet and Outlet Relative Entropy Variations.

The compressor seems to have increased the average relative entropy variation from section to section from 0.0003% to 0.0381%, but reduced the corresponding standard deviation. The concept of parallel compressors is responsible for the similar shapes of the variation curves upstream and downstream of the compressor. The maximum variation points are located in the sections where the inlet total pressure is smaller than the average pressure, which is caused by a smaller number of holes in these locations.

Beyond this first calculation, an area averaged value of the total temperature and pressure can be computed for each section, upstream and downstream of the compressor. These values can be compared to the temperature and pressure values used in the effective calculation of the efficiency, which yields the relative circumferential uncertainty in pressure and temperature. Using the same uncertainty measurement technique as in section 5.2.2, the spatial efficiency uncertainty can be estimated. Calculations showed an absolute uncertainty of 0.95%. These changes are first order estimations of how the compressor reacts to variations in corrected mass-flow. We should

underscore the fact that the compressor map used to compute the downstream parameters comes from a manual extrapolation of test runs.

### **5.2.3. Uncertainty Due To Time Sampling**

As pointed out in section 4.5, noise coming from the electrical environment is part of the signals recorded of the various instrument channels. This noise can account for a relative error of 0.2% to 0.30% on the pressure probes for instance. To adequately remove the perturbation linked to this phenomenon, a low pass filter is used in the data processing. To implement this filter in the case of a discrete set of data, a running average method is used. It is very important that the filter does not entail any phase distortion in the signal. The filter used first processes in the forward direction, then reverses the filtered sequence and runs it back in the filter. Although the cutting frequency was originally set at 60 Hz, it proved to be around 12 Hz, attenuating all signals with a higher frequency at the rate of 20 dB/decade. This technique does not add any uncertainty to the measurements.

### ***5.3. Non-Adiabatic Effects in a Blow-Down Test Environment***

In a steady state test rig, a compressor operates virtually adiabatically – there is very little heat transfer between the working gas and the walls. This is why the efficiency of a compressor is always referred to as the adiabatic efficiency. In a short-duration test facility, the tunnel will stay at near room temperature, the characteristic test time scale remains very short compared to the time needed for the tunnel to reach the fluid temperature. Calculations show that in a short-duration test facility, the walls are isothermal but the blades see a small variation in temperature. Hence, a certain amount of heat is transferred from the test gas to the walls of the facility as well as the compressor blades and hub casing.

In this chapter, we will first focus on the implications this phenomenon has on the compression process. We will then discuss how to correct the measured efficiency to estimate the equivalent adiabatic efficiency.

### 5.3.1. Difference Between Blow-Down Efficiency and Adiabatic Efficiency

The difference between an adiabatic compression and the compression in a blow-down environment is illustrated in Figure 5.2. All state parameters are stagnation quantities. Subscript “1” represents the compressor inlet conditions and subscript “2” the outlet conditions. Three compression processes are plotted on the figure. They represent three thermodynamic paths to raise the gas pressure from  $P_{01}$  to  $P_{02}$ .

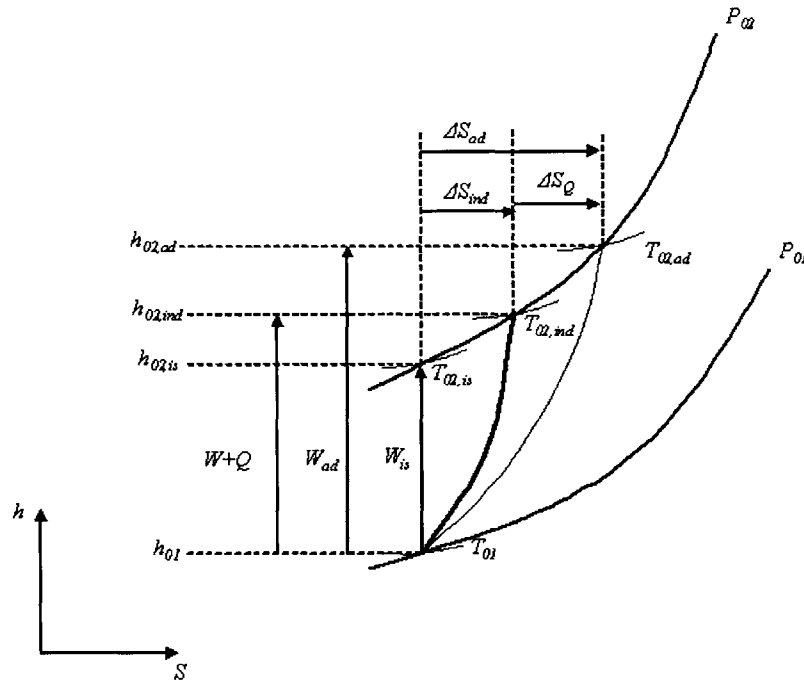


Figure 5.2 – Enthalpy – Entropy Diagram for the Compression Processes in Compressors.

For an ideal compression, the entropy rise across the compressor is equal to zero. The exit enthalpy  $h_{02, is}$  can be computed from the isentropic relations for an ideal gas with constant specific heat ratio  $\gamma$ .

$$\frac{T_{02, is}}{T_{01}} = \left( \frac{P_{02}}{P_{01}} \right)^{\frac{\gamma-1}{\gamma}} \quad (5.9)$$

The ideal work corresponds to the case where the compressor would work without any loss.

$$W_{is} = h_{02,is} - h_{01} \quad (5.10)$$

Real compressors operate with losses. The actual compression work to achieve the same pressure ratio is hence larger. Under adiabatic conditions, we define the adiabatic work  $W_{ad}$  as the difference between the adiabatic exit enthalpy  $h_{02,ad}$  (actually measured in steady state test rigs), for state conditions  $P_{02}$  and  $T_{02,ad}$ , and the inlet total enthalpy  $h_{01}$ :

$$W_{ad} = h_{02,ad} - h_{01} \quad (5.11)$$

Consequently, the adiabatic efficiency yields as the ratio of these two thermodynamic transformations:

$$\eta_{ad} = \frac{h_{02,is} - h_{01}}{h_{02,ad} - h_{01}} \quad (5.12)$$

As explained above, the blow-down compressor does not allow the measurement of an adiabatic compression. It only yields indicated values. The exit temperature is an indicated value  $T_{02,ind}$  which corresponds to an indicated exit total enthalpy  $h_{02,ind}$ . The enthalpy rise in the flow stems hence from two exchange sources: work  $W$  and the wall heat transfer  $Q$ .

$$h_{02,ind} - h_{01} = W + Q \quad (5.13)$$

We can define the corresponding indicated efficiency that comes out of the post processing of the data recorded during the tests:

$$\eta_{ind} = \frac{h_{02,is} - h_{01}}{h_{02,ind} - h_{01}} \quad (5.14)$$

We can easily derive a relation between the indicated and the adiabatic efficiencies:

$$\frac{1}{\eta_{ind}} = \frac{h_{02,ind} - h_{01}}{h_{02,is} - h_{01}} = \frac{h_{02,ad} - h_{01}}{h_{02,is} - h_{01}} + \frac{h_{02,ind} - h_{02,ad}}{h_{02,is} - h_{01}} \quad (5.15)$$

$$\frac{1}{\eta_{ind}} = \frac{1}{\eta_{ad}} + \frac{h_{02,ind} - h_{02,ad}}{h_{02,is} - h_{01}} \quad (5.16)$$

Assessing the correction to provide to the indicated efficiency comes down to estimating the adiabatic exit total enthalpy.

### 5.3.2. Correction to provide to Measured Efficiency

Equation (5.16) shows that it is necessary to estimate the exit adiabatic total temperature to assess the correction to provide. According to Figure 5.2, the loss difference in enthalpy rise is due to the heat exchange between the flow and the facility walls. The problem comes down to estimating this exchange as well as its impact on the efficiency. To do so, we first estimate the heat exchange between the fluid and the walls using a one-dimensional compressible flow analysis. The surface heat transfer coefficient is computed from an estimation of the Stanton number. The lump capacity model is used to calculate the heat transfer with the blades while the semi-infinite body model is used for the transfers with the compressor's tip and hub casings. More details are given in Appendix A. Second, we derive an equation linked to the properties of entropy. Entropy is a thermodynamic state quantity. It hence only depends on the initial and final state conditions of the fluid. Therefore, the entropy generated in an adiabatic compressor can be viewed as the sum of two parts: the entropy generated in a blow-down facility and the entropy change due to the heat transfer:

$$\Delta S_{ad} = \Delta S_{ind} + \Delta S_{\varrho} \quad (5.17)$$

where  $\Delta S_{\varrho}$  for a reversible heat transfer can be quantified as

$$\Delta S_{\varrho} = \int \left( \frac{\delta Q}{T} \right)_{rev} = \frac{Q}{T^*} \quad (5.18)$$

The temperature  $T^*$  is the equivalent temperature at which the heat transfer takes place in the compressor.

For an ideal gas, the entropy change can be written as

$$\Delta S = S_2 - S_1 = C_p \cdot \ln \left( \frac{T_{02}}{T_{01}} \right) - R \cdot \ln \left( \frac{P_{02}}{P_{01}} \right) \quad (5.19)$$

This expression can be modified in the following form:

$$\frac{P_{02}}{P_{01}} = \left[ \frac{T_{02}}{T_{01}} \cdot \exp\left(-\frac{\Delta S}{C_p}\right) \right]^{\frac{\gamma}{\gamma-1}} \quad (5.20)$$

The two thermodynamic paths of interest correspond to the same pressure ratio. So, using equation (5.20), we can assert that:

$$\frac{T_{02,ad}}{T_{01}} \cdot \exp\left(-\frac{\Delta S_{ad}}{C_p}\right) = \frac{T_{02,ad}}{T_{01}} \cdot \exp\left(-\frac{\Delta S_{ind} + \Delta S_Q}{C_p}\right) = \frac{T_{02,ind}}{T_{01}} \cdot \exp\left(-\frac{\Delta S_{ind}}{C_p}\right) \quad (5.21)$$

This equation unveils the following relation:

$$T_{02,ad} = T_{02,ind} \cdot \exp\left(\frac{\Delta S_Q}{C_p}\right) \quad (5.22)$$

We presume that the difference in entropy due to heat exchange is very limited in amplitude. We thus decide to apply a first order Taylor series around zero to get an simpler expression.

$$T_{02,ad} = T_{02,ind} \cdot \left(1 + \frac{\Delta S_Q}{C_p}\right) \quad (5.23)$$

or

$$T_{02,ad} = T_{02,ind} \cdot \left(1 + \frac{Q}{C_p T^*}\right) \quad (5.24)$$

Hence, the sought difference between the exit adiabatic total enthalpy and the indicated value can be approximated as follows:

$$h_{02,ad} - h_{02,ind} = Q \frac{T_{02,ind}}{T^*} \quad (5.25)$$

and finally:

$$\frac{1}{\eta_{ind}} = \frac{1}{\eta_{ad}} - \frac{Q}{h_{02,is} - h_{01}} \frac{T_{02,ind}}{T^*} \quad (5.26)$$

This equation shows the impact the heat transfer has on the correction to be provided to the indicated efficiency. The difference between the inverse of both the indicated and the adiabatic efficiencies is proportional to the heat transfer, scaled by a

temperature ratio that needs to be further assessed. The temperature  $T^*$  defined in equation (5.18) is the equivalent temperature at which the heat transfer would occur in the compressor. In reality, this heat transfer takes place at the various locations that are at different temperatures. The upper bound is the indicated exit temperature and the lower bound is the inlet temperature. A larger and hence more reliable correction is obtained with the latter bound. The scaling coefficient is then equal to the temperature ratio across the compressor. A model based on the blow-down time constant yields a difference between the indicated and the adiabatic efficiencies of about 0.1% for an indicated value of 87%, which corresponds to the value obtained at a 100% speed (Figure 5. 3). The correction is hence very small.

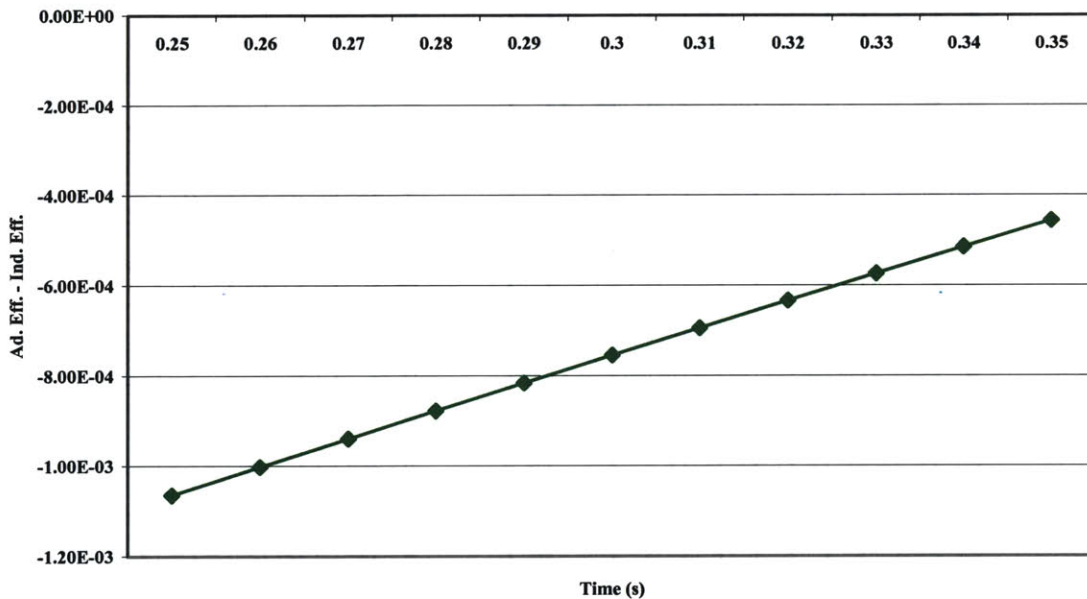


Figure 5. 3 – Difference Between Adiabatic and Indicated Efficiency Over the Test Time.

Run ID	Avg PR	Avg TR	Meas. Eff	Abs Tt Uncertainty		Relative Uncertainty				
				Up (K)	Dn	Up Pt	Dn Pt	Up Tt	Dn Tt	gamma
005	1.983	1.266	0.792	0.142	0.327	0.31%	0.42%	0.05%	0.10%	0.15%
006	2.103	1.287	0.811	0.142	0.327	0.31%	0.39%	0.05%	0.09%	0.16%
007	2.303	1.315	0.842	0.142	0.327	0.31%	0.36%	0.05%	0.09%	0.23%
008	2.468	1.351	0.840	0.142	0.327	0.32%	0.36%	0.05%	0.09%	0.29%
009	2.973	1.415	0.868	0.142	0.327	0.36%	0.37%	0.05%	0.09%	0.03%
010	2.915	1.406	0.873	0.142	0.327	0.36%	0.37%	0.05%	0.09%	0.15%
011	2.899	1.422	0.836	0.142	0.327	0.34%	0.37%	0.05%	0.09%	0.01%
013	2.910	1.398	0.888	0.142	0.327	0.40%	0.38%	0.05%	0.09%	0.05%
014	2.836	1.382	0.885	0.142	0.327	0.42%	0.38%	0.05%	0.09%	0.10%

Table 5.2. – Absolute and Relative Uncertainties in Total Temperature and Pressure Measurements for Runs 005 to 014.

Run ID	Error Coefficients			Uncertainty Per Measurement					Efficiency Uncertainty
	Eff*UMF P	Eff*UMF T	Eff*UMF Gamma	Up Pt	Dn Pt	Up Tt	Dn Tt	gamma	
005	1.347	-3.142	2.225	0.42%	0.56%	-0.16%	-0.30%	0.34%	0.85%
006	1.267	-2.952	2.280	0.40%	0.50%	-0.16%	-0.28%	0.36%	0.80%
007	1.182	-2.780	2.393	0.36%	0.43%	-0.15%	-0.26%	0.55%	0.84%
008	1.080	-2.446	2.375	0.34%	0.39%	-0.13%	-0.22%	0.69%	0.90%
009	0.959	-2.159	2.558	0.34%	0.35%	-0.11%	-0.19%	0.07%	0.54%
010	0.973	-2.205	2.552	0.35%	0.36%	-0.12%	-0.19%	0.37%	0.66%
011	0.935	-2.032	2.442	0.31%	0.34%	-0.11%	-0.18%	0.03%	0.51%
013	0.995	-2.297	2.598	0.39%	0.37%	-0.12%	-0.20%	0.13%	0.61%
014	1.033	-2.433	2.622	0.43%	0.40%	-0.13%	-0.22%	0.25%	0.69%

Table 5.3. – Scaling Coefficients, Scaled Uncertainties in Temperature, Pressure and Specific Heat Ratio and Efficiency Uncertainty for Runs 005 to 014.

## **6. Experimental Results**

### ***6.1. Introduction***

Fourteen runs of the blow-down counter-rotating aspirated compressor were performed, with rotor speeds of 90%-90%, 95%-95% and 100%-100%. This chapter presents the preliminary test runs performed to check the integrity of the compressor as well as the setting adjustments. Attention is then focused on the following runs, where the two rotor corrected speeds are matched. Finally, a tentative compressor map is presented.

### ***6.2. Test Data***

#### **6.2.1. Preliminary Tests**

Six preliminary tests were necessary to verify the operation of the compressor, ensuring its mechanical integrity and learning to match the two rotor corrected speeds. During the four first tests, the compressor's mechanical speed was set to have the rotors' corrected speeds reach 85% of their design values. Data showed that the facility behaved without any mechanical problems and that it was able to deliver a quasi-steady operating state between 200 ms and 600 ms after the firing of the fast acting valve. The entire set of instruments survived the physical constraints imposed by the dynamic pressure of the

flow as well as the facility vibrations. However, some additional setting adjustments appeared necessary. While rotor 1 behaved properly and as expected, rotor 2 corrected speed did not match rotor 1's. It actually reached values above 90% at the end of the quasi-steady state, as shown in Figure 6.1. This phenomenon revealed that rotor 2 was not putting out enough work, due to too low a back pressure. This parameter is set by a throttle located at the rear of the aft section, separating the compressor flow passage from the dump tank. Closing this throttle too much causes the rotor to stall. To avoid that, a safety margin on the calculation of the adequate opening of the throttle was implemented. Reducing progressively this margin allowed the two rotor corrected speeds to match. Meanwhile, the upstream instrumentation pointed out a pressure and a temperature distortion in the inlet plane of the compressor. Adding two electrical fans in the supply tank to improve the mixing of the argon with the carbon dioxide helped get rid of the temperature gradient in the inlet plane, while improving the filling time of the supply tank. As for the pressure distortion, it persisted both for the total and the static values. The source of this phenomenon was investigated and results showed that non-uniformity in the pressure screen hole pattern may account for these discrepancies. More information can be found in [2].

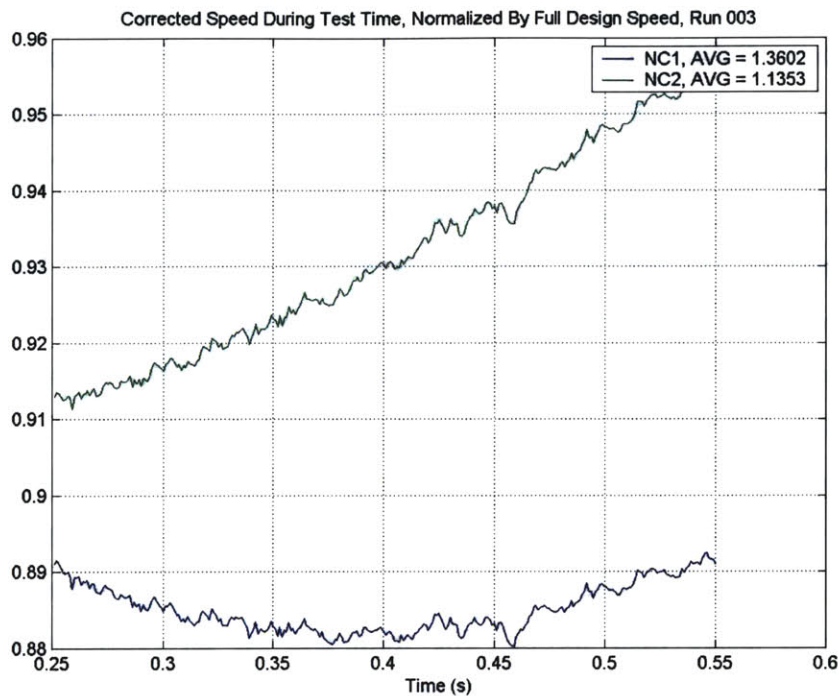


Figure 6.1 – Corrected Speeds During Test Time Normalized by Full Design Speed – Run 003.

### 6.2.2. Matched Corrected Speed Run Results

The two rotor corrected speeds were matched from run 007 to run 014. In this section, we will only comment on the results from run 010, which correspond to a 100% - 100% speed run.

The histories of the inlet and exit total temperatures are shown in Figure 6.2 and Figure 6.3. Three upstream and one downstream single total temperature probes placed at mid-span were used for this test along with the upstream and the two downstream rakes. A first remark is that all probes are able to observe the compressional heating mentioned in section 3.4.1. Figure 6.2 shows that between 220 ms and 500 ms, the temperature decreases almost linearly. This interval corresponds to the quasi-steady state of the compressor. To improve the study of the compressor and the better assess its performances, the time window considered for the post processing steps was limited to the interval between 250 ms and 350 ms. This corresponds to the early part of the quasi-

steady state period. Data proved to be more linear and undergoing less variation in that time window. Besides, the end of the quasi-steady state proved to be difficult to determine accurately from run to run. 350 ms turned out to be a safe value in that respect. The total temperature rakes give a radial profile of the temperature distribution upstream and downstream of the compressor (cf. Figure 6.4). The upstream rake tends to show a classic temperature pattern with higher temperatures near the end walls. The downstream rake showed however a more original distribution, with a quasi-linear spanwise growth in temperature. A drop was nonetheless recorded near the outer end-wall where heat exchanges are taking place.

The history of the area-averaged pressures in each section of the tunnel is pictured in Figure 6.5. In both the upstream and the downstream sections of the compressor, it takes 750 ms after the opening of the fast-acting valve for the pressures to become homogeneous inside each section. The front and the aft pressures then converge asymptotically. The upstream total and static pressure measurements show a persistent distortion in the inlet plane of the compressor on the order of 2% from window to window (Figure 6.6 and Figure 6.7). We remind the reader that the single pressure measurement probes are located in windows located  $120^\circ$  apart from one another. The upstream and downstream Pitot probe measurements are presented in Figure 6.8 and Figure 6.9. They allow a first order estimation of the flow Mach numbers. Their measurements are associated to the other total and static pressure measurements and used as input data to the NIST gas tables that yields the flow speeds, the sound velocities and hence the Mach number at the various stages of the machine for non-ideal gases. As for the upstream and downstream total pressure rakes, their measurements over the test-time are gathered in Figure 6.10 and Figure 6.11. The radial pressure patterns are presented in Figure 6.12. While the upstream rake is recording a uniform span distribution, the downstream rakes show a significant drop in the outer casing region. The rotors tip clearance could account for this fact.

The rake measurements can be converted into radial performance distribution, as plotted in Figure 6.13. The most striking aspect of this representation is the efficiency greater than 1 in the hub region of the compressor. Studies have shown that this

phenomenon is due to radial convection of losses around that region. This uncovers a limit to the assumption which associates the flow parameters of each downstream relative radial position to the flow parameters for the same upstream relative radial position.

A high speed static pressure probe was placed behind each rotor to better observe any stall of the compressor. A Fourier analysis permitted determination of the frequencies content. Theoretically, when rotor 2 is not stalled, its high static signal should mostly consist of rotor 2 and rotor 1 blade passage frequencies as well as a coupling phenomenon between the two rotors. Once other frequencies start growing in amplitude, the rotor is considered stalled. However, the limit between the two states for rotor 2 did not prove to be very obvious. Some stall is feared to have taken place during the time window of interest for runs 007 to 009. The pressure in the supply tank was lowered to overcome this issue.

The Mach numbers are plotted in Figure 6.16. The downstream value turned out to remain constant over the period of interest, but a significant decrease affected the upstream value.

Figure 6.17 show the rotor's normalized corrected speeds. Between 250 ms and 350 ms, the two speeds matched to less the 0.1% of the design speed. Such an achievement is made possible by an appropriate setting of the back pressure via the throttle opening and the matching of the inertias of the two rotors to the work ratio across the compressor. The curved shape of the speed variations during the quasi-steady state time recall the second order polynomial predicted by the programs used to scale the tunnel. Positioning the minimum value of the corrected speed in the appropriate time window is depending on the supply tank pressure.

The compressor performances are summarized in Figure 6.19 and Figure 6.20, which display very promising results. A pressure ratio of 2.95 and a temperature ratio of 1.41 for an efficiency of 0.886 were recorded on average between 250 ms and 350 ms. For the full design speed runs, the CFD simulated a pressure ratio of 3.06 and a temperature ratio of 1.43 for an efficiency of 87% (table 2.2).

The initial operating conditions, as well as the performance results at 250 ms for each run are summarized in Table 6.1.

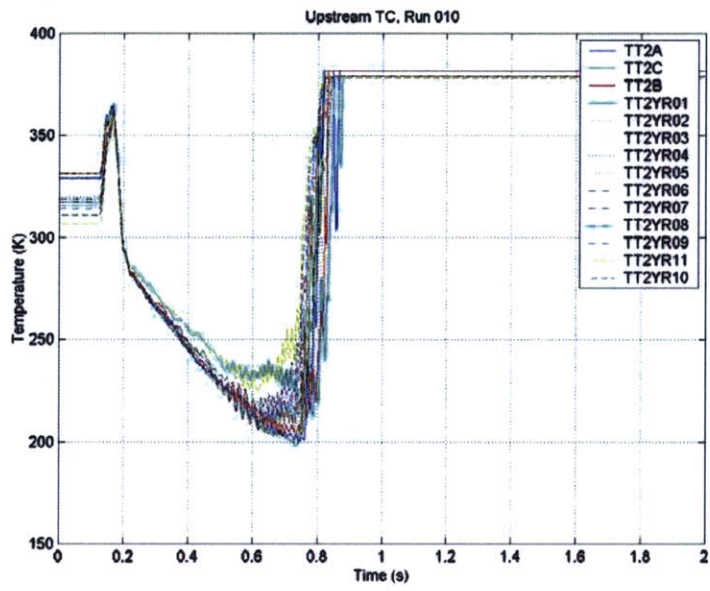


Figure 6.2 – Upstream Total Temperatures of Run 010.

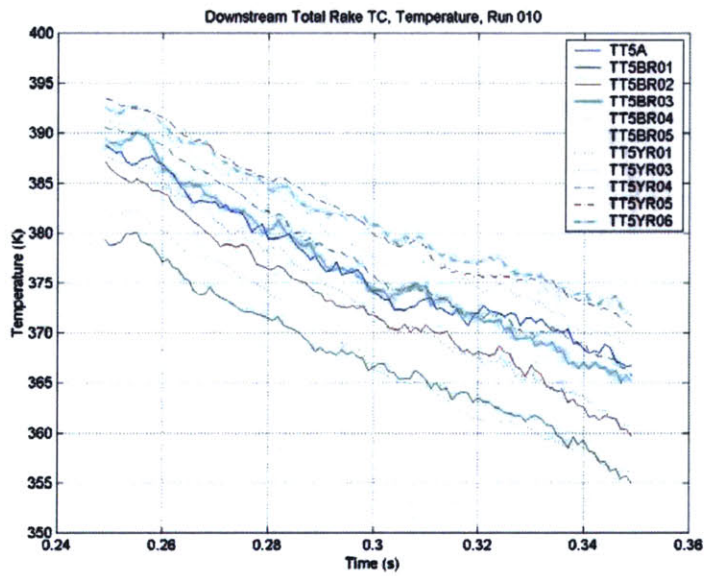


Figure 6.3 – Downstream Total Temperatures of Run 010.

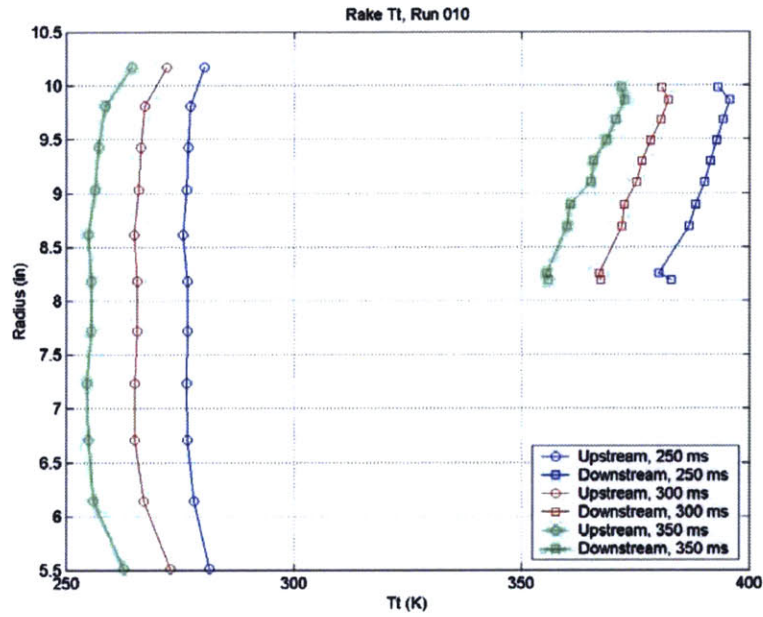


Figure 6.4 – Upstream and Downstream Radial Total Temperature Distribution at 250 ms, 300 ms and 350 ms for Run 010.

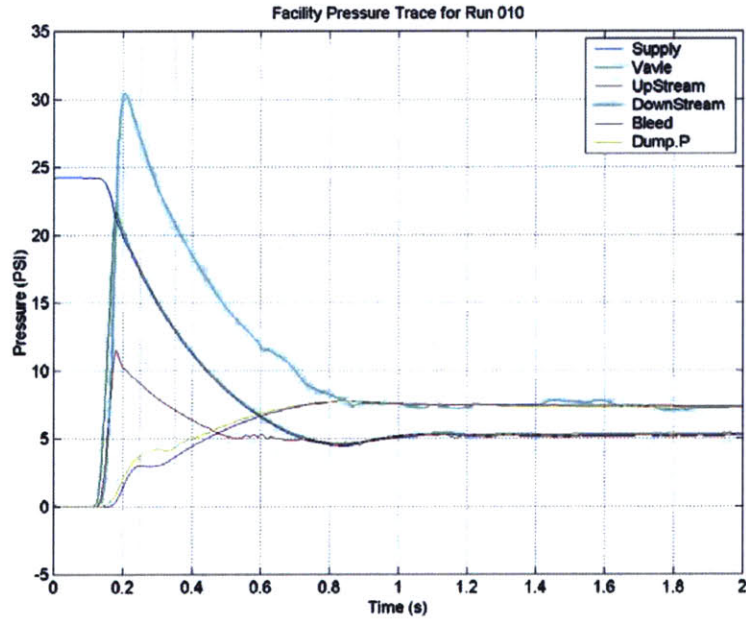


Figure 6.5 – Area-Averaged Pressure History in the Supply Tank, the Valve, Upstream and Downstream of the Compressor, in the Bleed Flow and in the Dump Tank for Run 010.

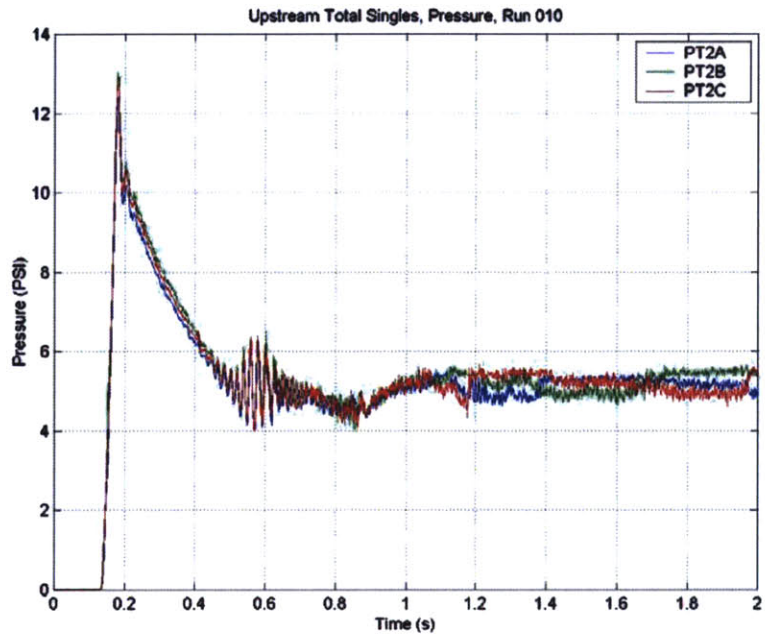


Figure 6.6 – Upstream Total Pressure at Three Midspan Locations for Run 010.

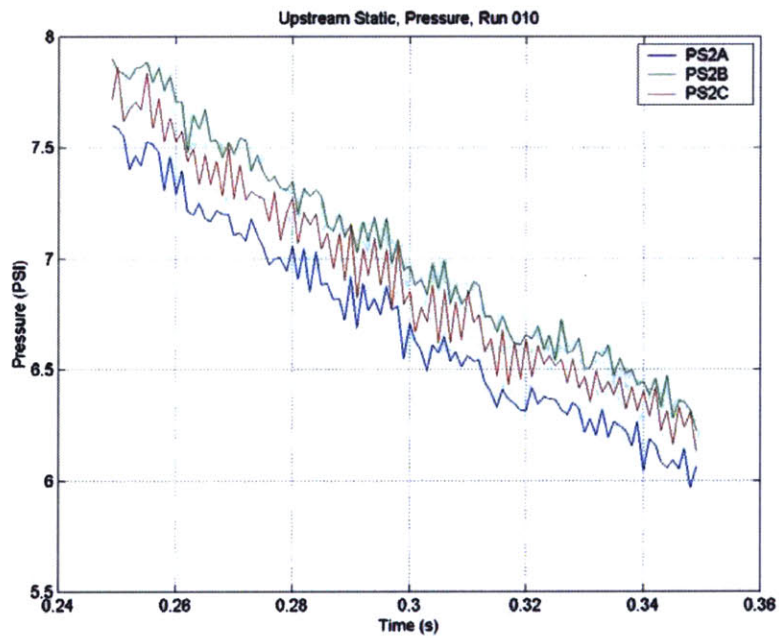


Figure 6.7 – Upstream Static Pressure Distribution for Run 010.

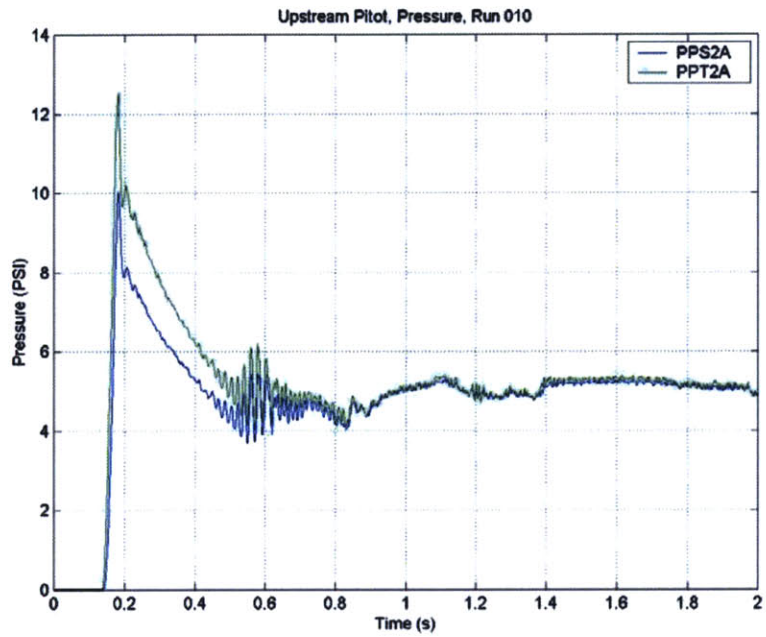


Figure 6.8 – Upstream Pitot Total and Static Pressures for Run 010.

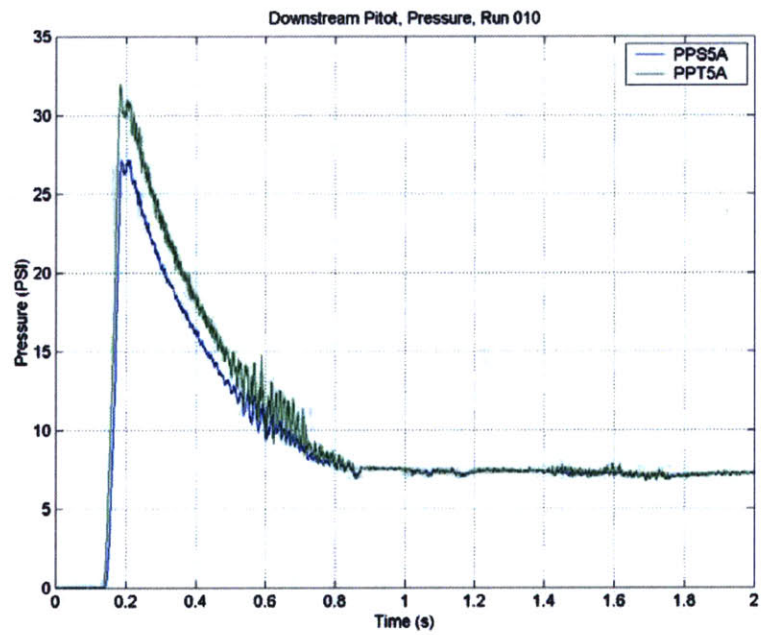


Figure 6.9 – Downstream Pitot Total and Static Pressures for Run 010.

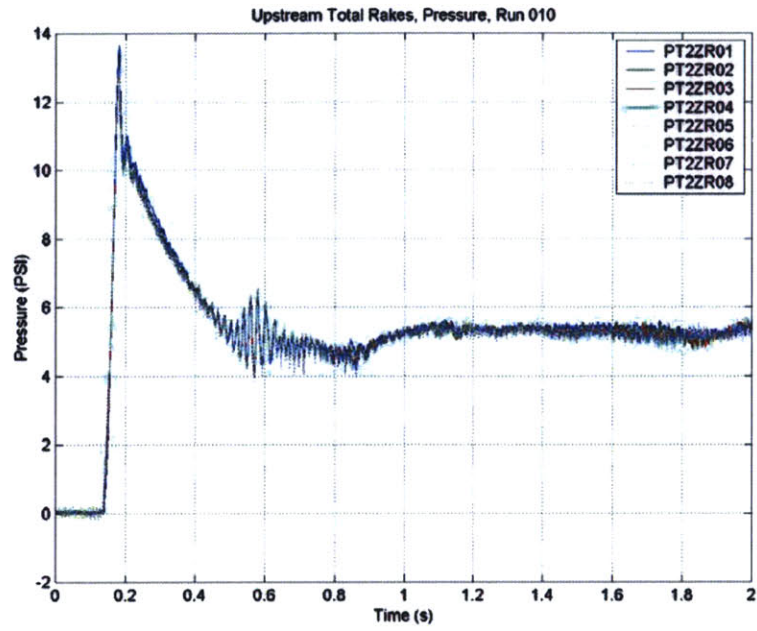


Figure 6.10 – Upstream Total Pressure Rake Measurements for Run 010.

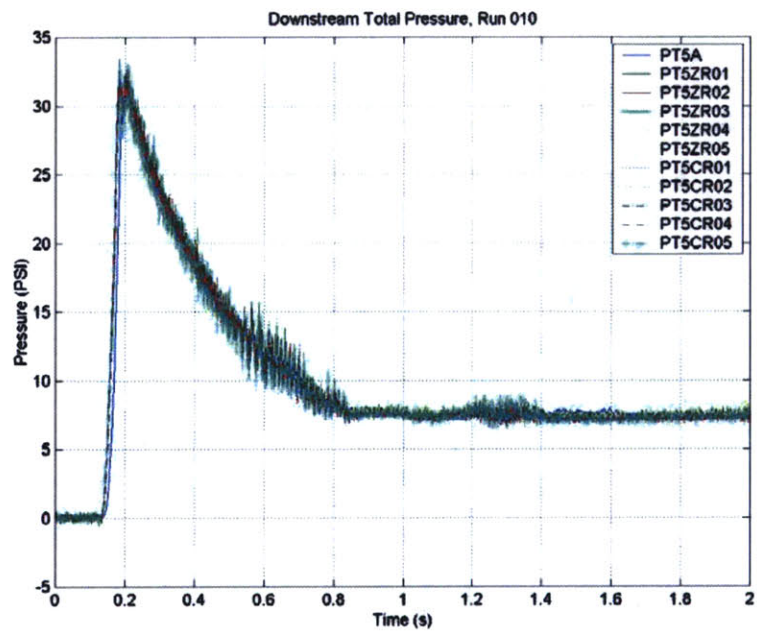


Figure 6.11 – Downstream Total Pressure Rake Measurements for Run 010.

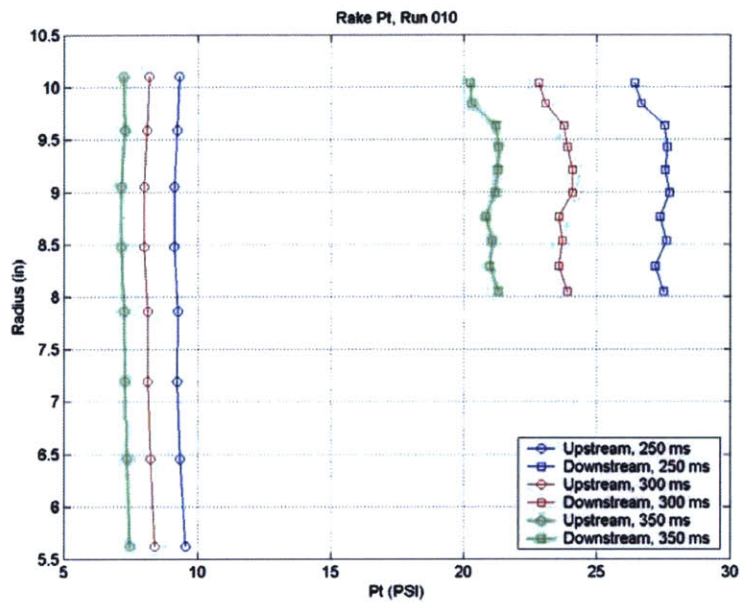


Figure 6.12 - Upstream and Downstream Radial Total Pressure Distribution at 250 ms, 300 ms and 350 ms for Run 010.

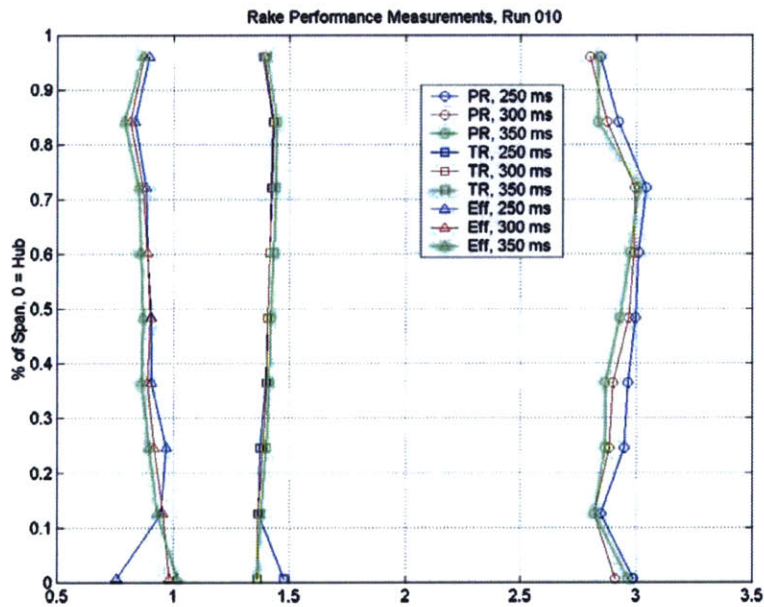


Figure 6.13 - Pressure Ratio, Temperature Ratio and Efficiency Radial Distributions at 250 ms, 300 ms and 350 ms for Run 010.

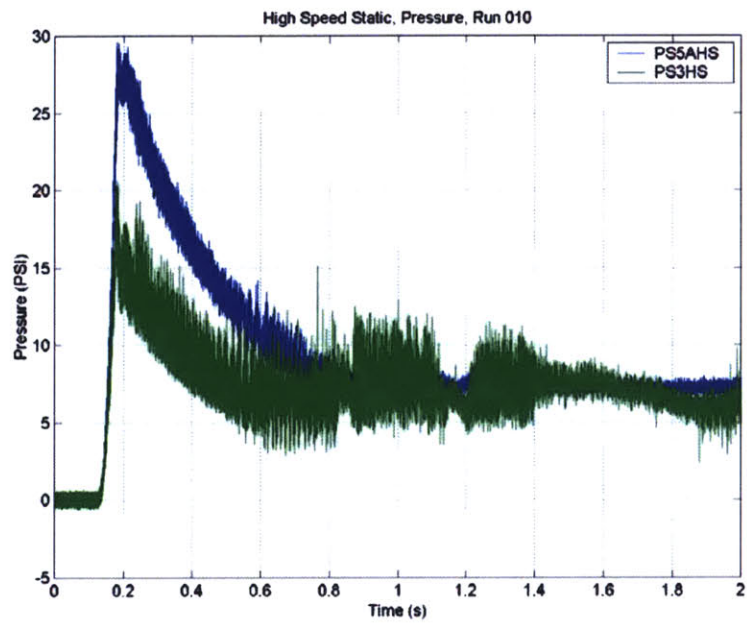


Figure 6.14 – High Speed Static Pressures Behind Rotor 1 (Blue) and Rotor 2 (Green) for Run 010.

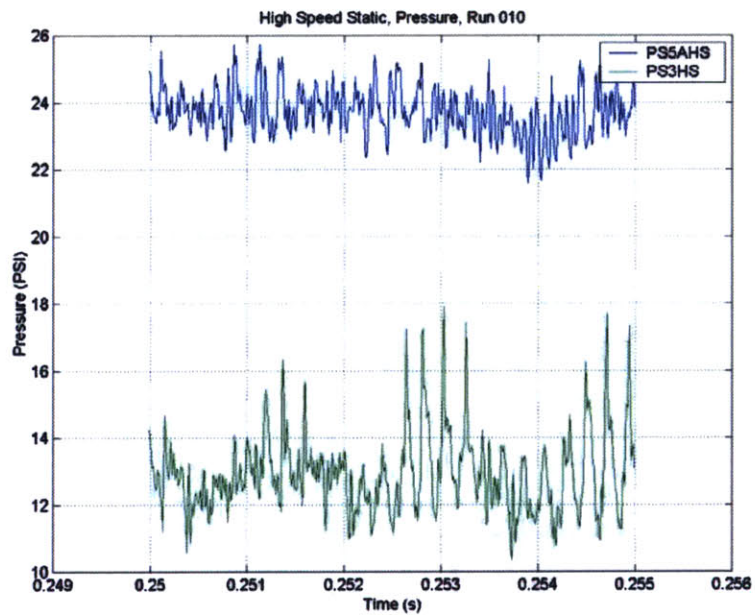


Figure 6.15 - High Speed Static Pressures Behind Rotor 1 (Blue) and Rotor 2 (Green) for Run 010 between 250 ms and 255 ms.

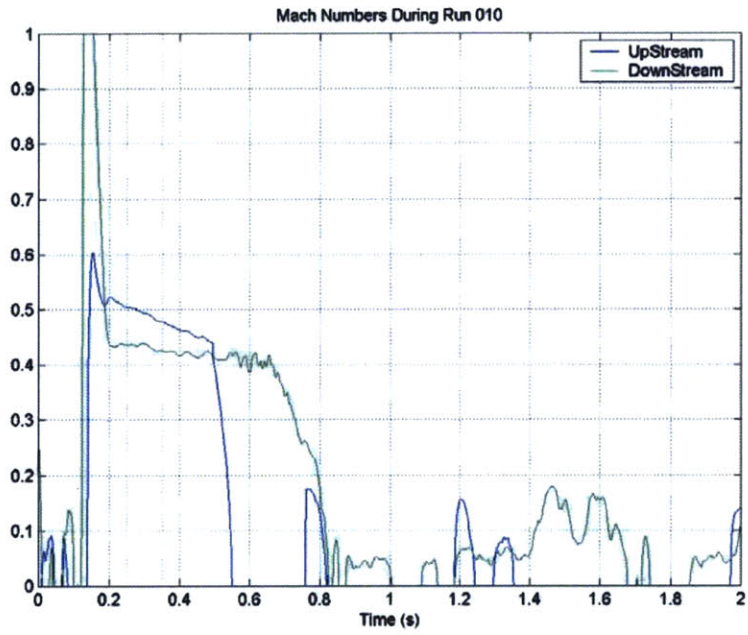


Figure 6.16 – Upstream and Downstream Mach Numbers for Run 010.

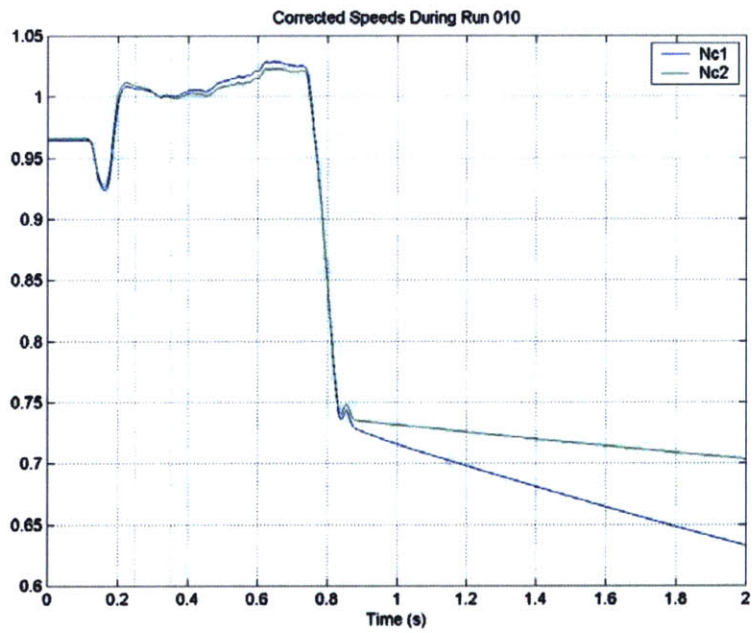


Figure 6.17 – Rotor 1 and 2 Normalized Corrected Speeds for Run 010.

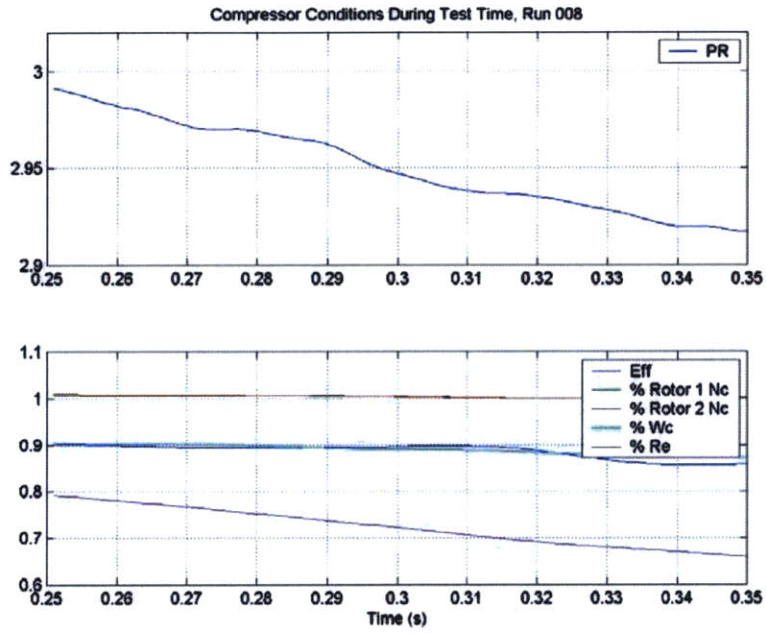


Figure 6.18 – Compressor Conditions During Test Time for Run 010.

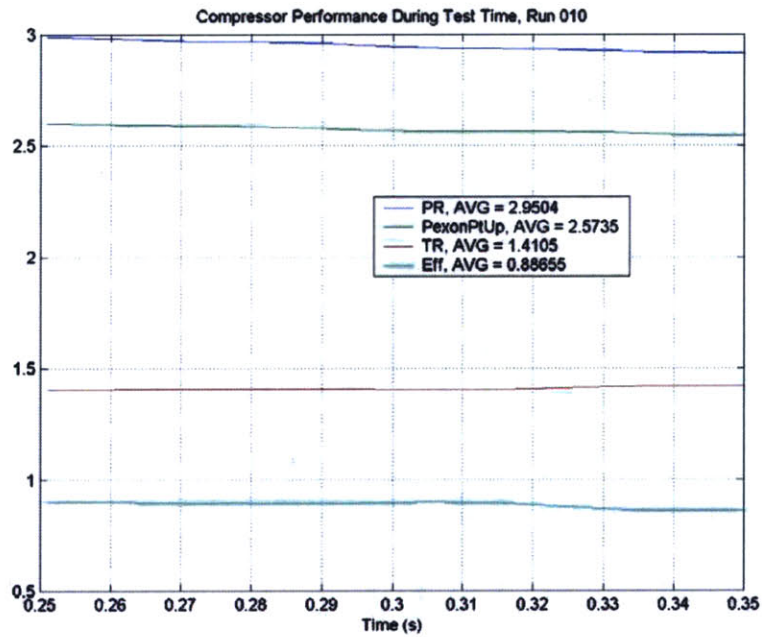


Figure 6.19 – Compressor Performance During Test Time for Run 010.

	<b>RUN ID</b>	<b>005</b>	<b>006</b>	<b>007</b>	<b>008</b>	<b>009</b>	<b>010</b>	<b>011</b>	<b>013</b>	<b>014</b>
<b>Initial Conditions</b>	<b>Tank Pressure (PSI)</b>	30.05	30.13	30.24	34.86	29.82	24.21	23.95	24.21	24.19
	<b>R1 Speed (Hz)</b>	198.44	198.45	198.35	209.54	220.04	219.25	219.42	220.26	220.15
	<b>setting</b>	198.7	198.7	198.7	209.8	220.4	220.4	220.4	220.4	220.4
	<b>R2 Speed (Hz)</b>	151.14	153.03	155.91	164.53	183.82	174.08	174.22	174.35	174.38
	<b>setting</b>	151.3	153.2	156	164.8	184	174.6	174.6	174.6	174.6
	<b>Throttle (in<sup>2</sup>)</b>	98.15	88.88	82.44	82.44	82.44	82.44	78.44	86.58	90.68
<b>At 260 ms</b>	<b>Rotor 1 NC</b>	0.903	0.901	0.904	0.938	1.000	1.007	1.006	1.016	1.018
	<b>Rotor 2 NC</b>	0.886	0.89	0.903	0.934	1.054	1.009	1.008	1.017	1.022
	<b>Wc/WcDes</b>	0.825	0.822	0.812	0.845	0.938	0.94	0.886	0.994	1.016
	<b>Entrance Mach</b>	0.446	0.444	0.437	0.46	0.532	0.534	0.49	0.582	0.603
	<b>PR</b>	1.997	2.119	2.329	2.511	3.017	2.934	2.928	2.928	2.849
	<b>TR</b>	1.264	1.286	1.314	1.351	1.414	1.403	1.417	1.395	1.377
	<b>Eff</b>	0.81	0.826	0.863	0.857	0.885	0.879	0.849	0.906	0.9
	<b>Inlet Gamma</b>	1.426	1.426	1.427	1.428	1.428	1.428	1.427	1.429	1.431
	<b>Exit Gamma</b>	1.396	1.394	1.391	1.388	1.382	1.382	1.381	1.383	1.384
	<b>Eff Throt Area (in<sup>2</sup>)</b>	98.15	88.88	82.44	82.44	82.44	82.44	78.435	86.58	90.675
	<b>Discharge Coef</b>	0.981	1.026	1.007	0.979	0.911	0.938	0.943	0.966	0.967

Table 6.1. - Compressor Initial Operating Conditions, Performances and State at 250 ms for Runs 005 to 014.

### 6.2.3. Preliminary Compressor Map

As explained previously, the compressor operates quasi-steadily between 250 ms and 300 ms. Over this period of time, the corrected speeds of the two rotors are maintained constant to 1%. Data have shown that the inlet corrected mass-flow, which was originally meant to remain constant during the quasi-steady phase, decreases by 3% to 4% over the same range. Thanks to these aspects, a preliminary compressor map can be drawn for each of the test runs, by plotting the compressor pressure ratio versus the normalized inlet corrected mass-flow for constant corrected speed lines. The results encompassing runs 005 to 014 is presented in Figure 6.20. The main particularity of this map is that for each speed line, the pressure ratio of the machine increases with the inlet corrected flow. The operating conditions have not allowed to record the steep drop in pressure ratio as the corrected flow starts significantly overcoming the design inlet corrected flow value. We should mention that this trend was not scheduled by the CFD calculations, which prediction for the design speed line is presented in superposition Figure 6.20. More information can be found in [16] and [17].

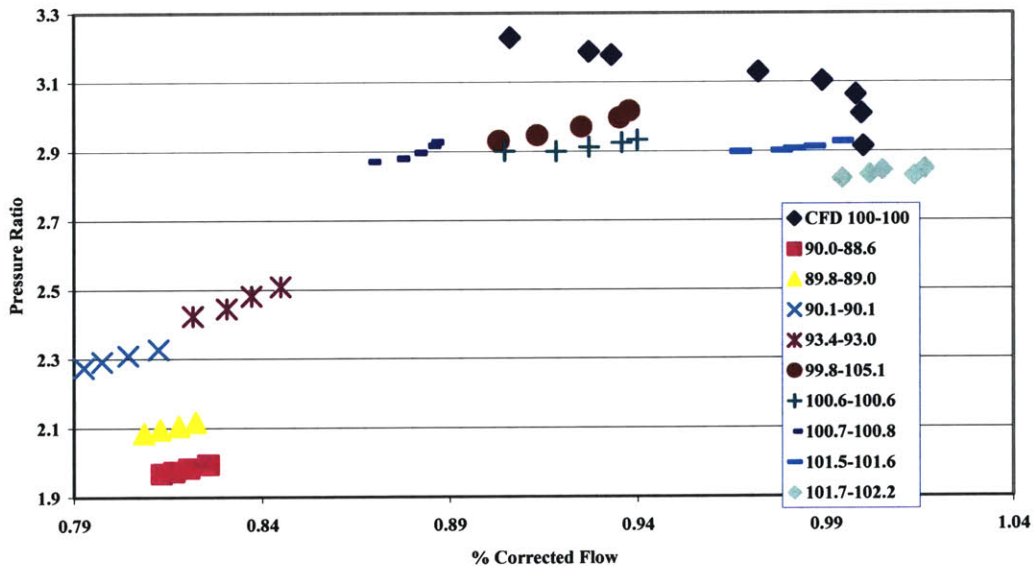


Figure 6.20 – Preliminary Counter-Rotating Aspirated Compressor Map for Corrected Speeds Between 88% and 102% Compared to CFD Full-Speed Line Predictions.

## **7. Conclusion**

### ***7.1. Summary***

In order to measure the aerodynamic performances of a counter-rotating aspirated compressor in a short duration facility, total temperature and pressure measurement probes have been designed.

The total temperature measurement sensors have been manufactured using 0.0005-inch diameter type-K thermocouple gage wires, hung across the inner diameter of the probe head. An infinite cylinder transient conduction-convection heat transfer model was used to predict the response time. The model showed that it takes 30 ms for the upstream probes and 19 ms for the downstream probes to read the fluid temperatures in the facility, which satisfies the response-time problem for transient testing conditions. These thermocouples were inserted in single measurement probes, with a ¼-inch casing diameter, as well as in radial measurement probes, with a 3/16-inch casing diameter, mounted on airfoil-shaped rakes. Thanks to extensive procedures, their calibration errors was contained to less than 0.1 K. Vent holes were designed in the casings of these heads to optimize the tradeoff between the response time of the sensors, the recovery error associated to the non-isentropic stagnation of the flow by the probes and the mechanical resistance of the thermocouple wires to the flow's dynamic pressure. The conduction

error of the sensors was reduced to a minimum of 0.073 K for the upstream rake probes, 0.014 K for the downstream rake probes, 0.005 K for the upstream single probes and 0.0005 K for the downstream single probes, thanks to larger casing diameters. The radiation error appeared to be the black sheep in the error analysis of the temperature probes. Due to the short duration of the test, the probe casings behave quasi-isothermally while the thermocouple wires is following the flow temperature. Consequently, the radiation error averaged 0.112 K for the upstream probes and 0.299 K for the downstream probes. The overall uncertainties of the temperature probes for this project amounted to an average of 0.14 K for the upstream probes and 0.30K for the downstream probes.

The pressure measurements were performed using mainly ultraminiature Kulite piezoresistive strain gauge differential transducers. This type of transducer has very high frequency response. These sensors show scale non-linearities as well as zero drifts, which require several in situ calibrations of each transducer. This helped bring down the corresponding relative probe error to 0.15%, which is on the order of the error imposed by the geometry of the sensing tubes on which the transducers were mounted. Signal noise remains the main error source for the pressure probes. The corresponding average relative error is equal to 0.30%, which is twice as much as the transducer error alone. Overall, the relative pressure measurement error amounted to 0.30% to 0.40%.

These errors have been compiled to compute the uncertainty in the efficiency measurement. Two methods were presented, one consisting in perturbing the inputs of the data reduction programs and recording the amount of change obtained in the efficiency, the other consisting in considering the test rig as an adiabatic compressor operating with an ideal gas at constant mass-flow and specific heat ratio, and deriving an analytical equation of the efficiency uncertainty. The first method gave much better results, forecasting an uncertainty of 0.131 points of efficiency, compared to 0.500 to 0.900 points of efficiency for the approximated model. The errors related to the discrete time and spatial samplings of the flow have been addressed. While the time treatment of the signal settled the first concern, the inlet pressure distortion entailed an uncertainty of 0.95% on the efficiency, due to the discrete spatial repartition of the measurement probes. The impact of the non-adiabatic effects of the short-duration testing environment have

also been estimated. The correction between the efficiency computed from direct measurements on the test rig and the corresponding adiabatic efficiency is proportional to the amount of heat transferred between the fluid and the facility walls, scaled by the temperature ratio of the compressor. Calculations showed that this correction term is smaller than 0.1 point of efficiency. The behavior of each probe and the results of the data reduction process during Run 010 have been presented. A preliminary compressor has been established and compared to the CFD predictions. The positive slopes of the empirical speed lines are a peculiar feature of this compressor.

## ***7.2. Future Work***

Many thrilling challenges remain in the measurement of the aerodynamic performances of the blow-down counter-rotating aspirated compressor.

A first group of challenges are linked to the performances of the measurement probes themselves. While all other errors have been brought to a minimum level, the thermocouple probes are submitted to a persisting radiation error, linked to the constant temperature of the head casings. Further study must be undertaken to allow the casings' temperature to better follow the flow temperature. As for the pressure transducers, the noise error can be reduced to the same level as the other sources by improving the electrical installation of the facility.

The second group concerns the facility. The operation of the tunnel has shown an inlet pressure distortion, which could be due to imperfections in the inlet pressure screen [2]. This phenomenon requires further studies. More instrumentation is needed in the bleed flow passage, to better assess the change in mass-flow over the test time. The preliminary compressor map has also unveiled an unexpected feature, namely that the pressure ratio grows with the corrected mass-flow. More instrumentation might help clear this point and better understand the way a blow-down counter-rotating aspirated compressor operates.



**8. Appendix A: Detailed Calculation of the Correction Between Indicated and Adiabatic Efficiencies in a Blow-Down Test Facility.**

GOAL: We want to determine the evolution of the blade temperature during a one second test.

Method: We compute the heat flux in each rotor and plot the corresponding response of the blade temperature

Blade thermal properties:

	<u>Rotor 1 (17-4PH)</u>	<u>Rotor 2 (Al 2046)</u>
Thermal diffusivity:	$\alpha_1 := 5.1 \cdot 10^{-6} \cdot \frac{\text{m}^2}{\text{s}}$	$\alpha_2 := 73 \cdot 10^{-6} \cdot \frac{\text{m}^2}{\text{s}}$
Thermal conductivity:	$k_1 := 18.3 \cdot \frac{\text{W}}{\text{m} \cdot \text{K}}$	$k_2 := 177 \cdot \frac{\text{W}}{\text{m} \cdot \text{K}}$
Density:	$\rho_1 := 7800 \text{kg} \cdot \text{m}^{-3}$	$\rho_2 := 2770 \text{kg} \cdot \text{m}^{-3}$
Heat coefficient	$c_1 := 460 \text{J} \cdot \text{K}^{-1} \cdot \text{kg}^{-1}$	$c_2 := 875 \text{J} \cdot \text{K}^{-1} \cdot \text{kg}^{-1}$
Initial temperature: $T_0 = 300\text{K}$		

Gas properties:

$$C_p := 691.5 \cdot \text{J} \cdot \text{kg}^{-1} \cdot \text{K}^{-1}$$

$$\gamma := 1.402$$

$$R_g := 198.276 \cdot \text{kg}^{-1} \cdot \text{K}^{-1}$$

Flow characteristics:

Before Rotor 1	Absolute Inlet Mach	$M_0 = 0.65$
	Number	
	Total Inlet Temperature	$T_{t0} = 300\text{K}$
	Total Inlet Pressure	$P_{t0} = 83789\text{Pa}$
Rotor 1	Relative Inlet Mach number	$M_{0b} = 1.27$
	Relative outlet Mach	$M_{1b} = .69$
	Number	
Rotor 2	Relative Inlet Mach number	$M_{2b} = 1.33$
	Relative Outlet Mach	$M_{3b} = 0.73$
	number	

These conditions change with time according to the blowdown time constant and model:

$$\tau_{bd} := 2.373 \cdot s$$

$$T_{t0}(t) := T_0 \cdot \frac{1}{\left(1 + \frac{t}{\tau_{bd}}\right)^2} \quad (A.1)$$

$$p_{t0}(t) := p_{t00} \cdot \left(1 + \frac{t}{\tau_{bd}}\right)^{\frac{-2\gamma}{\gamma-1}} \quad (A.2)$$

**Assumptions:**

Computation is done assuming unsteady inlet conditions at rotor 1. At each time  $t$ , we are able to determine the heat flux imposed by the airflow to the blades of the compressor, this assuming that there is no delay in the propagation of the information about the changes in the inlet conditions of rotor 1.

The adiabatic recovery coefficient is computed in the case of a turbulent boundary layer.

The static temperature of the gas is supposed to remain constant between the 2 rotors.

Critical assumption: The Prandtl number is assumed to be 0.774.

The temperature evolution in the blade is computed assuming the blades are semi-infinite solids submitted to a time variable surface heat flux. Then the blades are supposed to be isothermal in the thickness direction.

We assume for the test that the gas mixture we use has a Prandtl number of  $Pr = 0.774$

We also know the friction coefficient of the each blade, from the flow path computation.

$$\text{For rotor 1: } C_{f1} = 0.002$$

$$\text{For rotor 2: } C_{f2} = 0.0013$$

Then, according [21], in a turbulent boundary layer, the Stanton number is:

$$St_1 := \frac{\frac{C_{f1}}{2}}{1 + 13 \cdot \left(\frac{2}{Pr^3} - 1\right) \cdot \sqrt{\frac{C_{f1}}{2}}} \quad (A.4)$$

$$St_2 := \frac{\frac{C_{f2}}{2}}{1 + 13 \cdot \left(\frac{2}{Pr^3} - 1\right) \cdot \sqrt{\frac{C_{f2}}{2}}} \quad (A.5)$$

We can compute the turbulent recovery coefficient:

The turbulent Prandtl number is  $Pr_t = 0.9$

Hence, according to[21]:

$$r := Prt + (Pr - Prt) \cdot \left( \frac{11.5}{20} \right)^2 \quad (\text{A.6})$$

$$r = 0.858$$

Computation:

- At the inlet of rotor 1:

$$\rho a_0(t) := \frac{p_{t0}(t)}{R_g \cdot T_{t0}(t)} \cdot \left[ 1 + \frac{(\gamma - 1) \cdot M_0^2}{2} \right]^{\frac{1}{1-\gamma}} \quad (\text{A.7})$$

$$T_{s0}(t) := \frac{T_{t0}(t)}{1 + \frac{(\gamma - 1) \cdot M_0^2}{2}} \quad (\text{A.8})$$

$$a_0(t) := \sqrt{\gamma \cdot R_g \cdot T_{s0}(t)} \quad (\text{A.9})$$

$$T_{t0b}(t) := T_{s0}(t) \cdot \left( 1 + \frac{\gamma - 1}{2} \cdot M_{0b}^2 \right) \quad (\text{A.10})$$

$$q_{s0}(t) := -St_1 \cdot \rho a_0(t) \cdot C_p \cdot \left( T_{t0b}(t) \cdot \frac{1 + r \cdot \frac{\gamma - 1}{2} \cdot M_{0b}^2}{1 + \frac{\gamma - 1}{2} \cdot M_{0b}^2} - T_0 \right) \cdot M_{0b} \cdot a_0(t) \quad (\text{A.11})$$

- At the outlet of rotor 1:

The total temperature inside the blade remains constant from the rotating frame point of view.

$$Tt1b(t) := Tt0b(t) \quad (\text{A.12})$$

$$Ts1(t) := \frac{Tt1b(t)}{1 + \frac{(\gamma - 1) \cdot M1b^2}{2}} \quad (\text{A.13})$$

$$Pt0b(t) := \frac{pt0(t)}{\frac{\gamma}{\left[1 + \frac{(\gamma - 1) \cdot M0^2}{2}\right]^{\gamma-1}}} \cdot \left[1 + \frac{(\gamma - 1) \cdot M0b^2}{2}\right]^{\frac{\gamma}{\gamma-1}} \quad (\text{A.14})$$

$$Pt1b(t) := Pt0b(t) \quad (\text{A.15})$$

$$\rho a1(t) := \frac{Pt1b(t)}{\frac{\gamma}{\left[1 + \frac{(\gamma - 1) \cdot M1b^2}{2}\right]^{\gamma-1}}} \cdot \frac{1}{Rg \cdot Ts1(t)} \quad (\text{A.16})$$

$$a1(t) := \sqrt{\gamma \cdot Rg \cdot Ts1(t)} \quad (\text{A.17})$$

$$qs1(t) := -St1 \cdot \rho a1(t) \cdot Cp \cdot \left( Tt1b(t) \cdot \frac{1 + r \cdot \frac{\gamma - 1}{2} \cdot M1b^2}{1 + \frac{\gamma - 1}{2} \cdot M1b^2} - T0 \right) \cdot M1b \cdot a1(t) \quad (\text{A.18})$$

- At the inlet of rotor 2: we assume that the static temperature is not changed between the outlet of rotor 1 and the inlet of rotor 2.

$$Tt3b := Tt2b \quad (\text{A.19})$$

$$Tt2b(t) := Ts2(t) \cdot \left( 1 + \frac{\gamma - 1}{2} \cdot M2b^2 \right) \quad (\text{A.20})$$

$$\rho a2(t) := \rho a1(t) \quad (\text{A.21})$$

$$a2(t) := \sqrt{\gamma \cdot Rg \cdot Ts2(t)} \quad (\text{A.22})$$

$$qs2(t) := -St2 \cdot \rho a2(t) \cdot Cp \cdot \left( Tt2b(t) \cdot \frac{1 + r \cdot \frac{\gamma - 1}{2} \cdot M2b^2}{1 + \frac{\gamma - 1}{2} \cdot M2b^2} - T0 \right) \cdot M2b \cdot a2(t) \quad (\text{A.23})$$

- At the outlet of rotor 2:

$$Tt3b := Tt2b \quad (\text{A.24})$$

$$Pt3b(t) := \frac{Pt1b(t)}{\frac{\gamma}{\left[ 1 + \frac{(\gamma - 1) \cdot M1b^2}{2} \right]^{\gamma - 1}}} \cdot \left[ 1 + \frac{(\gamma - 1) \cdot M2b^2}{2} \right]^{\frac{\gamma}{\gamma - 1}} \quad (\text{A.25})$$

$$\rho a3(t) := \frac{Pt3b(t)}{\frac{\gamma}{\left[ 1 + \frac{(\gamma - 1) \cdot M3b^2}{2} \right]^{\gamma - 1}}} \cdot \frac{1}{Rg \cdot \frac{Tt3b(t)}{1 + \frac{(\gamma - 1) \cdot M3b^2}{2}}} \quad (\text{A.26})$$

$$Ts3(t) := \frac{Tt3b(t)}{1 + \frac{(\gamma - 1) \cdot M3b^2}{2}} \quad (\text{A.27})$$

$$a3(t) := \sqrt{\gamma \cdot Rg \cdot Ts3(t)} \quad (\text{A.28})$$

$$qs3(t) := -St2 \cdot \rho a3(t) \cdot Cp \cdot \left( Tt3b(t) \cdot \frac{1 + r \cdot \frac{\gamma - 1}{2} \cdot M3b^2}{1 + \frac{\gamma - 1}{2} \cdot M3b^2} - T0 \right) \cdot M3b \cdot a3(t) \quad (\text{A.29})$$

According to [22], the leading edges temperatures for each rotor are given by:

$$Te1(\eta, t) := T0 + \frac{\sqrt{\alpha1}}{k1 \cdot \sqrt{\pi}} \cdot \int_0^t -qs0(t - \tau) \cdot e^{-\eta^2} \cdot \frac{1}{\sqrt{\tau}} d\tau \quad (A.30)$$

$$Te2(\eta, t) := T0 + \frac{\sqrt{\alpha2}}{k2 \cdot \sqrt{\pi}} \cdot \int_0^t -qs2(t - \tau) \cdot e^{-\eta^2} \cdot \frac{1}{\sqrt{\tau}} d\tau \quad (A.31)$$

$$x1(\eta, t) := \eta \cdot 2 \cdot \sqrt{\alpha1 \cdot t}$$

$$x2(\eta, t) := \eta \cdot 2 \cdot \sqrt{\alpha2 \cdot t}$$

$$x1(2, 1s) = 9.033 \times 10^{-3} \text{ m}$$

$$x2(2, 1s) = 0.034 \text{ m}$$

$$x1(2, 0.5 \cdot s) = 6.387 \times 10^{-3} \text{ m}$$

$$x2(2, 0.5 \cdot s) = 0.024 \text{ m}$$

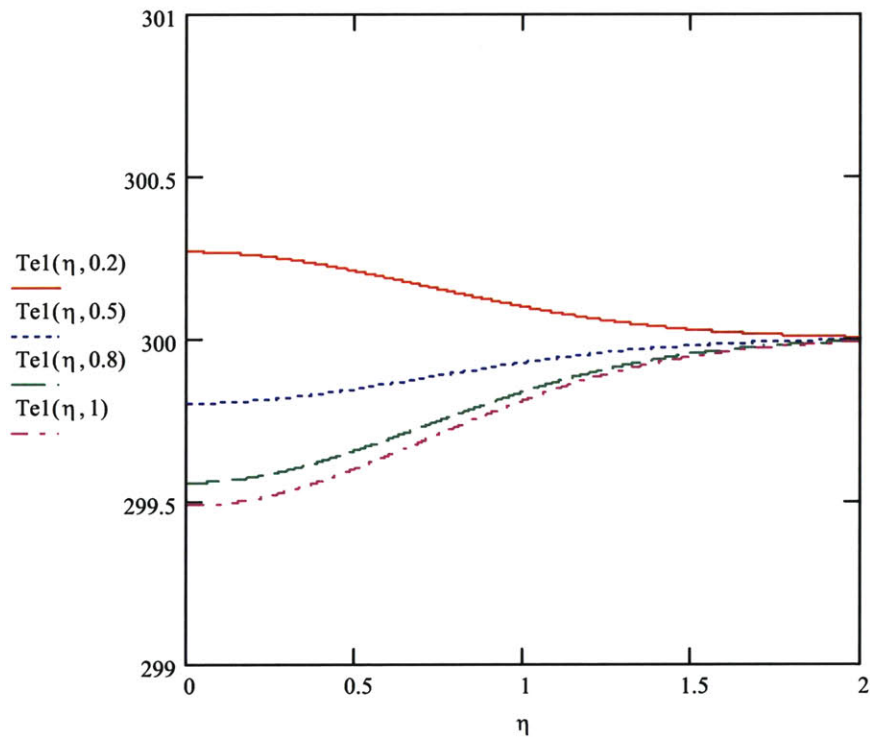


Figure A.1. - Temperature Profile vs. η Inside Rotor 1 at Various Time Points.

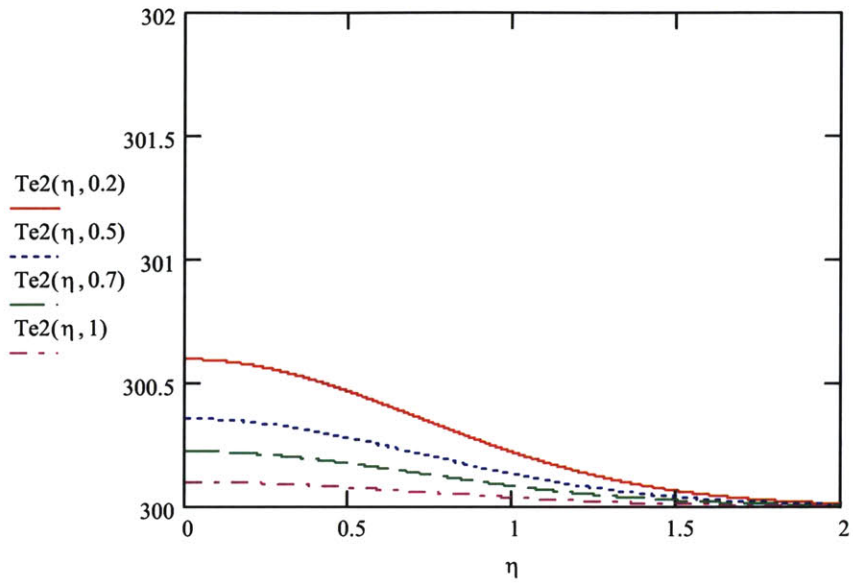


Figure A.2. - Temperature Profile vs.  $\eta$  Inside Rotor 2 at Various Time Points.

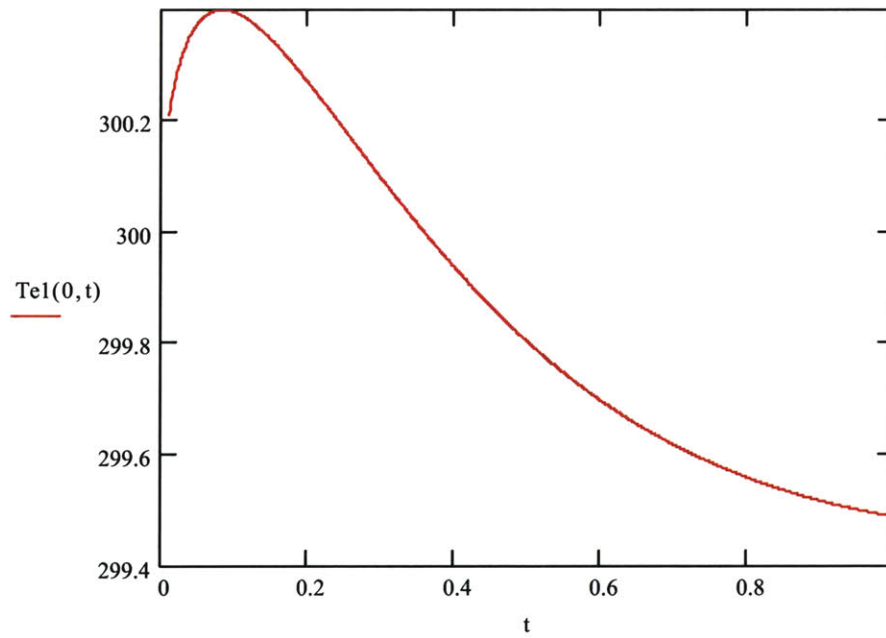


Figure A.3. - Temperature Evolution at the Surface of the Leading Edge of Rotor 1 over 1s

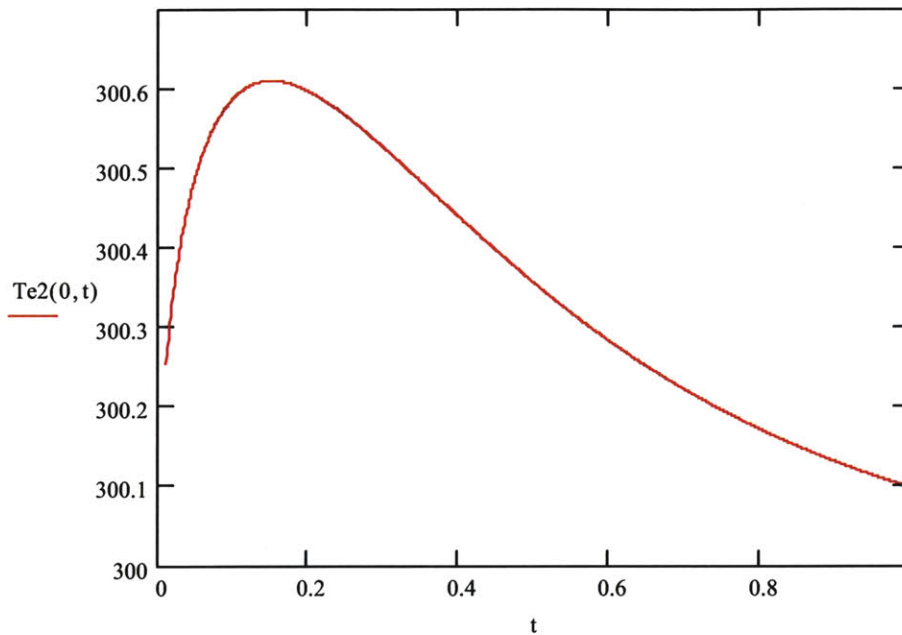


Figure A.4. - Temperature Evolution at the Surface of the Leading Edge of Rotor 2 over 1s.

The non-dimensional length of this problem seems relatively large compared to the thickness of the blades. Over 1 second, the length beyond which the blade is not affected by the temperature change is:

For rotor 1  $x_{l(2, 1s)} = 9.033 \times 10^{-3} \text{ m}$

For rotor 2  $x_{\lambda(2, 1s)} = 0.034 \text{ m}$

We shall notice here that the heat flux has been calculated assuming the blade temperature to be constant, and from this result the corresponding temperature evolution of the blade temperature has been plotted. The small variation observed show the consistency of the way we proceeded, although this model does not represent correctly what happens in the blades.

We might have to consider the lumped thermal capacity model. We can compute the Biot number for each stage:

For rotor 1:

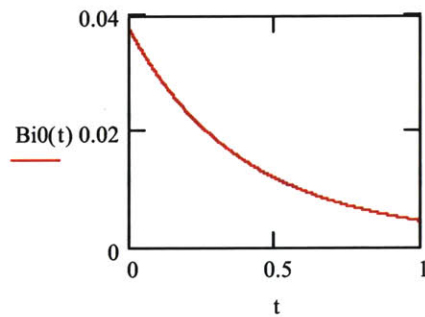
$$hc0(t) := St1 \cdot \rho a0(t) \cdot Cp \cdot M0b \cdot a0(t) \quad (A.32)$$

$$hc1(t) := St1 \cdot \rho a1(t) \cdot Cp \cdot M1b \cdot a1(t) \quad (A.33)$$

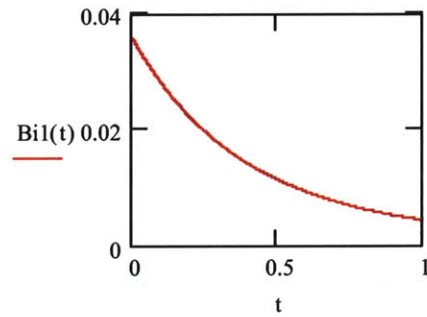
$$L1 = 0.0023m$$

$$Bi0(t) := \frac{hc0(t) \cdot L1}{k1} \quad (A.34)$$

$$Bi1(t) := \frac{hc1(t) \cdot L1}{k1} \quad (A.35)$$



(a)



(b)

Figure A.5. – Biot Number at Leading Edge (a) and Trailing Edge (b) of Rotor 1 over 1s.

For rotor 2:

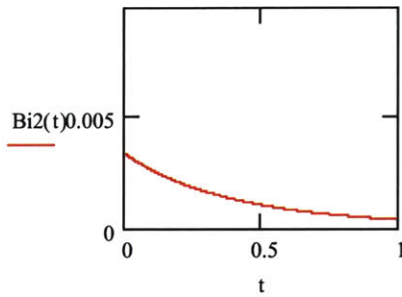
$$hc2(t) := St2 \cdot \rho a2(t) \cdot Cp \cdot M2b \cdot a2(t) \quad (A.36)$$

$$hc3(t) := St2 \cdot \rho a3(t) \cdot Cp \cdot M3b \cdot a3(t) \quad (A.37)$$

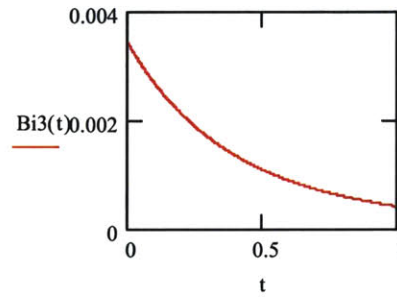
$$L2 = 0.0017m$$

$$Bi2(t) := \frac{hc2(t) \cdot L2}{k2} \quad (A.37)$$

$$Bi3(t) := \frac{hc3(t) \cdot L2}{k2} \quad (A.38)$$



(a)



(b)

Figure A.6. - Biot Number at Leading Edge (a) and Trailing Edge (b) of Rotor 2 over 1s.

We get Biot numbers on the order of 0.1, which justifies the use of the lumped capacity models.

Cross section surface areas:

For the IGV

$$AcIGV := 0.067 \cdot \text{in}^2$$

For rotor 1

$$Ac1 := 0.54 \text{in}^2$$

For rotor 2

$$Ac2 := 0.28 \text{in}^2$$

We can estimate the surface area of the blades, from the cross section view, assuming the blades to be trapezoidal and dividing the measures by the cosine of the average relative angle.

For the IGV  $A_{IGV} := (0.0055\text{m} \cdot 5 \cdot 0.026 \cdot \text{m} \cdot 5)$   $A_{IGV} = 3.575 \times 10^{-3} \text{m}^2$

For rotor 1  $A_1 := \frac{[(0.026\text{m} + 0.02\text{m}) \cdot 5 \cdot 0.0115\text{m} \cdot 5]}{\cos\left(\frac{60\text{deg} + 46.4\text{deg}}{2}\right)}$   $A_1 = 0.022\text{m}^2$

Foro rotor 2  $A_2 := \frac{[(0.016\text{m} + 0.012\text{m}) \cdot 5 \cdot 0.0075\text{m} \cdot 5]}{\cos\left(\frac{62\text{deg} + 50.3\text{deg}}{2}\right)}$   $A_2 = 9.425 \times 10^{-3} \text{m}^2$

We can also estimate the volume of each blade:

For the IGV  $V_{IGV} := A_{IGV} \cdot 0.026\text{m} \cdot 5$   $V_{IGV} = 5.619 \times 10^{-6} \text{m}^3$

For rotor 1  $V_1 := A_{c1} \cdot \left[0.02\text{m} \cdot 5 + \frac{(0.026\text{m} - 0.02\text{m}) \cdot 5}{2}\right]$   $V_1 = 4.006 \times 10^{-5} \text{m}^3$

For rotor 2  $V_2 := A_{c2} \cdot \left[0.012\text{m} \cdot 5 + \frac{(0.016\text{m} - 0.012\text{m}) \cdot 5}{2}\right]$   $V_2 = 1.265 \times 10^{-5} \text{m}^3$

Let  $T_1$  be the temperature of the blades of rotor 1 and  $T_2$  the temperature of the blades of rotor 2, in this lump thermal capacity model. For each rotor, we can compute the evolution of the temperature using the heat transfer computed at the leading edge or at the trailing edge of the blade. Letter 'l' will refer to the temperature at the leading edge and letter 't' to that at the trailing edge.

$T_{1l}$  must satisfy the following differential equation:

$$\frac{d}{dt} T = -hc_0(t) \cdot \frac{\frac{A_1}{2}}{\left(\rho_1 \cdot c_1 \cdot \frac{V_1}{2}\right)} \cdot T(t) + hc_0(t) \cdot \frac{\frac{A_1}{2}}{\left(\rho_1 \cdot c_1 \cdot \frac{V_1}{2}\right)} \cdot T_{t0b}(t) \cdot \frac{1 + r \cdot \frac{\gamma - 1}{2} \cdot M_{0b}^2}{1 + \frac{\gamma - 1}{2} \cdot M_{0b}^2} \quad (\text{A.39})$$

Using the constant variation method, we are able to compute the solution:

$$\lambda_{11}(t) := 1 + \frac{\int_0^t hc_0(u) \cdot \frac{A_1}{2} \cdot T_{t0b}(u) \cdot \frac{1 + r \cdot \frac{\gamma - 1}{2} \cdot M_{0b}^2}{1 + \frac{\gamma - 1}{2} \cdot M_{0b}^2} du}{\rho_1 \cdot \frac{V_1}{2} \cdot c_1 \cdot T_0 \cdot e^{\int_0^u \frac{-A_1}{\rho_1 \cdot \frac{V_1}{2} \cdot c_1} hc_0(\tau) d\tau}} \quad (\text{A.40})$$

$$T_{11}(t) := \lambda_{11}(t) \cdot T_0 \cdot e^{\int_0^t \frac{-A_1}{\rho_1 \cdot \frac{V_1}{2} \cdot c_1} hc_0(\tau) d\tau} \quad (\text{A.41})$$

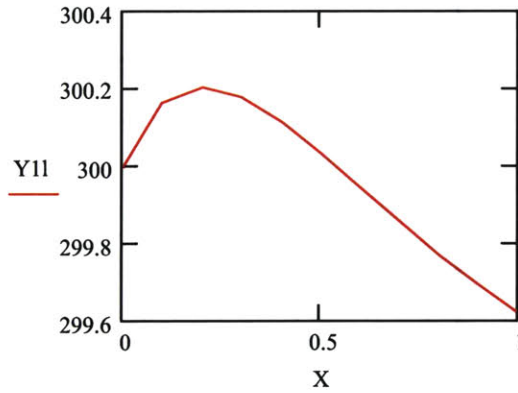


Figure A.7. – Temperature Evolution at the Surface of the Leading Edge of Rotor 1 Over 1s.

Similarly, at the trailing edge of rotor 1:

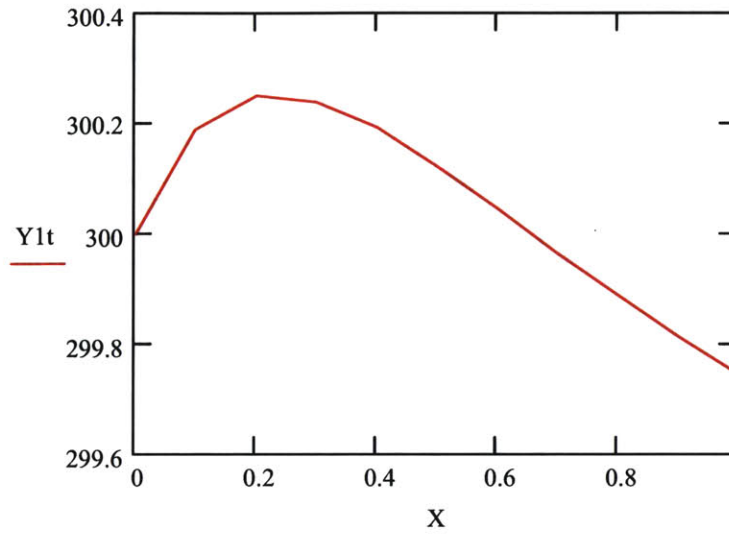


Figure A.8. - Temperature Evolution at the Surface of the Trailing Edge of Rotor 1 Over 1s.

At the leading edge of rotor 2:

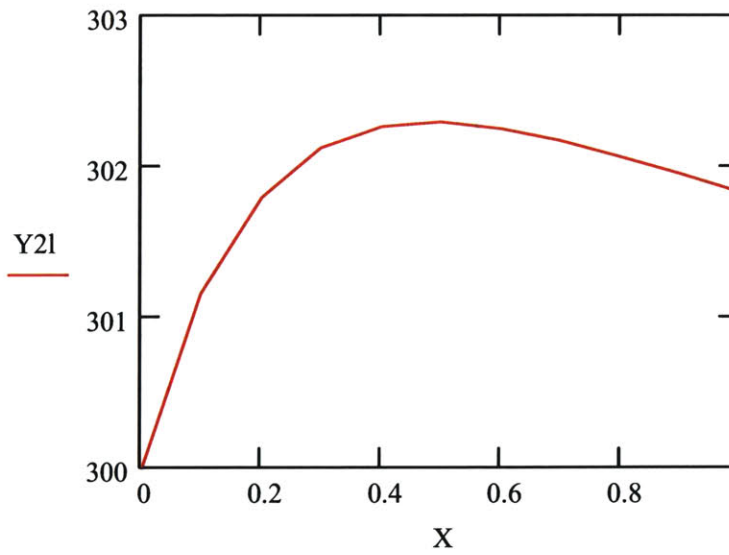


Figure A.9. - Temperature Evolution at the Surface of the Leading Edge of Rotor 2 Over 1s.

At the trailing edge of rotor 2:

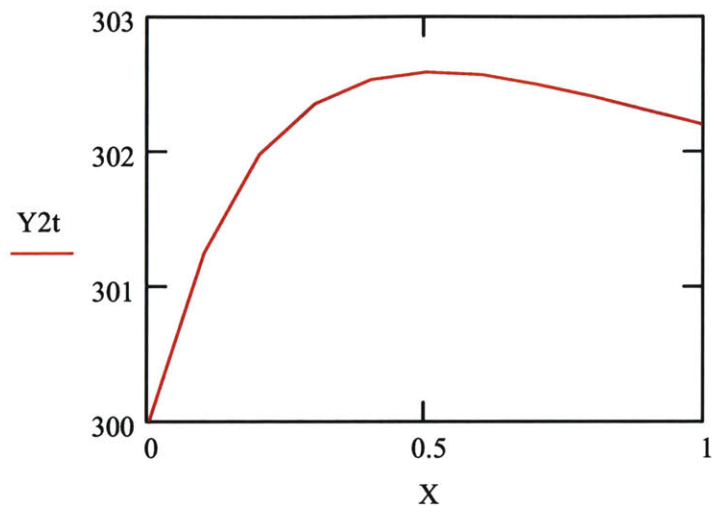


Figure A.10. - Temperature Evolution at the Surface of the Trailing Edge of Rotor 2 Over 1s.

As for the IGV:

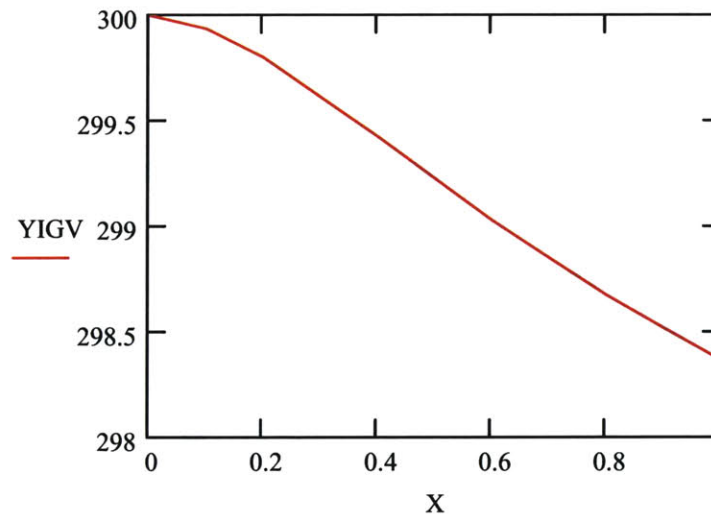


Figure A.11. - Temperature Evolution at the Surface of the IGV Over 1s.

The results concerning the heat transfer at the level of the hub of the rotors are similar to the time unsteady results computed for the blades as semi-infinite bodies. We do not take into account the thermal boundary layer. Rotor 2 hub is however made of steel 17-4PH contrary to the corresponding blades, which are in aluminum.

For rotor 2 hub, the result is:

$$Te3(\eta, t) := T0 + \frac{\sqrt{\alpha}l}{k1 \cdot \sqrt{\pi}} \cdot \int_0^t -qs2(t - \tau) \cdot e^{-\eta^2} \cdot \frac{1}{\sqrt{\tau}} d\tau \quad (A.42)$$

Over the test time, the temperature profiles in the hub for various time dates are:

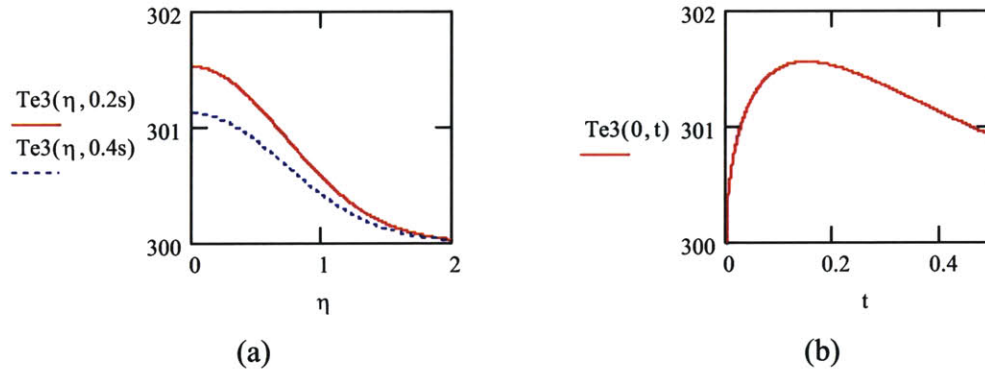


Figure A.12. – Temperature Evolution of Rotor 2 Hub vs. Depth for Different Time Points (a) and vs. Time at the Surface (b).

The walls of the duct are assumed to be made of carbon steel AISI 1010.

Thermal diffusivity

$$\alpha3 := 18.8 \cdot 10^{-6} \cdot \frac{m^2}{s}$$

Density

$$\rho3 := 7830 \frac{kg}{m^3}$$

Constant Heat capacity

$$c3 := 434 \frac{J}{K \cdot kg}$$

Thermal conductivity

$$k3 := \alpha3 \cdot \rho3 \cdot c3$$

$$k3 = 63.887 kg ms^{-3} K^{-1}$$

For the walls that are located in front of rotor 1, the heat transfer flux is

$$q_{s00}(t) := -St_1 \cdot \rho a_0(t) \cdot C_p \cdot \left( Tt_0(t) \cdot \frac{1 + r \cdot \frac{\gamma - 1}{2} \cdot M_0^2}{1 + \frac{\gamma - 1}{2} \cdot M_0^2} - T_0 \right) \cdot M_0 \cdot a_0(t) \quad (A.43)$$

The corresponding temperature is:

$$Te_0(\eta, t) := T_0 + \frac{\sqrt{\alpha_3}}{k_3 \cdot \sqrt{\pi}} \cdot \int_0^t -q_{s00}(t - \tau) \cdot e^{-\eta^2} \cdot \frac{1}{\sqrt{\tau}} d\tau \quad (A.44)$$

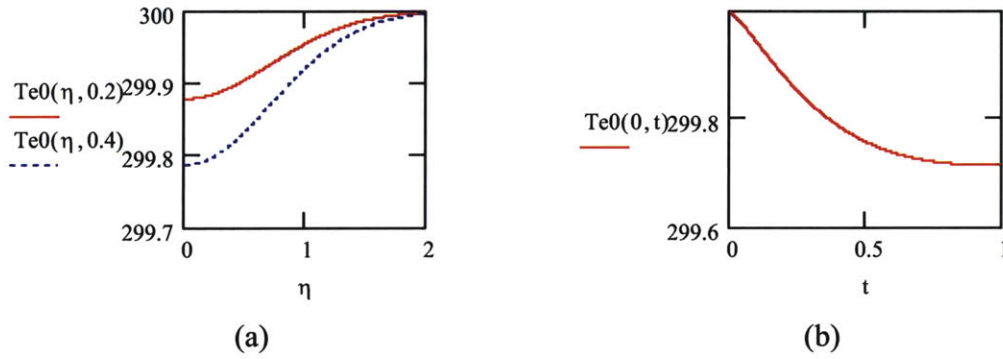


Figure A.13. - Temperature Evolution of Rotor 1 Hub vs. Depth for Different Time Points (a) and vs. Time at the Surface (b).

For the rotor casing:

$$q_{s0e}(t) := -St_1 \cdot \rho a_0(t) \cdot C_p \cdot \left( Tt_0(t) \cdot \frac{1 + r \cdot \frac{\gamma - 1}{2} \cdot M_0^2}{1 + \frac{\gamma - 1}{2} \cdot M_0^2} - T_0 \right) \cdot M_0 \cdot a_0(t) \quad (A.45)$$

$$Te_0(\eta, t) := T_0 + \frac{\sqrt{\alpha_3}}{k_3 \cdot \sqrt{\pi}} \cdot \int_0^t -q_{s0e}(t - \tau) \cdot e^{-\eta^2} \cdot \frac{1}{\sqrt{\tau}} d\tau \quad (A.46)$$

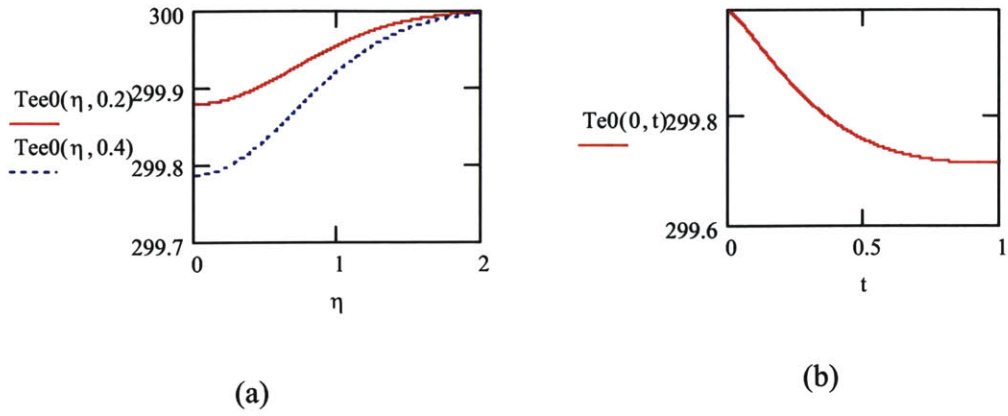


Figure A.14. - Temperature Evolution of the Leading Edge Parts of Rotor 1 Blades vs. Depth for Different Time Points (a) and vs. Time at the Surface (b).

- At station 1:

Let  $M1$  be the total Mach number at mid-span.

$M1x$  – axial Mach number at station 1       $M1x := 0.4\xi$

Rotor 1 tip rotating speed       $Vr1 := 1450 \frac{\text{ft}}{\text{s}}$

Corresponding Mach number       $Mr1(t) := \frac{Vr1}{a1(t)}$

Thus:

$$M1(t) := \sqrt{M1x^2 + \left( Mr1(t) - \sqrt{M1b^2 - M1x^2} \right)^2} \quad (\text{A.47})$$

$$qs1e(t) := -St1 \cdot \rho a1(t) \cdot Cp \cdot \left[ Ts1(t) \cdot \left( 1 + r \cdot \frac{\gamma - 1}{2} \cdot M1(t)^2 \right) - T0 \right] \cdot M1(t) \cdot a1(t) \quad (\text{A.48})$$

$$Teel(\eta, t) := T0 + \frac{\sqrt{\alpha 3}}{k3 \cdot \sqrt{\pi}} \cdot \int_0^t -qs1e(t - \tau) \cdot e^{-\eta^2} \cdot \frac{1}{\sqrt{\tau}} d\tau \quad (\text{A.49})$$

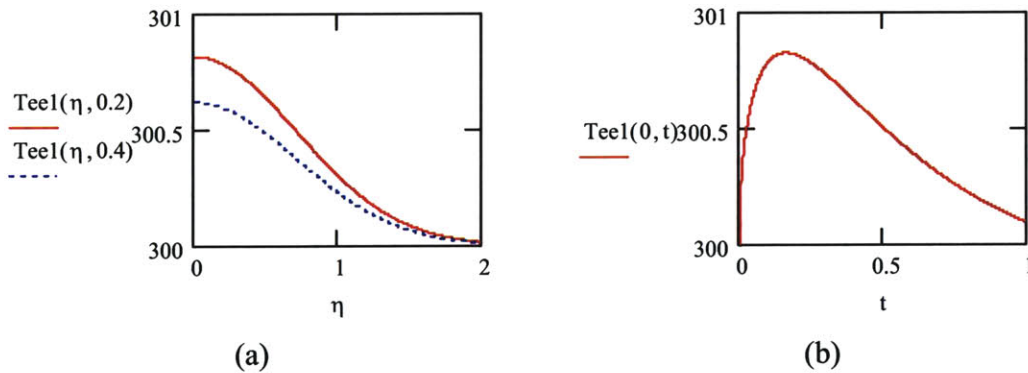


Figure A.15. - Temperature Evolution of the Trailing Edge Parts of Rotor 1 Blades vs. Depth for Different Time Points (a) and vs. Time at the Surface (b).

- At station 2:

Let  $M2$  be the total Mach number at mid-span.

$M2x$  – axial Mach number at station 2       $M2x := 0.63$

Rotor 2 tip rotating speed       $Vr2 := 1100 \frac{\text{ft}}{\text{s}}$

Corresponding Mach number       $Mr2(t) := \frac{Vr2}{a2(t)}$

Thus:

$$M2(t) := \sqrt{M2x^2 + \left( Mr2(t) - \sqrt{M2b^2 - M2x^2} \right)^2} \quad (\text{A.50})$$

$$qs2e(t) := -St2 \cdot \rho a2(t) \cdot Cp \cdot \left[ Ts2(t) \cdot \left( 1 + \frac{\gamma - 1}{2} \cdot r \cdot M2(t)^2 \right) - T0 \right] \cdot M2(t) \cdot a2(t) \quad (\text{A.51})$$

$$Tee2(\eta, t) := T0 + \frac{\sqrt{\alpha 3}}{k3 \cdot \sqrt{\pi}} \cdot \int_0^t -qs2e(t - \tau) \cdot e^{-\eta^2} \cdot \frac{1}{\sqrt{\tau}} d\tau \quad (\text{A.52})$$

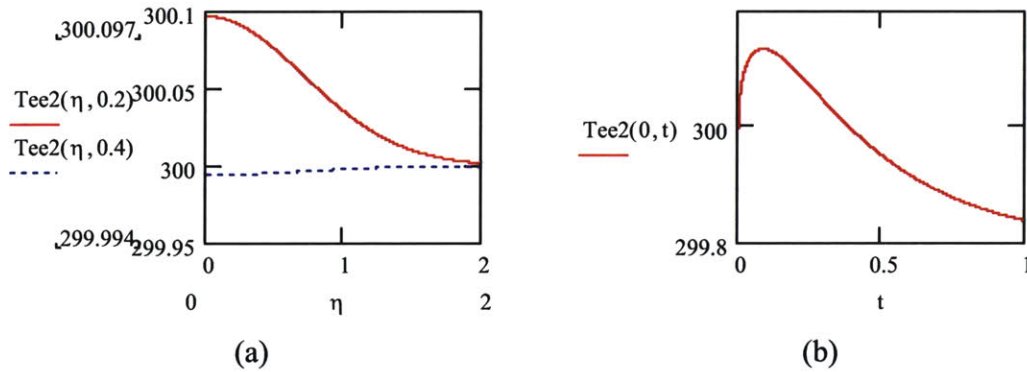


Figure A.16. - Temperature Evolution of the Leading Edge Parts of Rotor 2 Blades vs. Depth for Different Time Points (a) and vs. Time at the Surface (b).

- At station 3:

Let  $M3$  be the total Mach number at mid-span:

$M3x$  – axial Mach number at station 3       $M3x := 0.47$

Corresponding Mach number       $Mr3(t) := \frac{Vr2}{a3(t)}$

Thus:

$$M3(t) := \sqrt{M3x^2 + \left( Mr3(t) - \sqrt{M3b^2 - M3x^2} \right)^2} \quad (A.53)$$

The total temperature in the annulus behind rotor 2 is given by:

$$Tt3(t) := Ts3(t) \cdot \left( 1 + \frac{\gamma - 1}{2} \cdot M3(t)^2 \right) \quad (A.54)$$

The corresponding heat transfer is

$$qs3e(t) := -St2 \cdot \rho a3(t) \cdot Cp \cdot \left( Tt3(t) \cdot \frac{1 + r \cdot \frac{\gamma - 1}{2} \cdot M3(t)^2}{1 + \frac{\gamma - 1}{2} \cdot M3(t)^2} - T0 \right) \cdot M3(t) \cdot a3(t) \quad (A.55)$$

Here again, we assume the walls to be a semi-infinite body. The temperature variation is given by:

$$Tee3(\eta, t) := T0 + \frac{\sqrt{\alpha 3}}{k3 \cdot \sqrt{\pi}} \cdot \int_0^t -qs3e(t - \tau) \cdot e^{-\eta^2} \cdot \frac{1}{\sqrt{\tau}} d\tau \quad (A.56)$$

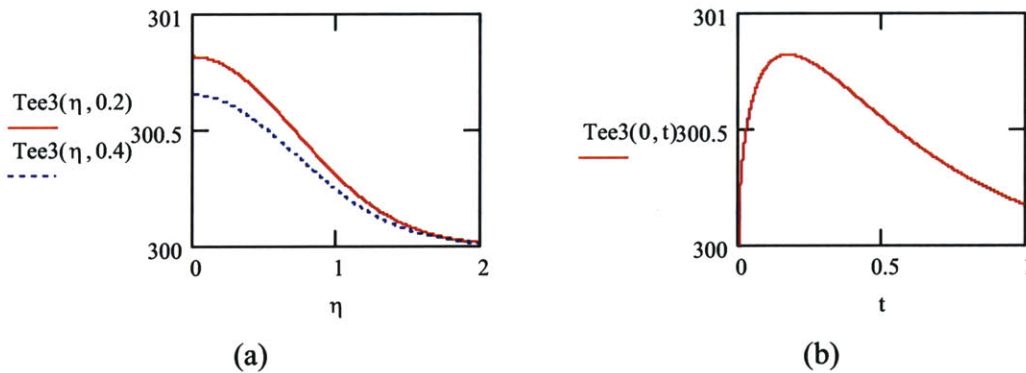


Figure A.17. - Temperature Evolution of the Trailing Edge Parts of Rotor 2 Blades vs. Depth for Different Time Points (a) and vs. Time at the Surface (b).

We will now compute the heat transfer in the walls behind rotor 2

$$M3ex := 0.48$$

$$qs4(t) := -St2 \cdot \rho a3(t) \cdot Cp \cdot \left( Tt3(t) \cdot \frac{1 + r \cdot \frac{\gamma - 1}{2} \cdot M3ex^2}{1 + \frac{\gamma - 1}{2} \cdot M3ex^2} - T0 \right) \cdot M3ex \cdot a3(t) \quad (A.57)$$

Let us compute the overall heat transfer:

$$\text{For rotor 1:} \quad Qr1(t) := \frac{A1}{2} \cdot qs0(t) \cdot 20 + \frac{A1}{2} \cdot qs1(t) \cdot 20 \quad (A.58)$$

$$\text{For rotor 2:} \quad Qr2(t) := \frac{A2}{2} \cdot qs2(t) \cdot 29 + \frac{A2}{2} \cdot qs3(t) \cdot 25 \quad (A.59)$$

$$\text{For the IGV:} \quad QIGV(t) := 35 \cdot hcIGV(0s) \cdot AIGV \cdot \left( Tt0(t) \cdot \frac{1 + r \cdot \frac{\gamma - 1}{2} \cdot M0^2}{1 + \frac{\gamma - 1}{2} \cdot M0^2} - T0 \right) \quad (A.60)$$

$$\text{For the front duct:} \quad Qfront(t) := 0.0427m^2 \cdot qs00(t) \quad (A.61)$$

$$\text{For the aft duct:} \quad Qaft(t) := 0.0353m^2 \cdot qs4(t) \quad (A.62)$$

$$\text{For rotor 1 hub:} \quad Qcone1(t) := 0.0045m^2 \cdot \left( \frac{qs0(t) + qs1(t)}{2} \right) \quad (A.63)$$

$$\text{For rotor 2 hub:} \quad Qcone2(t) := 0.008m^2 \cdot \left( \frac{qs2(t) + qs3(t)}{2} \right) \quad (A.64)$$

$$\text{For the casing around rotor 1:} \quad Qring1(t) := 0.015m^2 \cdot \left( \frac{qs0e(t) + qs1e(t)}{2} \right)$$

$$\text{For the casing around rotor 2:} \quad Qring2(t) := 0.014m^2 \cdot \left( \frac{qs2e(t) + qs3e(t)}{2} \right)$$

The total heat transfer is equal to:

$$Qw(t) := Qr1(t) + Qr2(t) + QIGV(t) + Qfront(t) + Qaft(t) + Qcone1(t) + Qcone2(t) + Qring1(t) + Qring2(t) \quad (A.66)$$

From there on, we want to compute the correction to provide to the indicated efficiency to find the adiabatic efficiency. This correction is based on the difference between the total enthalpy measured at the outlet of rotor 2 and the total adiabatic enthalpy at this same station. The computation of this difference is based on the assumption on the remarks detailed in section 5.3. So the difference between the 2 enthalpies is equal to the heat exchanged in the compression (The justification of this assumption will be given later):

$$1/\eta_{ad} = 1/\eta_{ind} + Q_w \cdot \tau / (h_{o2is} - h_{o1}) \quad (A.67)$$

Let 'Corr' be the correction term. Then, using the blow-down model:

$$\begin{aligned} W_c &:= 0.586t & P_{is} &:= 0.4 & P_{ic} &:= 1.9 \cdot 1.63 \\ A_c &:= 252.40 \ln^2 & P_0 &:= 30.40 \text{psi} & \tau &:= 1.43t \end{aligned}$$

$$\text{Corr}(t) := \frac{\tau \cdot Q_w(t)}{\frac{P_{is} \cdot P_0 \cdot \left(1 + \frac{t}{\tau_{bd}}\right)^{\gamma-1} \cdot A_c \cdot W_c}{\sqrt{R_g \cdot T_0 \cdot \left(1 + \frac{t}{\tau_{bd}}\right)^{-2}}} \cdot C_p \cdot Tt_0(t) \cdot P_{ic}^{\frac{\gamma-1}{\gamma}}} \quad (A.68)$$

$$\eta_{ad}(\eta_{ind}, t) := \frac{1}{\frac{1}{\eta_{ind}} - \text{Corr}(t)} \quad (A.69)$$

$$\text{Errmes}(\eta_{ind}, t) := \eta_{ad}(\eta_{ind}, t) - \eta_{ind} \quad (A.70)$$

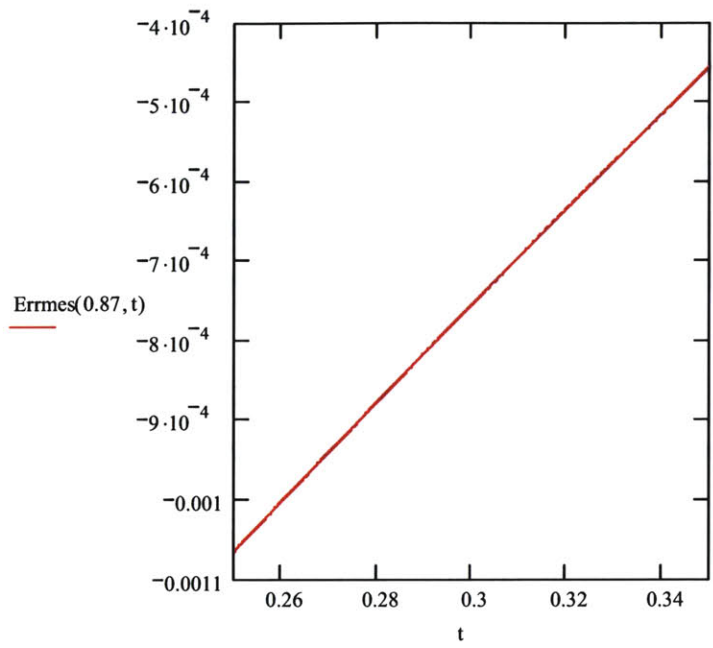


Figure A.18. - Difference Between Adiabatic and Indicated Efficiency Over the Test Time.

**9. Appendix B: Detailed calculation of the Total Temperature Probe Errors.**

For the upstream rake temperature probes, we can compute the Biot number around the wire to determine the response time of this wire.

For an error of 0.025K due to the recovery error, with a recovery factor in the laminar case equal to the square root of the Prandtl number, we can compute the necessary Mach number in the shield:

- At  $t = 0s$ :

$$T_{t0}(0s) = 300K$$

$$\mu_{i1} := 1.838 \cdot 10^{-5} \cdot \frac{\text{kg}}{\text{m} \cdot \text{s}}$$

$$\text{Pr}_{i1} := 0.77$$

$$\gamma_{i1} := 1.40$$

$$k_{g_{i1}} := 1.641 \cdot 10^{-2} \cdot \frac{\text{W}}{\text{m} \cdot \text{K}}$$

$$M_{v_{i1}} := \sqrt{\frac{0.025K}{\left[ (1 - \sqrt{\text{Pr}_{i1}}) \cdot T_0 - 0.025K \right] \cdot \frac{\gamma_{i1} - 1}{2}}} \quad (\text{B.1})$$

Which yields a Mach number of:

$$M_{v_{i1}} = 0.059$$

Let us compute the vent hole area that will give us this Mach number around the thermocouple. We need to account for the compressibility effects in the flow:

$$A_{inlet} := \pi \cdot \left( \frac{4.4069}{2} \cdot 10^{-3} \text{m} \right)^2$$

$$C_d := 0.6$$

$$Y_{i1}(A_{vent_{i1}}) := 1 - \left[ 0.41 + 0.35 \cdot \left( \frac{A_{vent_{i1}}}{A_{inlet}} \right)^2 \right] \cdot \frac{1}{\gamma_{i1}} \cdot \left[ 1 - \left( 1 + \frac{\gamma_{i1} - 1}{2} \cdot M_0^2 \right)^{\frac{-\gamma_{i1}}{\gamma_{i1} - 1}} \right] \quad (\text{B.2})$$

$$M_{v1} \cdot \sqrt{\gamma_{i1} \cdot R_g \cdot \frac{T_{t0}(0s)}{1 + \frac{\gamma_{i1} - 1}{2} \cdot M_{v1}^2}} - \gamma_{i1}(\lambda) \cdot C_d \cdot \left(1 + \frac{\gamma_{i1} - 1}{2} \cdot M_0^2\right)^{\frac{-1}{\gamma_{i1} - 1}} \cdot \frac{\lambda}{A_{inlet}} \cdot M_0 \cdot a_0(0s) = 0$$

(B.3)

$$\lambda_{i1} := \text{Find}(\lambda)$$

$$\lambda_{i1} = 2.923 \times 10^{-6} \text{ m}^2$$

$$D_{venti1} := \sqrt{\frac{\lambda_{i1}}{\pi}} \cdot 2$$

(B.4)

$$D_{venti1} = 1.929 \times 10^{-3} \text{ m}$$

For the single probes, this calculation gives a vent hole size of:

$$D_{ventisin1} = 2.424 \times 10^{-3} \text{ m}$$

Now, the corresponding heat transfer coefficient and Biot number are:

$$h_{probe1}(t, R) := \frac{0.664 \cdot \sqrt{\rho a_0(t)} \cdot \left( M_{v1} \cdot \sqrt{\gamma_{i1} \cdot R_g \cdot \frac{T_{t0}(t)}{1 + \frac{\gamma_{i1} - 1}{2} \cdot M_{v1}^2}} \right) \cdot \frac{2 \cdot R}{\mu_{i1}} \cdot \text{Pr}_{i1}^{\frac{1}{3}} \cdot \text{kg}_{i1}}{2 \cdot R}$$

(B.5)

$$\text{Biot1}(R, t) := h_{probe1}(t, R) \cdot \frac{R}{19.2 \frac{\text{W}}{\text{m} \cdot \text{K}}}$$

(B.6)

$$\text{Biot1}\left(\frac{12.7}{2} \cdot 10^{-6} \text{ m}, 0s\right) = 9.564 \times 10^{-4}$$

With such a low value of the Biot number, only the first coefficient of the series given the temperature response of the thermocouple is representative of the behavior of the thermocouple. The time response is given by the following calculation:

$$x := 0.1$$

Given

$$x \cdot J_1(x) - \text{Biot} \left( \frac{12.7}{2} \cdot 10^{-6} \text{ m}, 0 \text{ s} \right) \cdot J_0(x) = 0 \quad (\text{B.7})$$

$$x_{i1} := \text{Find}(x)$$

$$x_{i1} = 0.044$$

$$\frac{2}{x_{i1}} \cdot \frac{J_1(x_{i1})}{(J_0(x_{i1}))^2 + (J_1(x_{i1}))^2} = 1 \quad (\text{B.8})$$

$$t_{i1} := \frac{-1}{x_{i1}^2} \cdot \ln(0.01) \cdot \frac{\left[ \frac{(12.7 \cdot 10^{-6} \text{ m})}{2} \right]^2}{\frac{19.2 \frac{\text{W}}{\text{mK}}}{8730 \frac{\text{kg}}{\text{m}^3} \cdot 448 \frac{\text{J}}{\text{kgK}}}}$$

$$t_{i1} = 0.02 \text{ s}$$

Let us do the computation of the time-response for the bead, which has the shape of a sphere with a diameter of  $3 \cdot 0.0005$  in. From [7], we can use the following equations:

$$x \cdot \cos(x) + \left( \text{Biot} \left( \frac{2 \cdot 12.7}{2} \cdot 10^{-6} \text{ m, 0s} \right) - 1 \right) \cdot \sin(x) = 0 \quad (\text{B.9})$$

$$x_{ib1} := \text{Find}(x)$$

$$x_{ib1} = 0.064$$

$$2 \cdot \frac{\sin(x_{ib1}) - x_{ib1} \cdot \cos(x_{ib1})}{x_{ib1} - \sin(x_{ib1}) \cdot \cos(x_{ib1})} = 1 \quad (\text{B.10})$$

$$t_{ib1} := \frac{-1}{x_{ib1}^2} \cdot \ln(0.01) \cdot \frac{\left[ \frac{(2 \cdot 12.7 \cdot 10^{-6} \cdot \text{m})}{2} \right]^2}{\frac{19.2 \frac{\text{W}}{\text{mK}}}{8730 \frac{\text{kg}}{\text{m}^3} \cdot 448 \frac{\text{J}}{\text{kgK}}}}$$

$$t_{ib1} = 0.037\text{s}$$

This process can be repeated for  $t = 0.250$  s and  $t = 0.500$  s. The results are:

Time (s)	Casing Mach Number	Wire Response Time (s)	Bead Response Time(s)
0.250	0.058	0.03	0.057
0.500	0.059	0.045	0.084

Table B.1. – Casing Mach Number, Wire and Bead Response Times for the Upstream Probes at  $t = 250$  ms and  $t = 500$  ms.

Similarly, for the downstream rake probes, a similar calculation gives a vent hole size of:

$$D_{vent1} = 1.502 \times 10^{-3} \text{ m}$$

As for the Mach number in the head casing and the response times:

<b>Time (s)</b>	<b>Casing Mach number</b>	<b>Wire response time (s)</b>	<b>Bead response time(s)</b>
0.000	0.03	0.012	0.023
0.250	0.03	0.019	0.036
0.500	0.03	0.028	0.053

Table B.2. - Casing Mach Number, Wire and Bead Response Times for the Downstream Probes  
at t = 250 ms and t = 500 ms.

The downstream single probes must have a vent hole size of:

$$D_{ventsin1} = 1.878 \times 10^{-3} \text{ m}$$

Let us focus in the conduction error for the upstream probes:

The characteristic spatial frequency of the phenomenon is equal to:

$$m(t, R) := \sqrt{\frac{hcprobei3(t, R) \cdot 2 \cdot \pi \cdot R}{19.2 \frac{W}{m \cdot K} \cdot \pi \cdot R^2}} \quad (B.11)$$

For the 3/16 probes, the conduction error is equal to:

$$L0 := 0.135m$$

$$\frac{2 \cdot \sinh\left(\frac{m\left(0.5s, 12.7 \cdot \frac{10^{-6}}{2} \cdot m\right) \cdot L0}{2}\right) \cdot (T0 - Tt0(0.5s))}{\sinh\left(m\left(0.5 \cdot s, 12.7 \cdot \frac{10^{-6}}{2} \cdot m\right) \cdot L0\right)} = 0.073K$$

For the 1/4 probes, the conduction error is equal to:

$$L14 := .180m$$

$$\frac{2 \cdot \sinh\left(\frac{m\left(0.5s, 12.7 \cdot \frac{10^{-6}}{2} \cdot m\right) \cdot L14}{2}\right) \cdot (T0 - Tt0(0.5s))}{\sinh\left(m\left(0.5 \cdot s, 12.7 \cdot \frac{10^{-6}}{2} \cdot m\right) \cdot L14\right)} = 5.27 \times 10^{-3} K$$

As for the conduction error of the downstream probes:

$$me(t, R) := \sqrt{\frac{hcprobee3(t, R) \cdot 2 \cdot \pi \cdot R}{19.2 \frac{W}{m \cdot K} \cdot \pi \cdot R^2}} \quad (B.12)$$

For the 3/16 probes:

$$\frac{2 \cdot \sinh\left(\frac{me\left(0.5s, 12.7 \cdot \frac{10^{-6}}{2} \cdot m\right) \cdot L0}{2}\right) \cdot \tau \cdot (T0 - Tt0(0.5s))}{\sinh\left(me\left(0.5 \cdot s, 12.7 \cdot \frac{10^{-6}}{2} \cdot m\right) \cdot L0\right)} = 0.014K$$

For the  $\frac{1}{4}$  probes:

$$\frac{2 \cdot \sinh\left(\frac{\text{me}\left(0.5\text{s}, 12.7 \cdot \frac{10^{-6}}{2} \cdot \text{m}\right) \cdot \text{L14}}{2}\right) \cdot \tau \cdot (T0 - Tt0(0.5\text{s}))}{\sinh\left(\text{me}\left(0.5 \cdot \text{s}, 12.7 \cdot \frac{10^{-6}}{2} \cdot \text{m}\right) \cdot \text{L14}\right)} = 4.979 \times 10^{-4} \text{ K}$$

Last concern is the radiation error:

Upstream, we compute that:

$$\sigma := 5.67 \cdot 10^{-8} \frac{\text{W}}{\text{m}^2 \text{K}^4}$$

$$\varepsilon_m := 0.4$$

$$\text{Eradi}(t, R) := \frac{\sigma \cdot \varepsilon_m \cdot (Tt0(t)^4 - T0^4)}{\text{hprobei3}(t, R)} \quad (\text{B.13})$$

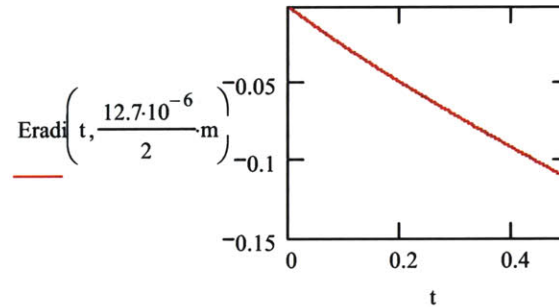


Figure B.1. – Radiation Error Evolution for the Upstream Probes, Over 1s.

Downstream:

$$\text{Erad}(t, R) := \frac{\sigma \cdot \varepsilon m \cdot \tau^4 \cdot (T(t)^4 - T_0^4)}{\text{hcprobe3}(t, R)} \quad (\text{B.14})$$

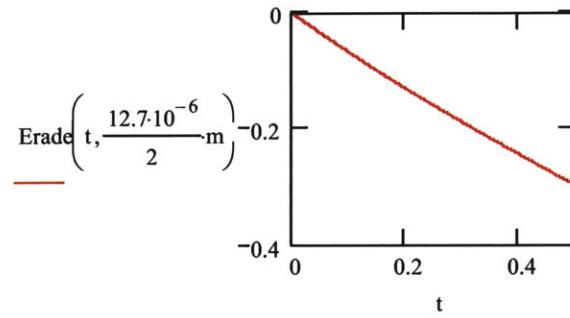


Figure B.2. - Radiation Error Evolution for the Downstream Probes, Over 1s.



## **10. Appendix C: Total Temperature Probes Drawings**



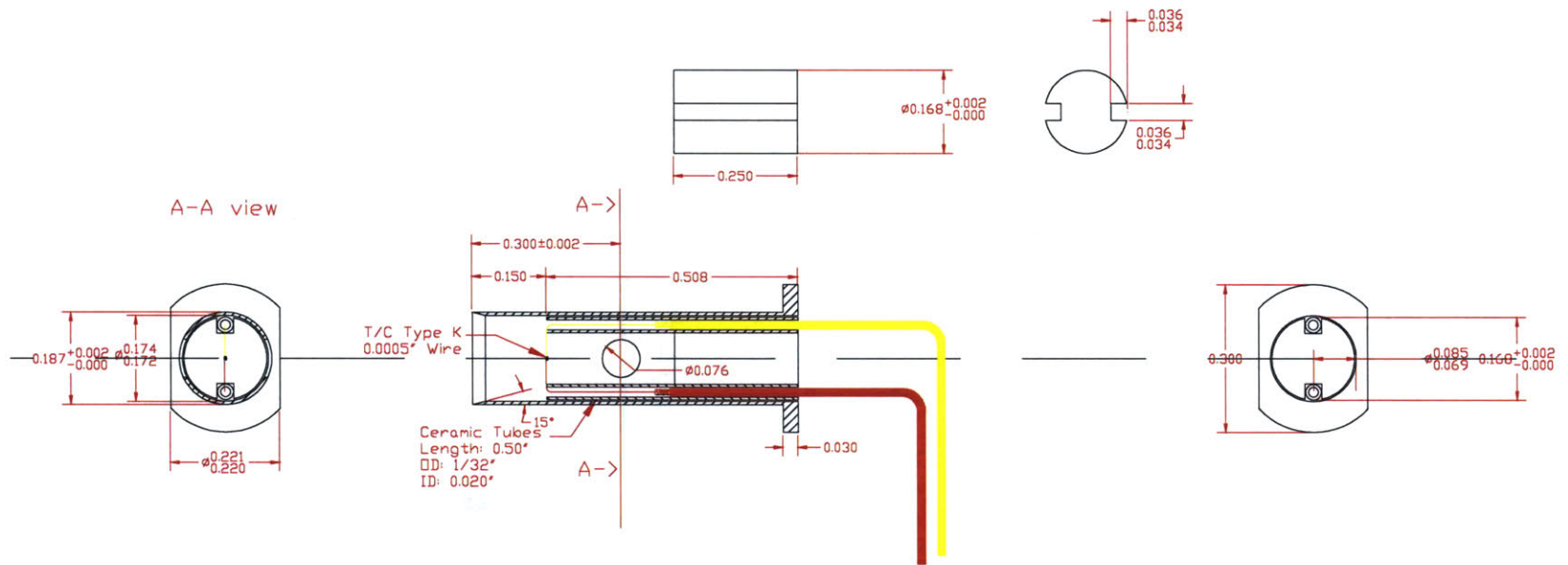


Figure C.1. – Upstream Rake Total Temperature Measurement Head.

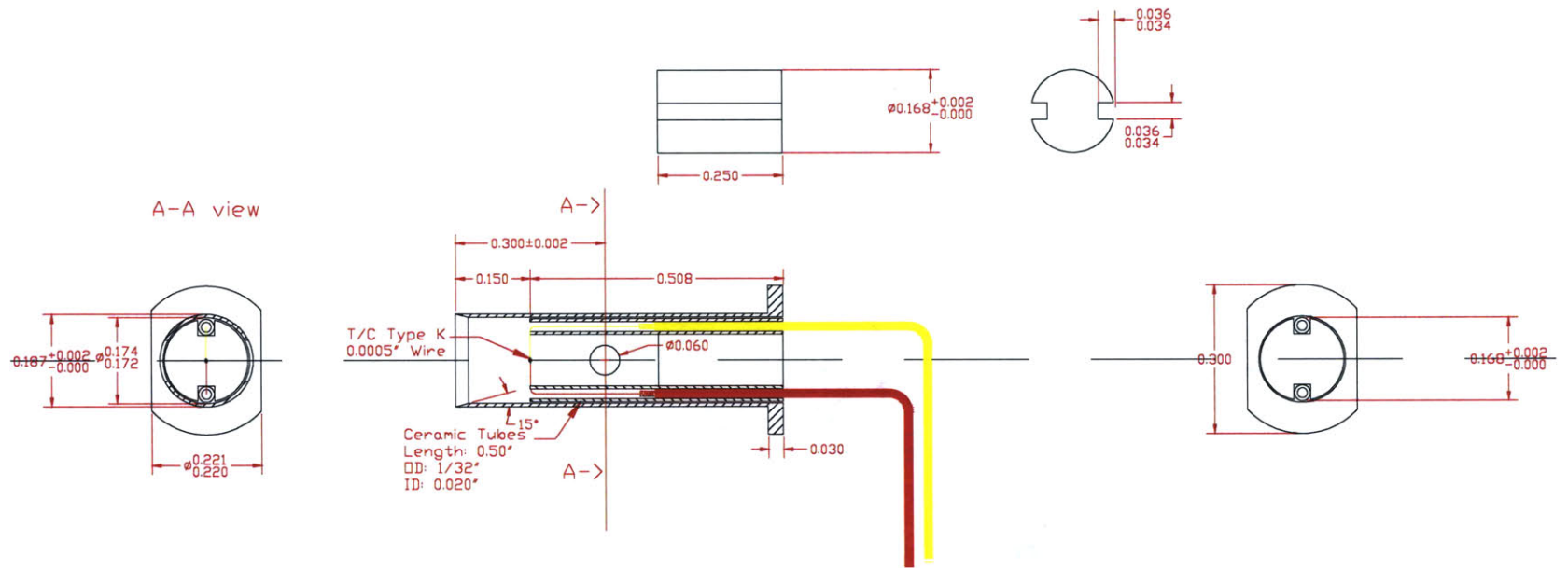


Figure C.2. – Downstream Rake Total Temperature Measurement Head.

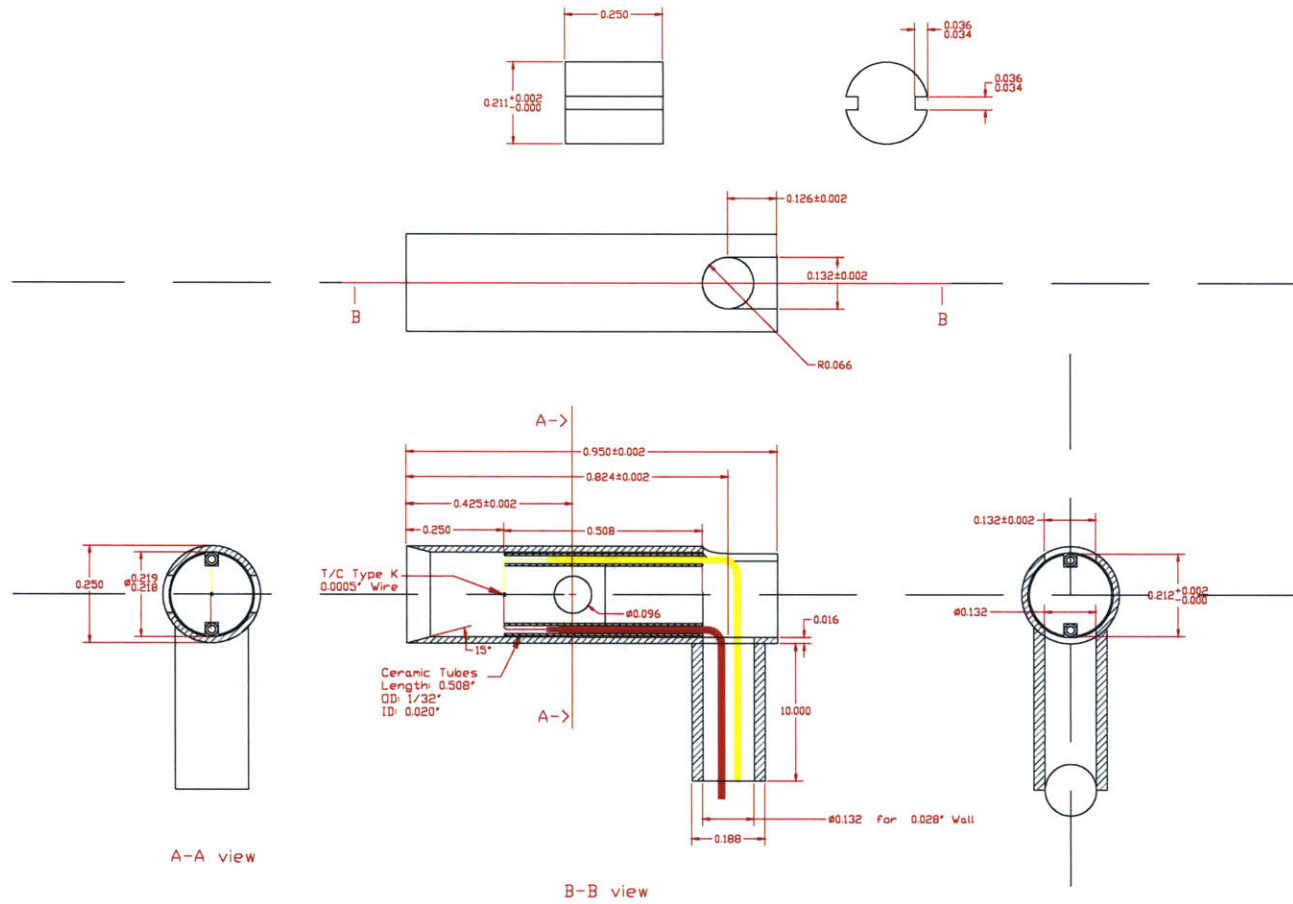


Figure C.3. – Upstream Total Temperature Measurement Probe.

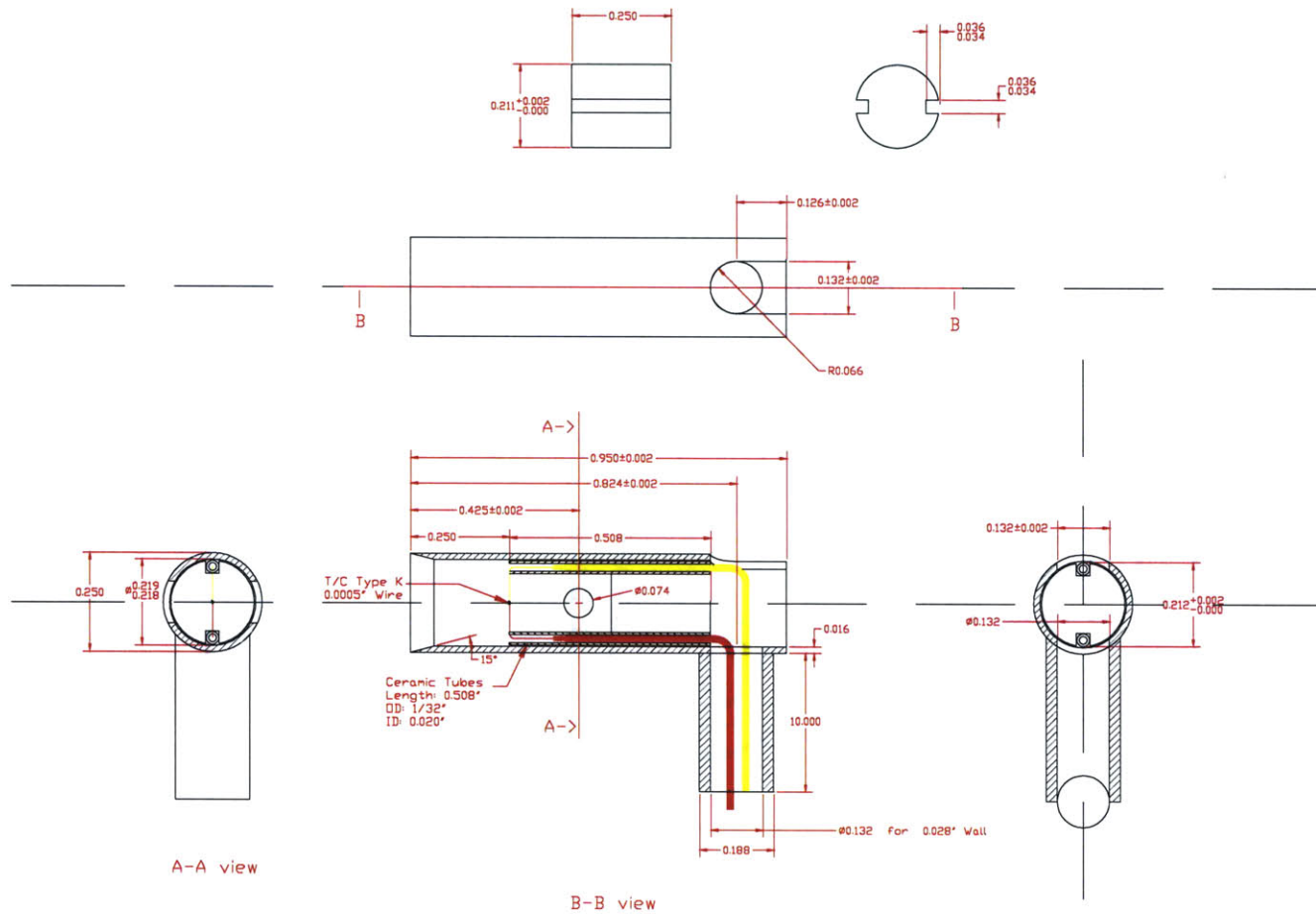


Figure C.4. - Downstream Total Temperature Measurement Probe.

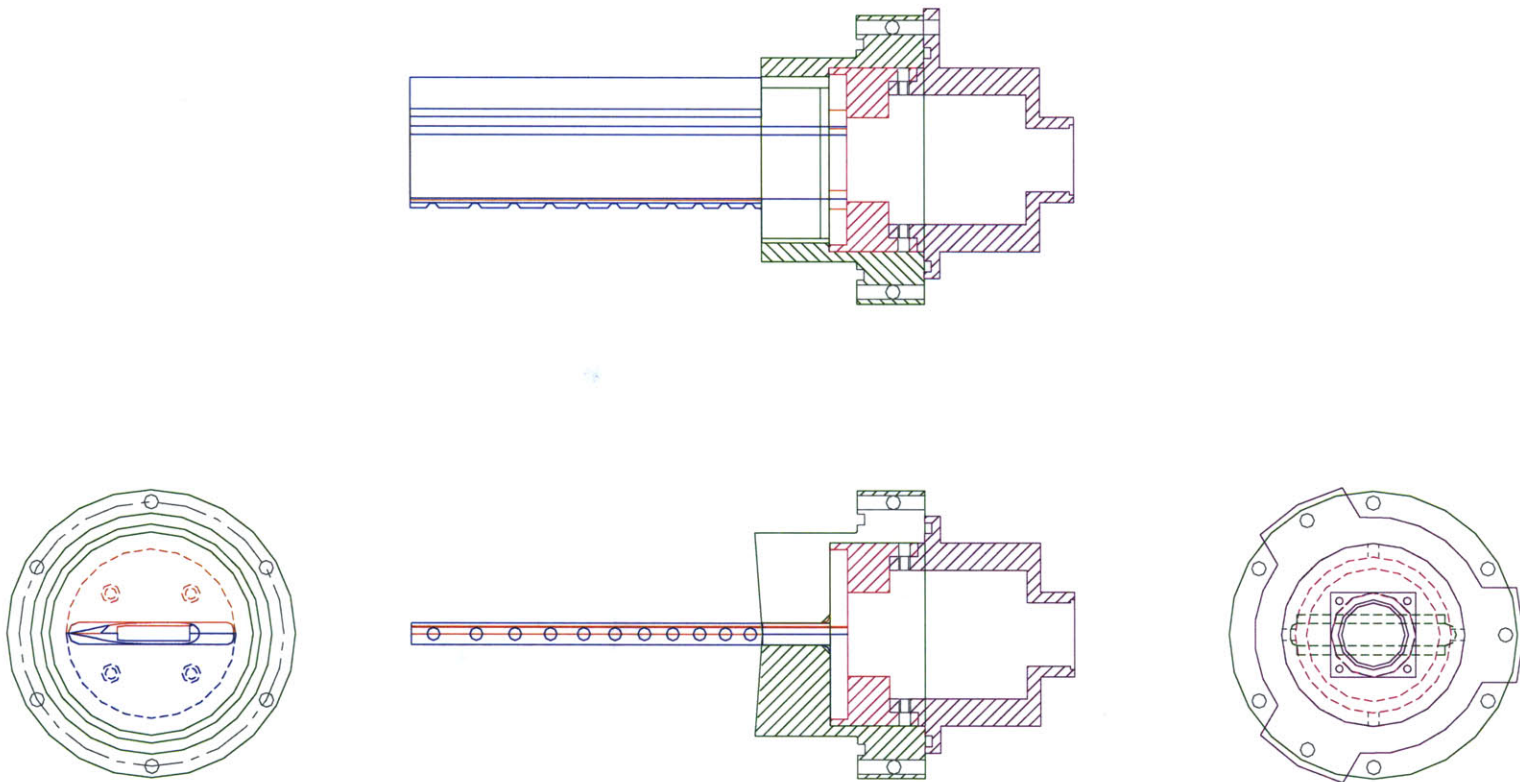


Figure C.5. – Upstream Total Temperature Measurement Rake Assembly.

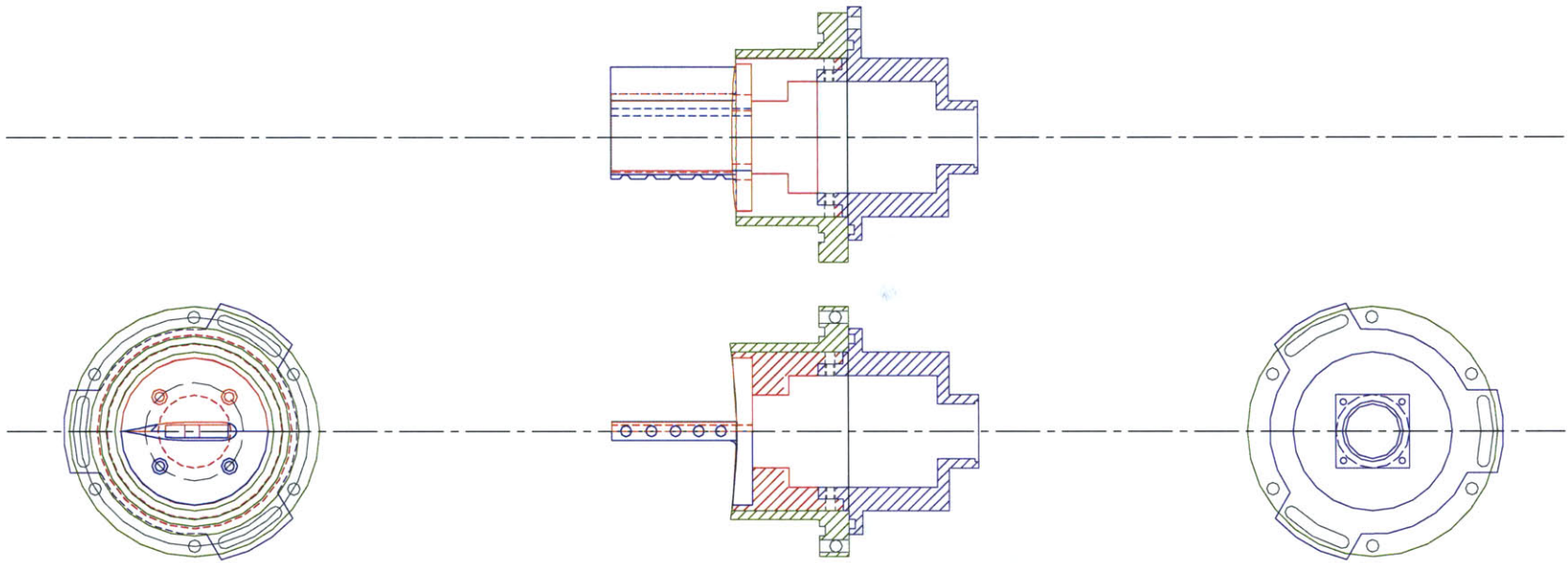


Figure C.6. – Downstream Total Temperature Measurement Rake Assembly (5 Head Model).

## **11. Appendix D: Total Pressure Probes Drawings**



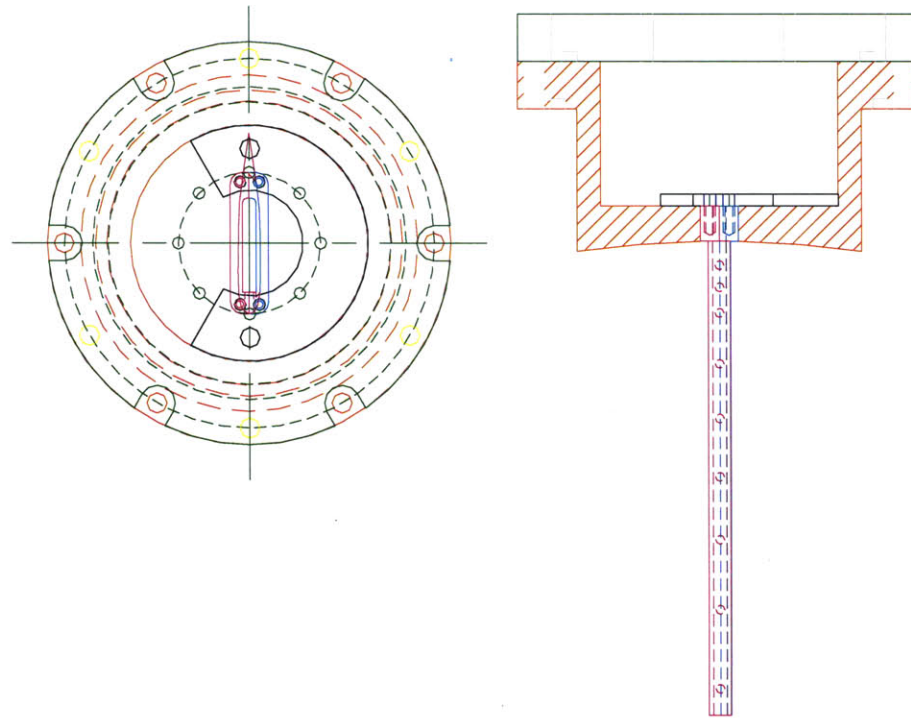


Figure D.1. – Upstream Total Pressure Measurement Rake Assembly.

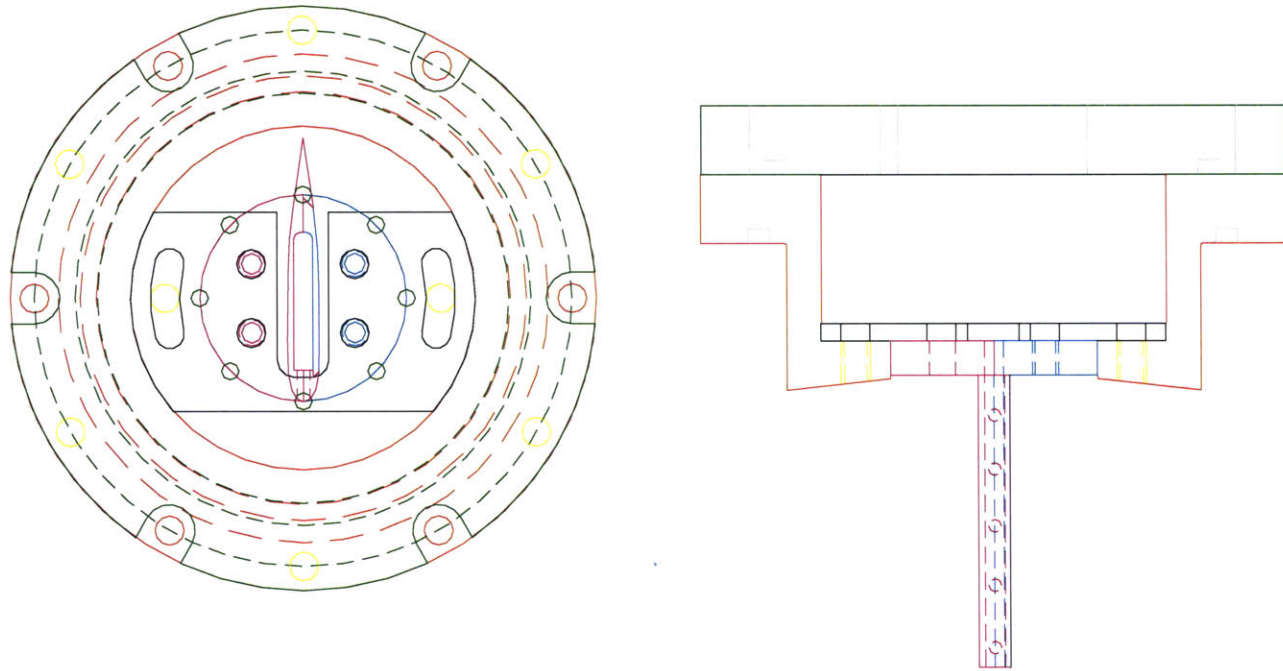


Figure D.2. – Downstream Total Pressure Measurement Rake Assembly.

## **12. Appendix E: Detailed Type-K Thermocouple Manufacturing Description**

**List of hardware components:**

- Head casing (according to prints)
- Stainless steel spacer (according to prints)
- Type-K unsheathed fine gage thermocouples (0.0005" wire dia - Omega CHAL-0005)
- Thermocouple insulators (1/32" OD - .020" ID – Omega ORX-020132)
- Thermocouple insulated wires (0.010" wire dia – Omega TFCY-010 (Chromel) & TFAL-010 (Alumel))
- Thermocouple wires, duplex insulated (Omega TT-K-20).
- Multipin design thermocouple connectors (Female flanged Omega MTC-24-FF)
- Thermocouple contact pins (Chromel MTC-CH-P and Alumel MTC-AL-P).
- ½"-thick Teflon pieces
- ½"-thick aluminum piece
- 3"x3"x¼" cork pads

**Chemical and soldering materials:**

- Epoxy Eccobond 104 and Eccobond 45 LV
- Solder (HMP alloy – Type 366 Flux from Vishay Micro Measurements)
- All Purpose Flux LA-CO N-3
- M-Line Rosine Solvent (from Vishay Micro Measurements)
- M-Line AR Activated Rosin Soldering Flux (from Vishay Micro Measurements)
- Acetone

**1<sup>st</sup> Step: Assembling the thermocouple insulators to the stainless steel spacer:**

1. In the ½"-thick Teflon pieces, drill clearance holes for the stainless steel spacers. (0.177" for 3/16-probes and 0.211" for ¼ probes)
2. Using a diamond file, cut 0.510" long pieces of thermocouple insulators.
3. Drill a clearance hole for these ceramic tubes in the ½"-thick piece of aluminum.
4. Insert the ceramic piece in the clearance hole and grind both ends against sandpaper, to give clean and square edges to the tubes. The aluminum piece acts

as a holder and guarantees that the tubes will be brought down to the correct length.

5. Using the Teflon pad as a jig, epoxy the ceramic tubes with Eccobond 104 in the grooves of the stainless steel spacer. The ceramic tube edges must be flush with one end of the aluminum piece.
6. Cure it for 3 hours at 300 degrees F.
7. Gently remove the assembled spacers from the jig using a small arbor press. Shocks may damage the ceramic tubes in that process.
8. Under the microscope, check that the ceramic tubes are parallel. Scrape away the excess of epoxy, using a diamond file. Check the OD of the spacer against the ID of the head casing.

**2<sup>nd</sup> Step: Mounting the thermocouple gage on the spacer:**

1. Tape down the spacer on a stainless steel holder. Put a piece of 0.010" almel wire through one ceramic tube and a piece of 0.010" chromel wire through the other ceramic tube. Strip them back 0.125", making sure the insulation does not ball up and allows the wire to move through the ceramic tubes without constraints. The wires should be 10" long for 3/16 probes and 24" long for ¼ probes.
2. Remove the gage from the package. Move the red and yellow dots to about 2" from the gage junction. Remove the white dot using acetone.
3. Tack the gage red wire and yellow wire gage to the 0.010" wires mounted on the spacers, using All Purpose Flux LA-CO N-3 and multicore 570-28R solder.
4. Turn the small gage wire at least four times around the large wire and solder, using again All Purpose Flux LA-CO N-3 and multicore 570-28R solder.
5. Put small droplets of Eccobond 104. Gently draw the wires in so as straighten the gage wire and center the junction between the ceramic tubes.
6. Tape down the 0.010" wires to stress relieve the gage and prevent it from moving during the curing period.
7. Cure the assembly for 3 hours at 300 degrees F.

8. Let the assembly cool down and check the continuity between the 2 wires. Add epoxy and cure again to cover any contacts between the edge of the ceramic tube and the gage (Figure E.1).

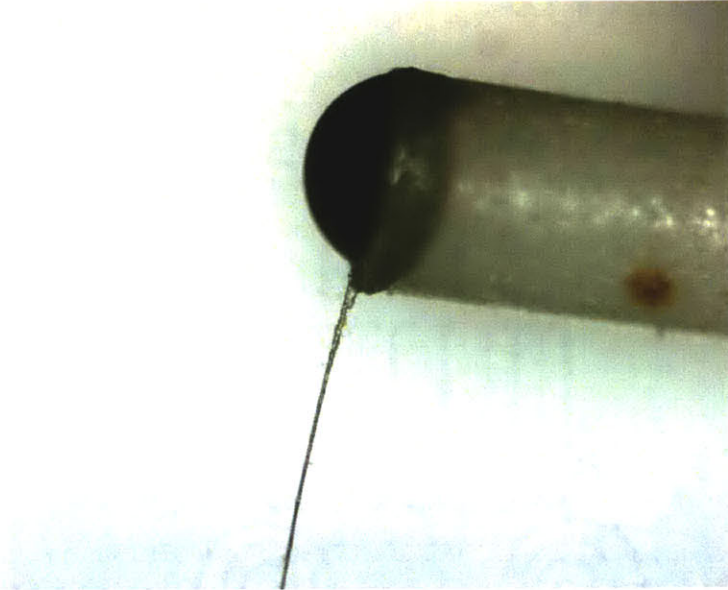


Figure E.1. – Close-Up View of the Thermocouple Gage Wire Epoxied to the Ceramic Stem.

### **3<sup>rd</sup> Step: Mounting the thermocouple insert on the head casing:**

For 3/16” probes:

1. Drill a clearance hole for the 3/16” heads in the cork pad. Insert the head casing until the flange meets the cork. This piece serves as a holder in the process.
2. Coat the thermocouple spacer with Eccobond 104 epoxy and insert it into the head. Make sure the rear of the spacer is flush with the rear face of the head. Turn the insert inside the head so that the gage wire is perpendicular to the vent hole axis.
3. Tape down the wires to prevent the insert from moving during the curing process.
4. Cure for 3 hours at 300 degrees F.
5. Let the assembly cool down. Check the continuity. Put the TC head in a small graduated cylinder with acetone for one hour, to clean the gage. Check the result under the microscope.

For ¼” probes:

1. Measure 10.250” from the spacer rear side and strip the wire insulation over 0.250”. Put Eccobond 104 epoxy and slide ½” ceramic tubes over the exposed wire.
2. Coat the thermocouple spacer with epoxy 104 and put into the head. The rear face must be flush with the inside of the stem piece and the gage must be perpendicular to the vent hole axis. Tape the wires down around the exterior of the stem tube. Cure for 3 hours at 300 degrees F.
3. Let the probe cool. Then run the wires down the stem, one at a time, and make sure they are not stressed by leaving a small loop behind the spacer face.
4. Using a syringe, fill the stem with Eccobond from the bottom end to seal the probe. Cure for 3 hours and add epoxy as needed.

**4<sup>th</sup> Step: Building the leak-proof connectors for the rakes:**

1. Remove the rubber part from the side that will accommodate the thermocouple wires on the thermocouple connector. Remove 3/16” of metal from the casing on the lathe and take of the paint from the inside area.
2. Cut 1 ¼” pieces of TT-K-20 wires. Strip back 3/16” of insulation on both ends and crimp them to the appropriate pins. Insert the pin on the connector according to a predetermined pattern.
3. Fill a plastic syringe with Eccobond 45LV epoxy and inject epoxy between the mounted pins, under the microscope. Once the bottom of the connector is covered, place the connector in a vacuum pump to degas the epoxy. This will cause the epoxy to bubble and overflow from the connector. To minimize the loss of epoxy and keep the connector as clean as possible, form a small chimney around the connector using aluminum foil. Cover also each wire with a transparent plastic tube. Repeat this process 4 consecutive times until the level of epoxy reaches the metallic edge of the connector. Remove the transparent tubes from the wires and cure the connector for 45 minutes at 200 degrees F.

4. Put vacuum seal around the O-ring of the connector and place it on the connector. Hook it to a vacuum pump, pull vacuum on the wire side of the connector and register the pressure variation overnight.

**5<sup>th</sup> Step: Mounting the 3/16 probes on the rakes:**

1. Insert the heads on the rake and put 2 drops of Eccobond 104 on the side of the flange that will be in contact with the rake. Tape down the wires to the trailing edge of the airfoil and cure for 3 hours at 300 degrees F.
2. File the flange and the excess of epoxy off the cover groove, so as to allow that cover to slide in smoothly. Check the continuity of each probe.
3. To remove a broken head, scrape away the epoxy, with a diamond file, as much as possible. Finish removing with a hammer. It is crucial to remove as much epoxy as possible so as to avoid hammering the rake too strongly. The shocks caused by the hammer can break the neighboring gages. Repeat the process to insert a new head.
4. Label each thermocouple wire and lace them together for easier and safer handling (Figure E.2)
5. Close the airfoil and screw it to the front canister piece. Pass the wires through the aft canister piece.
6. Cut ½"-long pieces of shrink tubes and place them over each wire. Strip back the wires' ends over 1/8". Using multicore 570-28R and M-Line AR Activated Rosin Soldering Flux, solder these ends to the cables on the connector cables, according to the laying pattern. For easier handling, bend the TT-K-20 wires to space their extremities. Clean with M-Line Rosine Solvent. Cover the soldered area with the shrink tubes and shrink them with the heat gun. Close the entire assembly.

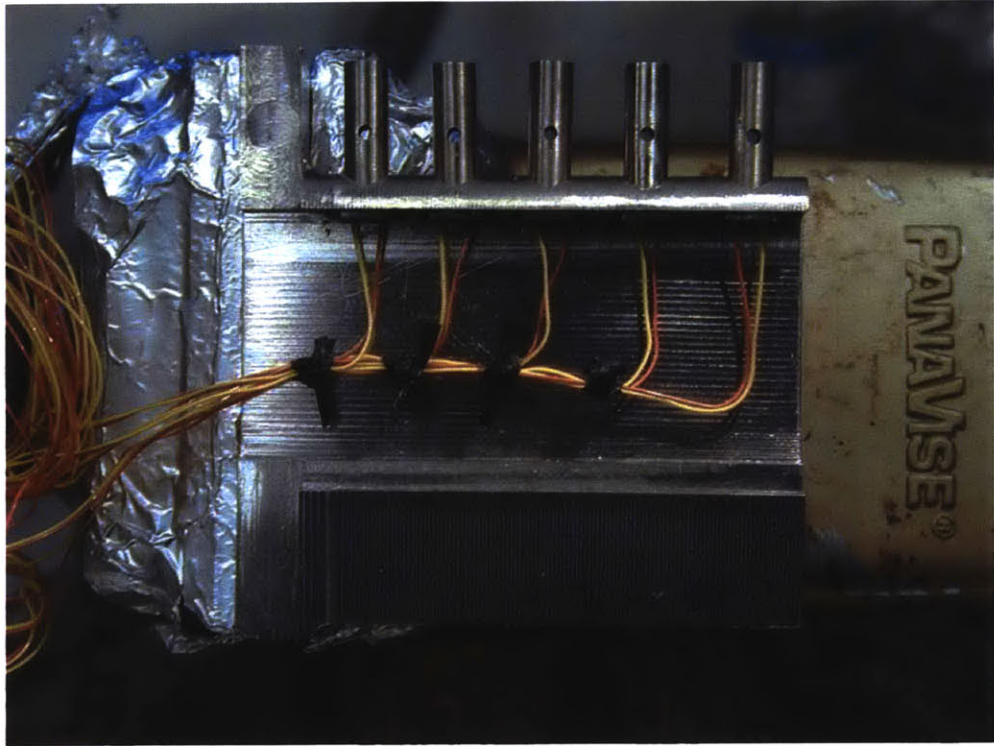


Figure E.2. – View of the Thermocouple Extension Cables Laced Together in the Rake Airfoil Cavity.



## References and Bibliography

- [1] Kerrebrock Jack L.. *The Prospects for Aspirated Compressors*. MIT – AIAA-2000-2472. 2000
- [2] Parker David V.. *Design and Operation of a Counter-Rotating Aspirated Compressor Blow-Down Test Facility*. Master's thesis, Massachusetts Institute Technology, 2005.
- [3] Cai Yi. *Aerodynamic Performance Measurements in A Fully Scaled Turbine*. Master's thesis, Massachusetts Institute Technology, 1998.
- [4] American Society for testing and Materials, 1916 Race Street, Philadelphia, PA 19103. *Manual on the Use of Thermocouple in a Temperature Measurements*. 1970.
- [5] Cattafesta L.N.. *An Experimental Investigation of the Effects of Inlet Radial Temperature Profiles on the Aerodynamic Performance of a Transonic Turbine Stage*. Master's thesis, Massachusetts Institute Technology, 1988.
- [6] Whitman, Gayne. *The Effects of the Reynolds and Mach Number on the Recovery Factor of Cylindrical Thermocouples Immersed in a Rapidly Moving Air Stream*. Master's thesis, Massachusetts Institute of Technology, 1950.
- [7] Mills A.F. *Heat and Mass Transfer*. Ed. Irwin, 1995.
- [8] <http://www.hartscientific.com/products/bathfluid.htm>
- [9] DeWitt D.P. Incropera F.P. *Fundamentals of Heat and Mass Transfer*. Wiley and Sons, Inc, second edition, 1985.
- [10] Russell Walter R. Gracey William, Letko William. *Wind tunnel investigation of a number of total pressure tubes at high angles of attack*. Technical Report, 2331, National Advisory Committee for Aeronautics, 1951.
- [11] Pankhurst R.C. Ower E. *The Measurement of Air Flow*. Pergamon Press, fifth edition, 1977.
- [12] Coleman H.W. *Experimentation and Uncertainty Analysis for Engineers*. Wiley, 1999.
- [13] <http://www.unitedsensorcorp.com/kiel.html>
- [14] <http://www.unitedsensorcorp.com/pitot.html>
- [15] <http://www.omega.com/Temperature/pdf/TRCIII.pdf>
- [16] Merchant Ali. *Aerodynamic Design and Performance of Aspirated Airfoils*. Proceedings of Turbo Expo 2002, 2002.
- [17] Merchant Ali. *MAFC Aero Design*. Massachusetts Institute of Technology. 2004.
- [18] <http://sine.ni.com/nips/cds/view/p/lang/en/nid/1055>
- [19] <http://sine.ni.com/nips/cds/view/p/lang/en/nid/13677>
- [20] <http://sine.ni.com/nips/cds/view/p/lang/en/nid/12785>
- [21] White F.M. *Fluid Mechanics*. McGraw-Hill Series in Mechanical Engineering, 1999.
- [22] Carslaw H.S. and Jaeger J.C. *Conduction of Heat in Solids*. Oxford University Press, 1986.